ELECTROCATALYTIC AND MATERIALS PROPERTIES AND MEMBRANE SEPARATION APPLICATIONS OF IRON-DOPED BARIUM ZIRCONATE

A Dissertation

by

HAOMIAO ZHANG

Submitted to the Office of Graduate and Professional Studies of
Texas A&M University
in partial fulfillment of the requirements for the degree of

DOCTOR OF PHILOSOPHY

Chair of Committee,	Benjamin A. Wilhite
Committee Members,	Perla Balbuena
	Tahir Cagin
	Haiyan Wang
Head of Department,	M. Nazmul Karim

May 2016

Major Subject: Chemical Engineering

ABSTRACT

This dissertation presents the first investigation of a novel mixed conducting $BaZr_{0.9}Fe_{0.1}O_{3-\delta}$ perovskite (BZF10) in terms of materials properties, combined electrochemical and catalytic properties over a complete span of gas environments (O_2, CO_2, H_2O, CO, H_2) as well as membrane separation applications. This unique combination of electrical conduction, catalytic activity and long-term material stability makes this material a promising candidate for solid oxide electrolytic cell (SOEC) and solid oxide reversible fuel cell (SORFC) applications.

Powder of BZF10 was synthesized via solid-state reaction and characterized using synchrotron X-ray diffraction (XRD); results indicated the presence of a primary cubic perovskite phase. Transmission electron microscopy (TEM) images indicated stable grain structure and well-defined grain boundaries within the pellet. Electrical conductivity relaxation (ECR) was carried out on the sintered pellet at 600-800^oC under various oxygen partial pressures (pO_2). ECR indicated that both chemical diffusion coefficient D_V and surface kinetic parameter k' increased with pO_2. The oxygen permeation flux through BZF10 membrane at 900^oC was 0.102 mL/(min·cm^2) with air/Ar gradient. Electrochemical Impedance Spectroscopy (EIS) and effluent gasses analysis were carried out at 600-800^oC under a wide range of gas environments. Under dry O_2 conditions, this material displayed p-type semi-conduction behavior; upon exposure to dry CO_2 atmosphere, the material showed catalytic activity towards CO_2 reduction to CO and O_2; exposure to moisture inert suggested only mild interaction with

steam; under moist CO environment, a complex conduction mechanism was displayed alongside significant rates of water-gas-shift reaction; exposure to humidified H_2 resulted in increase in conductivity with H_2 partial pressure indicating n-type semi-conduction. Upon completion of >1,000 hours of continuous exposures, physical inspection of the BZF10 electrochemical cell indicated negligible chemical or mechanical degradation. XRD and TEM indicated stable phase composition and stable grain structure within the pellet. The hydrogen permeation flux was 0.75 mL/(min·cm^2) at 900^{o}C when exposed to 20%H_2/Ar and controlled by bulk diffusion. In the range of 600-700^{o}C, the hydrogen permeation was limited by the electronic transport with higher activation energy (E_a); while in the range 700-900^{o}C, the hydrogen permeation was limited by the mixed protonic-electronic transport with low E_a.

To my family

ACKNOWLEDGEMENTS

I would like to express my deepest appreciation to my advisor, Professor Benjamin A. Wilhite, for his inspiring and encouraging guidance throughout my Ph.D. study. I would like to thank my committee members, Professors Haiyan Wang, Perla Balbuena, and Tahir Cagin, for their guidance and support throughout the course of this research. I would like to thank Argonne National Lab for providing synchrotron XRD analysis and the Microscopy and Image Center at Texas A&M University for TEM and XEDS. Thanks also go to my friends and colleagues and the department faculty and staff for making my time at Texas A&M University a great experience. Specifically thanks to Dr. Aravind Suresh and Randy Marek for their lab support and Towanna Arnold for her administrative support. Finally, I would like to thank my parents for their encouragement and love.

TABLE OF CONTENTS

Page

LIST OF FIGURES

Page

LIST OF TABLES

Page

1. INTRODUCTION*

1.1 Goal statement

The goal of this dissertation is to investigate and identify homogeneous transition metal-doped perovskite for simultaneous electrochemical and catalytic activities and membrane separation applications, with long term mechanical and chemical stability especially under high-temperature humidified reducing atmospheres. The target material is iron-doped barium zirconate perovskite, with the hypothesis that the transition metal dopant could impart unique combinations of electrochemical and catalytic activity and maintain long-term chemical stability under both oxidizing and reducing environments. This represents a novel departure from traditional MIEC materials which have focused upon non-catalytic Lanthanide dopants to impart ionic/electronic conductivity.

1.2 Background

1.2.1 ABO_3 perovskite

"Perovskite", named from the Russian mineralogist Lev Perovski (1792 – 1856), denotes the class of ceramic materials with the same crystal structure of calcium titanium oxide ($CaTiO_3$), generally in the chemical formula of ABO_3. Perovskite structure, as

* Part of this chapter is reprinted with permission from "Materials Synthesizing, Electrochemical Characterization and O_2 Permeation Properties of Fe-Doped Barium Zirconates" by H. Zhang et al. / Solid State Ionics 266 (2014) 58–67, http://dx.doi.org/10.1016/j.ssi.2014.08.011; and "Electrical Conduction and Reaction Analysis on Mixed Conducting Iron-Doped Barium Zirconates" by H. Zhang, B.A. Wilhite / Solid State Ionics 286 (2016) 7–18, http://dx.doi.org/10.1016/j.ssi.2015.11.023; and "Electrochemical, Catalytic and O_2-Permeation Studies of Iron-Doped Barium Zirconates for Membrane Reactor Applications" by ECS Transactions, 61 (1) 307-318 (2014), 10.1149/06101.0307ecst.

shown in Figure 1.1, is a single cubic close-packed lattice, where the larger cation locates in the corner of the cube (A-site), the smaller cation occupies the cube center (B-site), and oxygen anion locates in the face center. The oxygen anion is surrounded by four A-site cations and two B-site cations, while the coordination number (the number of its nearest neighbors) for the A-site and B-site cations in this structure are twelve and six, respectively. A large group of metallic ions are stable in the cubic perovskite structure, if the tolerance factor t_f is in the range of 0.75 – 1.0 (Equation 1.1).

$$t_f = \frac{R_A + R_O}{\sqrt{2}(R_B + R_O)} \tag{1.1}$$

where R_A, R_B, R_O are the ionic radius of A-site, B-site cations and oxygen ions, respectively. The stability of perovskite structure may remain as an issue when the radius of the A-site and B-site ions are not comparable, as buckling and distortion may occur which can reduce coordination number. [1]

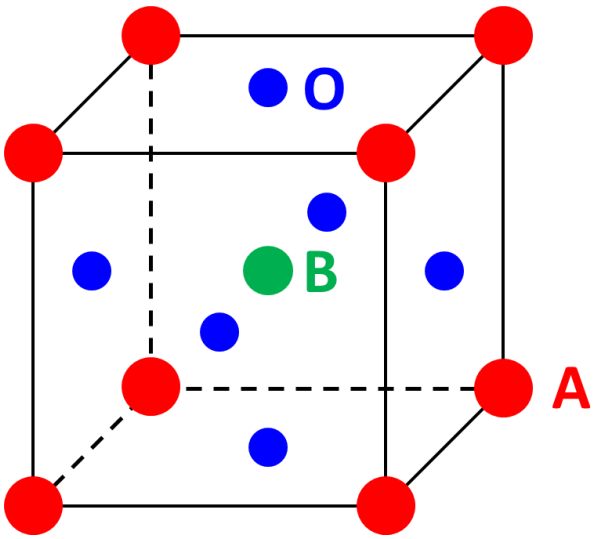

Figure 1.1: Illustration of cubic ABO_3 perovskite structure.

Perovskite materials can exhibit many properties including mixed oxygen ionic and electronic conductivity, protonic conductivity, superconductivity, piezoelectricity, and a multitude of dielectric properties. [2-8] In addition, perovskite-based catalysts have been reported for transformation of natural gas and biofuels into syn-gas (a mixture of CO and H_2) as well as environmental remediation based upon their catalytic activity in total combustion of volatile organic compounds (VOCs). [9-12] Moreover, these compounds are widely used in solid oxide fuel cells (SOFCs), solid oxide electrolysis cells (SOECs), solar cells, photoelectrolysis, and laser light generators applications. [13-21]

1.2.2 Mixed ionic and electronic conducting perovskites

Mixed ionic-electronic conductors (MIECs) have been explored for myriad sustainable-energy applications including high-performance batteries, oxygen separation, oxygen sensors, high-temperature fuel cell electrodes and CO_2 mitigation technologies over the past four decades. [22-24] MIECs are primarily employed as electrolytes in solid oxide fuel cells (SOFCs), where current flow occurs by the combined migration of oxygen ions (O^{2-}), electrical holes ($h^{\bullet}$) and/or electrons (e^{-}). [25-26] Solid oxide electrolytic cells (SOECs) with MIEC electrodes exhibiting suitable catalytic activity have recently been explored for the electrolysis of waste CO_2 and H_2O to syn-gas. [27] The syn-gas produced may in turn be converted to synthetic petroleum products via Fischer-Tropsch synthesis (FTS) technologies, currently employed by the oil and gas industries for production of liquid hydrocarbons from coal and natural gas. [28-30] Reversible solid-oxide fuel cells (RSOFCs) employing catalytically active MIEC electrodes displaying materials stability under both oxidizing and reducing atmosphere

would enable large-scale electrochemical energy storage and release via alternating between CO_2 reduction and CO oxidation. [31] The key advantage of this oxygen-transport process is that no external circuits are needed so long as a differential in oxygen partial pressure is maintained across the MIEC membrane. [32]

Significant research has been conducted on MIEC materials of a perovskite structure $(A^{+2}B^{+4}O_3)$ with one or more cations of disparate valency (e.g., X^{+3}) substituted into the stoichiometric oxide. [22,23,27,32-35] Such doping provides either extra oxygen atoms via A-site doping $(A_y^{+2}X_{1-y}^{+3}B^{+4}O_{3+\delta})$ or oxygen vacancies via B-site doping $(A^{+2}X_{1-y}^{+3}B_y^{+4}O_{3-\delta})$, both of which are capable of imparting electronic conductivity (electrons and/or holes) as well as oxygen ionic conductivity. The use of ambivalent (e.g., $X^{+3/+4}$ or $X^{+2/+3}$) dopants has also been explored for imparting additional electronic conductivity. [36] A-site transition-metal-doped perovskite oxides with formula $A_{1-x}Sr_xCo_{1-y}B_yO_{3-a}$ (A = La, Ba and B = Cr, Mn, Fe, Co) display significantly higher oxygen-ion conductivities exceeding that of yttria-stabilized zirconia (YSZ), [35] making them the leading class of materials considered for SOFC electrodes. [37-38] Higher oxygen-ion conductivities comparable to YSZ were also reported by Weber [39] and Takita, [40] based on perovskite structure with La^{+3} in the A-site. Electrochemical performance of $La_{0.8}Sr_{0.2}MnO_{3-\delta}$–YSZ (LSM–YSZ), $La_{0.6}Sr_{0.4}Co_{0.8}Fe_{0.2}O_{3-\delta}$ (LSCF), and $La_{0.8}Sr_{0.2}FeO_{3-\delta}$ (LSF) electrodes were studied under high temperature co-electrolysis of CO_2 and H_2O; LSCF electrodes were found to have the highest performance. [27] Teraoka et al. first demonstrated high oxygen

permeation flux through a Co-containing perovskite composition, [41-42] displaying high oxygen-ion conductivities. A high oxygen flux was also observed by operating dense ceramic membranes especially with a large series of mixed-conducting acceptor-doped perovskites ($La_{1-x}Sr_xCoO_{3-\delta}$, $La_{1-x}Sr_xFeO_{3-\delta}$, $La_{1-x}Sr_xCo_{1-y}Fe_yO_{3-\delta}$, $CaTi_{0.8}Fe_{0.2}O_{3-\delta}$) at 800-1000$^oC$. [43]

1.2.3 SOFC/SOEC applications based on MIEC electroceramics

Catalytic electroceramics promise multiple potentially transformative solutions to a broad range of environmental and energy challenges in the 21st century [44-48]. Oxygen-conducting membranes employing mixed ionic-electronic conducting (MIEC) materials enable oxygen separation from air in support of clean combustion [49-50], or selective oxygen coupling with light hydrocarbons for enhanced utilization of natural gas and refinery gases [51-52]. Recently, global climate change has caused plenty of abnormal temperature rising events, which may be partially caused by the increasing greenhouse gasses (GHG) emissions. Carbon dioxide, mainly emitted from fossil fuel power plants, is the most common greenhouse gas and for this reason there has been a lot of research focusing upon the capture, decomposing and removal of CO_2. [53-56] Renewable energy source has been developed due to dwindling fossil source, growing need of petroleum products, and environmental concerns. [57-58] Hydrogen has been treated as an important alternative energy carrier. Hydrogen production can be achieved by a steam electrolysis process ($H_2O \rightarrow H_2 + 1/2\ O_2$) via SOECs. [59-60] Beside hydrogen, oxygen and carbon monoxide can also be produced by electrolyzing carbon dioxide ($CO_2 \rightarrow CO + 1/2\ O_2$). [61-62] This approach has been investigated to produce

oxygen by NASA. [63-65] CO_2 could be reused and recycling from energy system or capture from air to produce synthetic hydrocarbon fuels. [66] The basic principle for a CO_2 electrolysis cell is shown in Figure 1.2.

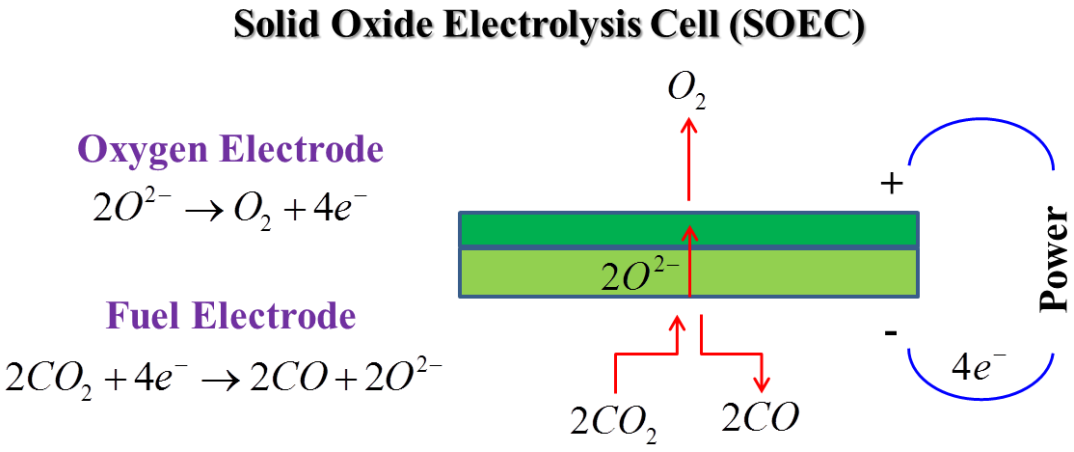

Figure 1.2: Schematic of a CO_2 Solid Oxide Electrolysis Cell (SOEC).

In recent years, solid-oxide electrolytic cells employing catalytic MIEC electrodes capable of converting waste heat, H_2O and CO_2 from combustion processes into syn-gas have been investigated as a novel means of producing synthetic fuels or petrochemicals while minimizing greenhouse gas emissions [67-69]. Solid oxide reversible fuel cells utilizing catalytically active MIEC materials support the large-scale storage of electrical energy generated by inherently transient and CO_2-free renewable energy sources such as wind, solar and tidal energy harvesting by providing a means to chemically store excess electrical energy by via reduction of CO_2 to CO, with subsequent electrical power generation via CO electrochemical oxidation at high efficiencies during peak power loads or low power generation periods [70-73]. SOECs

have also received significant recent interest due to their ability to generate H_2 through electrolysis of H_2O at greater energy efficiencies than photo-catalytic or thermochemical water splitting techniques [74-76]. The H_2 produced can be utilized as an alternative fuel convertible to electrical energy by fuel cells at competitive efficiencies with zero emissions at the point-of-use [77-78].

SOEC and SORFC development largely relies upon the discovery of inherently multi-functional materials capable of providing the requisite catalytic and electrochemical properties while retaining material and mechanical stability under harsh reducing environments uncommon to traditional SOFC cathodes. Specifically, there is a need to significantly improve SORFC efficiency and stability under both CO-oxidation and CO_2-reduction conditions. Recent research has focused on catalytic transition metal dopants to achieve new combinations of catalytic, ionic and electronic properties [79-80]. Currently reported high-performance MIEC materials including $La_xSr_{1-x}MnO_{3+\alpha}$ (LSMO), $La_xSr_{1-x}Co_yFe_{1-y}O_{3+\alpha}$ (LSCF) are capable of combining competitive oxygen-ion and electrical conductivities with high stability under oxidizing conditions, making them excellent candidates for SOFC cathodes [81-84]. However, the stability of these A-site doped MIECs under reducing atmospheres limits their viability in SOEC or oxygen-conducting membrane reactor applications [85-86].

1.2.4 Fe-based perovskites

The synthesis and characterization of $Ba(Ce_yZr_{1-y})O_3$ with Co as the sole dopant has recently been reported. [33] The overarching goal of that study was to incorporate period-IV transition metal ($Co^{+2/+3}$) in HTPCs in order to develop bi-functional,

homogeneous materials combining catalytic activity for hydrogen generation from liquid fuels (e.g. CH_3OH) with mixed protonic-electronic conductivity, for simultaneous non-galvanic hydrogen purification. However, the Co-doped system was limited by poor stability under wet reducing atmospheres. [34] In the literature, Fe-doped materials were demonstrated to display higher stability under reducing atmosphere at high temperatures in fuel cell applications and oxygen permeation membrane developments: 1) Fe-doped $La_xSr_{1-x}TiO_3$ showed high stability and mixed conductivity suitable for potential SOFC anode materials; [87] 2) Fe-doped $LaGaO_3$ exhibited high oxygen permeation rates and high stability against reduction; [88] 3) A recent study showed Fe-doped perovskite and double-perovskite type materials ($BaMg_{0.33}Nb_{0.34}Fe_{0.33}O_{3-\delta}$, $Ba_2Ca_{0.66}Nb_{0.68}Fe_{0.66}O_{6-\delta}$) exhibited excellent long-term chemical stabilities under CO_2 and SO_2 atmospheres for solid-state gas-sensor applications. [89]

Recently, catalytic transition-metal dopants were applied to achieve new combinations of catalytic, ionic and electronic properties. [90-91] The Fe-based perovskites have been associated with different crystal systems, depending on such factors as the synthesis technique and processing temperature. The structure at higher temperatures would also be expected to be a function of the oxygen partial pressure because of the changing concentration of oxygen-ion vacancies (δ). [92] Perovskite-based oxides from the Ba-Sr-Co-Fe-O (BSCF) and La-Sr-Co-Fe-O (LSCF) systems, with Fe on the B-site, have been studied as cathodes for oxygen-ion-conducting SOFCs. [93-94] In comparison, there are fewer studies documenting the role of Fe as a dopant in $BaCeO_3$ and $BaZrO_3$. Tao et al. [95] have investigated $BaCe_{1-x}Fe_xO_{3-\delta}$ as cathodes for

proton-conducting SOFCs. Zhu et al. [96-97] have studied $BaCe_{1-x}Fe_xO_{3-\delta}$ as oxygen-permeable membranes. Babilo and Haile [98] have investigated the role of 4 mol% Fe as a sintering aid in $BaZr_{0.85}Y_{0.15}O_{3-\delta}$. In a recent study, Escolastico et al. [99] have reported the structure, transport properties and chemical stability of $BaZr_{0.80}Y_{0.15}M_{0.05}O_{3-\delta}$ (M = Fe, Pr and Mn). Fe-doped $CaTiO_3$ was developed for oxygen permeation study while the oxygen permeation flux for a membrane thickness of 1.0 mm at 900^oC was very low (0.02 $mL/(min \cdot cm^2)$). [100] Fe-based catalysts have established catalytic surface activities for syn-gas production and Fischer-Tropsch synthesis of hydrocarbons [101-104], while Fe oxide catalysts are known to preferentially chemisorb CO_2 via formation of surface CO_3^{2-} groups via reaction with available O^{2-} ions [105-106]. In addition, Fe-doped materials were demonstrated to display higher stability under reducing atmosphere at high temperatures typical of fuel cell or oxygen permeation membrane conditions. Fe-doped $La_xSr_{1-x}TiO_3$ was shown by Fagg et al. to have high stability and mixed conductivity suitable for potential SOFC anode materials [87] while high oxygen permeation rates combined with high materials stability against reduction were demonstrated for Fe-doped $LaGaO_3$ [88].

1.2.5 Oxygen permeation

Since Nernst observed ionic conductivity in ceramics in 1899 [107], perovskite oxide type MIECs have been studied with high interest as potential high performance oxygen separators and oxygen sensors. [108-117] MIECs are widely used as electrolytes in solid oxide fuel cells (SOFCs) applications, where current flow occurs by the migration of oxygen ions and electrical holes/electrons. Oxygen molecules can occupy

the oxygen vacancy sites to form lattice oxygen on the oxygen-rich side, followed by an oxygen ionic transportation process to the oxygen-lean side. The driving force of oxygen transportation through the thickness of membrane is the difference of oxygen partial pressures on both sides, which contributes to an ionic and electronic gradient. After migrating through the membrane, oxygen ions are released from the lattice to reproduce mobile oxygen molecules on the oxygen-lean side. The key advantage of this process is that no external circuits are required to drive the oxygen transport if there is a chemical potential gradient. Thus, MIEC membranes can exhibit infinite selectivity to oxygen in theory, which makes it a potential candidate material for oxygen purification.

Perovskite-type oxide membrane with chemical formula $La_{1-x}Sr_xCo_{1-y}Fe_yO_{3-\delta}$ was first reported to separate oxygen from air at high temperature up to 1150 K by Teraoka et al. in 1985 [118], with the primary summary that the oxygen permeability was mainly controlled by the concentration of oxygen vacancies. Zirconium-doped (B-site) perovskite-type oxide membranes of $BaCo_{0.4}Fe_{0.6-x}Zr_xO_{3-\delta}$ (x=0-0.4) were investigated for oxygen permeation in the temperature range 600-950^{o}C by Tong et al. [119] and the highest oxygen permeation flux was 0.90 mL/(min·cm^2). Zhao et al. [120] studied barium-doped (A-site) perovskite membranes $Ba_xSr_{1-x}Co_{0.8}Fe_{0.2}O_{3-\delta}$ (x=0-1.0) and the highest oxygen permeation flux reported was 1.19 mL/(min·cm^2) at 850^{o}C. Above results showed both A-site and B-site dopants of the mixed conducting perovskites had great influence on the phase structure, materials stability and oxygen permeability. Oxygen permeation performance as well as materials microstructure was examined on $Ba_{0.5}Sr_{0.5}Co_{0.8}Fe_{0.2}O_{3-\delta}$ (BSCF) oxides synthesized by different methods

(solid-state reaction, modified citrate, and citrate-EDTA complexing) under the same sintering technique by Tan et al. [121] The membrane prepared by solid state reaction exhibited the highest oxygen permeability. Oxygen permeability was also found to be improved by surface modification. Ga-doped perovskite with high structural stability only showed limited oxygen permeability, but the measured oxygen flux increased to be comparable with a Co-based membrane by adding a catalytically surface-reactive $La_{0.6}Sr_{0.4}CoO_{3-\delta}$ (LSC) layer on its surface. [122] Surface effect on dense mixed conducting $La_{0.1}Sr_{0.9}Co_{0.9}Fe_{0.1}O_{3-\delta}$ was investigated by Kusaba et al. [123] It showed that the increase of surface area in the oxygen-lean side had more significant effect on increasing oxygen permeability than the increase of surface area in the oxygen-rich side. High oxygen permeation flux could be achieved on a Co-based perovskite membrane, but the materials stability remained as a concern due to the evaporation and reduction of cobalt. [124-126] In contrast, reduction potential of Fe is lower than that of Co, contributing to high materials stability under reducing environments. Moreover, Fe-based perovskite membrane exhibited high oxygen permeability, which attracted researchers' attentions during the past decade. [127-128] Recently, the successful development of hollow fibre perovskite membranes also gained plenty of interests towards their industrial applications for their highest oxygen permeability know so far and long-term materials stability in oxygen separators and membrane reactor converting natural gas into syn-gas. [129-131]

1.2.6 Mixed protonic and electronic conducting perovskites

Mixed ionic-electronic conducting electroceramic materials have received increasing interest as high-temperature hydrogen separation membranes for use in catalytic membrane reactors for natural gas conversion and as electrolytes in proton-conducting intermediate-temperature solid-oxide fuel cells (SOFCs). [132-135] Since the first report of proton conduction in perovskite (ABO_3) type $SrCeO_3$ at high temperatures ($\geq 600^oC$) by Iwahara et al. [136] in 1981, several acceptor-doped barium cerates and barium zirconates ($BaCe_xM_{1-x}O_{3-\delta}$ and $BaZr_xM_{1-x}O_{3-\delta}$, M = Sc, Y, Nd, Gd, Yb, etc.) have been investigated as high-temperature protonic conductors in connection with hydrogen separation or SOFC applications [137-140]. The primary mechanism to produce protons in these materials has been identified as the interaction between water vapor and oxygen vacancies, the latter being generated in the oxide via charge compensation required by the presence of trivalent cations (M^{3+}) at the B-site (B^{4+}). [141] Electronic conduction is introduced by doping with a multivalent cation (e.g., transition metal), which enables free electron transport from a low-oxidation-state cation to a high-oxidation-state cation in its neighborhood, i.e. the "small polaron" mechanism [142]. The key advantage of the resulting mixed ionic-electronic conducting membrane is that no external circuits is needed, thus offering an economic solution in comparison to power-based technologies for hydrogen production. [143]

1.2.7 Hydrogen permeation

Significant research has been conducted on mixed ionic-electronic conducting perovskite-type materials for hydrogen separation. [144-154] Li et al. [155] measured

the hydrogen permeation flux through $BaCe_{0.9}Mn_{0.1}O_{3-\delta}$ membranes with thickness 1.6 mm. The resulting flux was 0.011 mL/(min·cm^2) at 900^{o}C and was shown to be controlled by surface kinetics. Qi et al. [156] studied electrical conductivity and hydrogen permeation on mixed conducting $SrCe_{0.95}Tm_{0.05}O_{3-\delta}$ membrane and its highest hydrogen flux was reported to be ~0.04 mL/(min·cm^2) at 900^{o}C using 10% H_2 in the feed and 20%O_2 in the sweep. Effect of Zr doped Ni-$BaCe_xY_{1-x}O_{3-\delta}$ was investigated by Zuo et al. [157] in which hydrogen flux was promoted by addition of water vapor in the feed. Likewise, Cai et al. [158] showed that the hydrogen permeation flux under wet conditions was higher due to the increased proton concentrations. Hamakawa et al. [159] reported the H_2 permeation rates were proportional to the inverse of the membrane thickness even on a 2 μm thin film of $SrCe_{0.95}Yb_{0.05}O_3$, indicating that permeation is controlled by bulk diffusion and not by surface chemisorption or boundary transport. Song et al. [160] studied hydrogen permeation for Ni-$BaCe_{0.8}Y_{0.2}O_{3-\delta}$ and found the hydrogen permeation flux were due to ambipolar diffusion, which dominated over the entire examined temperature range (600-900^{o}C). Mather et al. [161] found that the hydrogen permeability could be largely improved by coating a porous Pt catalyst layer on the feed-exposed $Sr_{0.97}Ce_{0.9}Yb_{0.1}O_{3-\delta}$ membrane. Recently, Song et al. [162] investigated hydrogen permeation as well as oxygen permeation in Co-doped $BaCe_{0.85}Tb_{0.05}Co_{0.1}O_{3-\delta}$ (BCTCo) perovskite membrane (dual ion conducting membrane). The reported hydrogen flux reached 0.385 mL/(min·cm^2) at 1000^{o}C under 50% H_2/inert and the oxygen flux reached 0.122 mL/(min·cm^2) at 1000^{o}C under Air/He. In addition, a newly released finding showed a hydrogen flux as high as ~4.1

mL/(min·cm^2) at 800^{o}C for the $Sr(Ce_{0.6}Zr_{0.4})_{0.85}Y_{0.15}O_{3-\delta}$/Ni-$Sr(Ce_{0.6}Zr_{0.4})_{0.85}Y_{0.15}O_{3-\delta}$ hydrogen transport membrane, which increased the magnitude of reported H_2 permeation flux to a higher level. [163]

In addition to hydrogen permeation rates, membrane chemical stability is a key factor in identifying suitable hydrogen separation materials and electrolysis cell. Specifically, suitable materials must exhibit high chemical stability not only under reducing (H_2) environments, but also in the presence of gaseous species that commonly associated with hydrogen containing mixture gasses (e.g. H_2O, CO_2, SO_2, and NO_x). Solid-oxide electrolysis cells (SOECs) employing perovskite electrodes have been investigated as a novel means of producing hydrogen fuels or petrochemicals. [67,69] Solid-oxide reversible fuel cells (SPRFCs) with oxygen ion conducting and/or proton conducting electrolyte support the large-scale storage of electrical energy by providing a means to chemically store excess electrical energy. [72-73] Among similar chemical formulas, $BaCeO_3$ based materials showed high protonic conductivity under hydrogen containing environments [164], but their chemical stability under steam and CO_2 were reported to be poor. [165-167] A group of Zr-doped $BaCeO_3$ materials was investigated in order to mitigate the materials degradation pathways under CO_2- and steam-containing environments and the results showed that the chemical stability increased with increasing Zr amount in the doped materials. [139,157,168-169] However, hydrogen permeability data for $BaZrO_3$-based materials remains sparse.

1.3 Motivation

The authors have previously demonstrated Co-doped $Ba(Ce_yZr_{1-y})O_3$ to be an attractive electroceramic catalyst with mixed ionic-electronic conducting properties suitable for clean energy application [33]; however the stability of this material against hydrolysis degradation under humid reducing environments was found to be poor, as attributed to the low reduction potential of Co dopant and susceptibility of Ce to incorporate hydroxyl ions – both of which enable rapid degradation via Ba hydrolysis [34]. Based upon the above reviews, Fe-doped $BaZrO_3$ was selected for achieving a combination of high catalytic activity and material stability in various atmospheres at high temperatures. Barium was retained in the A-site to provide high oxygen permeation flux and long-term stability compared with other alkaline-earth metals because Ba is known to increase the lattice free volume and reduce the average metal-oxygen bond energy within the lattice. [170] Removal of Ce, such that Zr remains the sole undoped B-site cation, was selected in order to eliminate materials-degradation pathways under moist and CO_2-containing environments. Fe was selected as group IV dopant over Co owing to its lower reduction potential (Fe^{+2} to Fe^0 vs. Co^{+2} to Co^0) for greater materials stability. Recent studies have focused on the structural and functional properties of $BaZrO_3$ upon doping with cations not commonly associated with the application of the material for high-temperature protonic conductivity [99, 171-173] and although sintered $BaZrO_3$ has been reported to display high grain-boundary resistance and brittleness, it was selected as the base oxide because of its greater chemical stability relative to $BaCeO_3$. [174] Lanthanide dopants employed in barium zirconates have been studied

focusing upon realizing proton-conducting MIECs, [175-176] but the research of transition-metal-doped $BaZrO_3$ materials exhibiting mixed oxygen ionic-electronic conductivities are rare. However, no report has been presented to-date, on the properties of $BaZrO_3$ with Fe as the sole dopant.

A concurrent investigation, the basis for this dissertation, was therefore carried out on Fe-doped $BaZrO_3$, in which Fe dopant substitutes preferentially at the B-site, with an emphasis on material stability. Specifically, electrocatalytic investigation of Fe-doped $BaZrO_3$ was carried on over a full cycle of oxidizing and reducing environments expected for both SOEC and SORFC applications, followed by detailed materials analysis of the as-exposed material to assess the final, stable reduced perovskite microstructure and composition. Moreover, the Fe-doped $BaZrO_3$ material was investigated for oxygen permeation and hydrogen permeation studies. Results thus provide valuable insight into the underlying electrochemical mechanisms present as well as the long-term materials stability of acceptor-doped perovskites under both oxidizing and reducing environments.

1.4 Defect chemistry in $BaZr_{0.9}Fe_{0.1}O_{3-\delta}$ perovskite

The oxygen-transport properties and electrical conductivity of an electroceramic are dictated by the defect chemistry of the material. For the present analysis of $BaZr_{0.9}Fe_{0.1}O_{3-\delta}$, defect chemistry is employed to describe p-type and n-type electrical conduction as well as oxygen ion conduction for subsequent analysis. Kröger-Vink notation [177] is employed to denote defect species concentrations of mobile oxygen

vacancies ($[V_O^{\bullet\bullet}]$), electron holes ($[h^{\bullet}]$), mobile electrons ($[e']$), and Fe^{3+} cation substitution for Zr^{4+} ($[Fe'_{Zr}]$).

The global electro-neutrality condition over the whole crystal is described by the following equation:

$$p + 2[V_O^{\bullet\bullet}] = n + [Fe'_{Zr}] \tag{1.2}$$

where *p* denotes the concentration of mobile holes and *n* denotes the concentration of mobile electrons. Based upon the assumption that the concentration of electronic defects (intrinsic defects) is very small in comparison to that of the ionic defects (dopants) [178], Equation 1.2 reduces to:

$$2[V_O^{\bullet\bullet}] \cong [Fe'_{Zr}] \tag{1.3}$$

At sufficient oxygen activities, molecular O_2 may be absorbed by the lattice to generate electron holes (Scheme I). The equilibrium between gaseous oxygen and oxygen vacancy defects in the solid phase can be expressed by:

$$\frac{1}{2}O_2(g) + V_O^{\bullet\bullet} \leftrightarrow O_O^X + 2h^{\bullet} \tag{1.4}$$

$$K_{oxid} = \frac{[O_O^X][h^{\bullet}]^2}{pO_2^{1/2}[V_O^{\bullet\bullet}]} \cong \frac{p^2}{[V_O^{\bullet\bullet}]}\, pO_2^{-1/2} \tag{1.5}$$

where K_{oxid} denotes the equilibrium constant of Reaction 1.4. The electrical conductivity can be determined by the product of the fractional concentration of mobile holes, the charge of a hole, and the mobility of the holes, μ_p.

$$\sigma_p = p \cdot e \cdot \mu_p \tag{1.6}$$

The combination of Equation 1.5 and 1.6 gives the p-type conductivity dependence:

$$\sigma_p \propto p = (const)\, pO_2^{1/4} \tag{1.7}$$

Similarly, under low pO_2 conditions, oxygen exchange from the solid to gas phase (Scheme II), equilibrium constant, and with corresponding n-type conductivity dependence can be derived from the equilibrium expression:

$$O_O^X \leftrightarrow \frac{1}{2} O_2(g) + V_O^{\bullet\bullet} + 2e' \tag{1.8}$$

$$K_{red} = \frac{pO_2^{1/2}[V_O^{\bullet\bullet}][e']^2}{[O_O^X]} \cong n^2 [V_O^{\bullet\bullet}] pO_2^{1/2} \tag{1.9}$$

$$\sigma_n \propto n = (const)\, pO_2^{-1/4} \tag{1.10}$$

where K_{red} is the equilibrium constant of Reaction 1.8 and n donates the concentration of mobile electrons.

The above analysis assumes a constant ionic mobility, μ_i , primarily from oxygen-ion vacancies transport, as the dopant concentration remains fixed in this study. Likewise, the ratio of lattice oxygen to vacancy is assumed constant, such that the total conductivity may be written as a function of oxygen partial pressure:

$$\sigma_{total} = \sigma_n + \sigma_{ion} + \sigma_p = \sigma_n^0 pO_2^{-1/4} + \sigma_{ion} + \sigma_p^0 pO_2^{1/4} \tag{1.11}$$

This equation implies the shape and corresponding slope of the log-log plots of σ versus pO_2. At different pO_2, the conductivity may be dominated by electrical holes, dopant concentration, or electrons. This review of mechanism will be revisited in subsequent chapter for interpretation of electrochemical data.

1.5 Dissertation outline

This dissertation aims to investigate Fe-doped $BaZrO_3$ perovskite (BZF10) for simultaneous electrochemical and catalytic activities and membrane separation applications, with long term mechanical and chemical stability especially under high temperature humidified reducing atmospheres.

Chapter 2 primarily focuses upon BZF10 powder synthesis and pellet fabrication techniques as well as the materials characterization on BZF10 in terms of general physical properties (i.e. density, porosity), elemental analysis, synchrotron X-ray diffraction (HR-XRD), transmission electron microscopy (TEM), and scanning transmission electron microscopy coupled with energy dispersive X-ray spectroscopy (STEM-XEDS).

Chapter 3 presents the electrical conductivity relaxation (ECR) measurement and oxygen permeation test on dense BZF10 disk. Using ECR technique, transient electrical conductivity data is normalized and fitted to a one-dimensional, cartesian solution of Fick's second law assuming surface electrochemical reaction of 1^{st}-order dependence upon oxygen-ions. The variable parameters obtained by this fitting are the bulk ionic diffusion coefficient D_v (m^2/s) and the surface exchange coefficient k' (m/s).

Chapter 4 reports the investigation of Fe-doped $BaZrO_3$ over a full cycle of oxidizing and reducing (dry O_2, dry CO_2, humidified inert Ar, CO and H_2, then back to dry O_2) environments expected for both SOEC and SORFC applications. Specifically, the electrochemical and catalytic behavior of Fe-doped $BaZrO_3$ is examined, thus

providing valuable insight into the underlying electrochemical mechanisms present as well as the surface reactions under both oxidizing and reducing conditions.

Chapter 5 describes the detailed materials characterizations (HR-XRD, TEM, STEM-XEDS) on the as-exposed BZF10 pellet to assess the final, stable reduced perovskite microstructure and composition. Results thus demonstrate the long-term materials stability of acceptor-doped perovskites under both oxidizing and reducing environments.

Chapter 6 shows the hydrogen permeability of BZF10 membrane. Results show that in the examined thickness (0.97-1.40 mm), bulk diffusion is the rate-limiting step and the hydrogen permeation flux is comparable to other perovskite membranes. BZF10 membrane shows high mechanical and chemical stability over both dry and humidified hydrogen containing gas environments at 600-900^{o}C. Chapter 7 contains primary conclusions of this dissertation and recommendations for future work.

2. SYNTHESIS AND STRUCTURAL CHARACTERIZATION OF IRON-DOPED BARIUM ZIRCONATE*

2.1 Introduction

This chapter primarily focuses upon $BaZr_{0.90}Fe_{0.10}O_{3-\delta}$ (BZF10) powder synthesis and pellet fabrication techniques as well as the materials characterization on BZF10 in terms of general physical properties (i.e. density, porosity), elemental analysis, crystal structural analysis via synchrotron X-ray diffraction (HR-XRD) and transmission electron microscopy (TEM), and elemental mapping via scanning transmission electron microscopy coupled with energy dispersive X-ray spectroscopy (STEM-XEDS).

There are 5 primary techniques employed in metal oxides synthesis including solid state reaction, co-precipitation, Sol-gel, hydrothermal, and spray and freeze drying methods. [49] Solid state reaction is the most common and easily handled method by mixing and sintering the appropriate amount of the precursor compounds; while the homogeneity and purity of the synthesized powder is limited and high temperature (usually above $1200^{o}C$) is required. Co-precipitation method requires an aqueous solution of the target cations and that of the precipitating agent; the homogeneity and purity of the synthesized powder is improved and the sintering temperature decreases in comparison to solid state reaction. Sol-gel methods enable precise control over target

* Part of this chapter is reprinted with permission from "Materials Synthesizing, Electrochemical Characterization and O_2 Permeation Properties of Fe-Doped Barium Zirconates" by H. Zhang et al. / Solid State Ionics 266 (2014) 58–67, http://dx.doi.org/10.1016/j.ssi.2014.08.011.

composition thus high homogeneity and purity is expected. Hydrothermal, and spray and freeze drying techniques are non-conventional methods and are still in early stages of development. The synchrotron XRD data collected on as-synthesized BZF10 powder indicate a primary $BaZrO_3$-based cubic structure with high purity after synthesized by solid state reaction. BZF10 material prepared via solid state reaction also maintains good chemical and mechanical stability after humidified reducing gas exposures, as discussed in Chapter 5. Moreover, larger grain size can be achieved via solid state reaction, which can facilitate the gas separation process. Therefore, solid state reaction is chosen as the primary method for BZF10 powder synthesis.

2.2 Experimental

2.2.1 Powder synthesis and characterization

Powders of target composition $BaZr_{0.90}Fe_{0.10}O_{3-\delta}$ (BZF10) were synthesized via solid-state reaction using metal nitrates as precursors. 9.60 g of $Ba(NO_3)_2$ (Sigma-Aldrich, 99+%, A.C.S. reagent), 11.22 g of $ZrO(NO_3)_2 \cdot 6H_2O$ (Aldrich Chemistry, 99%), and 1.48 g of $Fe(NO_3)_3 \cdot 9H_2O$ (Sigma-Aldrich, ACS reagent, $\geq$ 98%) were mixed and ground into powder with mortar and pestle. The blended powder was heat-treated in an alumina crucible (Coorstek) under stagnant air at 1150^{o}C for 4 hours, with heating and cooling rates of 5^{o}C/min, followed by addition of acetone and grinding for 10 minutes to homogenize the partially calcined powder, followed by drying at 120^{o}C for 1 hour. The powder was subsequently heat-treated at 1600^{o}C for 12 hours on a Pt foil (Surepure Chemetals, 2″ × 2″ × 0.01″) inside an alumina crucible with heating and cooling rates of

5^{o}C/min to achieve complete calcination. Lastly, the dry product was ground into a homogeneous powder (9.39 g), as shown in Figure 2.1. Elemental analysis of as-synthesized BZF10 powder via Proton Induced X-ray Emission (PIXE) was provided by Elemental Analysis Inc. (KY, USA), and employed for quantitative determination of Ba, Zr and Fe concentrations. The as-synthesized powder was also characterized by synchrotron X-ray diffraction analysis using a scan rate of 0.6^{o}/min and a scan range of $0.5^{o} \leq 2\theta \leq 50^{o}$, provided using the mail-in program at Advanced Photon Source, Argonne National Lab (IL, USA).

Figure 2.1: Synthesized BZF10 powder under 12 hours heat-treatment at 1600^{o}C.

2.2.2 Pellet preparation and characterization

Cylindrical pellets for electrochemical analysis were produced by pressing 0.5g of BZF10 powder at 221.5 MPa for 1 minute with a hydraulic press (Carver, 4555) using

a 13mm die (Carver, 3619), followed by sintering on a Pt foil at 1700^{o}C for 4 hours with heating and cooling rates of 3^{o}C/min. Both faces of the as-sintered pellet were polished with coarse abrasive paper (Buehler Ltd., Grit 60/P60) to remove any surface products formed during sintering.

Porosity and pore-size of the resulting 13mm BZF10 pellets were measured using a Hg Porosimeter (Quantachrome, model # PM-33-17-LP) with pressure range 20.08-3.315×10^{4} psi. Density of 13mm BZF10 pellets was measured via Archimedes test using a Mettler-Toledo density determination kit (Catalog # 33360) as follows. First, the pellet was weighed in air (m_A), then after immersion in ethanol (Koptec, 99.5%) (m_B). The temperature of air and ethanol was used to obtain fluid densities $\left(\rho_{air}, \rho_{C_2H_5OH}\right)$; the density of the pellet $\left(\rho_{BZF10}\right)$ was then calculated using Equation 2.1:

$$\rho_{BZF10} = \frac{m_A}{m_A - m_B}\left(\rho_{ethanol} - \rho_{air}\right) + \rho_{air} \tag{2.1}$$

Microscopy analysis of fracture cross-section of the as-sintered BZF10 pellet and its chemical maps were investigated by transmission and scanning transmission electron microscopy (TEM & STEM) coupled with energy dispersive X-ray spectroscopy (XEDS). Cross-section TEM specimens were prepared by manual grinding and thinning of fractured samples, followed by dimpling and subsequent ion milling (Gatan PIPS 691 ion polishing system, 3.7 keV) to achieve suitably thin (electron-transparent) specimens. A TEM (FEI Tecnai G2 F20 ST microscope with a point resolution of 0.24 nm) operated at 200 kV and a TEM–STEM attachment of the same microscope operated at 200 kV were used for conventional and analytical imaging of the sample, respectively. Dense

cylindrical membranes of thickness 1.20 mm were prepared in similar fashion by pressing 3.5g of BZF10 powder in 25mm die (Carver, 4369) at 199.6 MPa for 1 minute and sintering at 1700^{o}C for 4 hours with heating and cooling rates of 3^{o}C/min, followed by polishing to remove any surface contaminates.

2.3 Results and discussion

2.3.1 Powder properties

Results of the elemental analysis are presented in Table 2.1, which yields an observed powder composition of $Ba_{0.90}Zr_{0.90}Fe_{0.10}O_{3-\delta}$. A very small amount of Hf was detected, which could be explained based on its occurrence as a common impurity in Zr compounds as reported elsewhere. [179] The resulting composition indicated the possibility of a Ba-deficient, B-site doping perovskite structure of the powder sample, or a combination of A- and B-site co-doping by Fe cation. Using density functional calculations and thermodynamic modeling, the distribution of dopants in perovskites has been found to be mainly governed by ionic radii size [180]. A comparison of the ionic radii of Fe^{2+} and Fe^{3+} (78pm and 65pm, respectively) with that of Ba^{2+} and Zr^{4+} (161pm and 72pm, respectively) would suggest primarily B-site acceptor doping. Sublimation of BaO at the processing temperatures used in the present study (1600^{o}C) may be expected [98] and could be the primary reason for Ba deficiency in the powder. It has been suggested [181] that a divalent-ion deficiency in doped alkaline-earth metal zirconates may drive the dopant incorporation onto the A-site instead of the intended B-site due to the effect of cation nonstoichiometry. PIXE suggests Fe substitutes at both A- and B-

sites, corresponding to n-type and p-type semi-conduction behavior, respectively, with an A:B ratio ~1.

Table 2.1: Results of elemental analysis performed using PIXE.

Element	**Mass %**	**Mole %**
Ba	36.498	0.266
Zr	24.179	0.265
Fe	1.608	0.029
Target composition = $BaZr_{0.90}Fe_{0.10}O_{3-\delta}$ Observed composition = $Ba_{0.90}Zr_{0.90}Fe_{0.10}O_{3-\delta}$		

The high resolution XRD pattern obtained from the BZF10 powder is presented in Figure 2.2a. In this pattern, all the visible primary peaks could be indexed with high accuracy to a cubic perovskite phase with a lattice parameter of *a* ~4.19 Å, which should be compared with the values reported for cubic $BaZrO_3$. From the JCPDS Set-Card, the reported lattice parameters for cubic $BaZrO_3$ are 4.193 Å (PDF# 06-0399), 4.197 Å (PDF# 70-3667), and 4.182 Å (PDF# 74-1299), which is in excellent agreement with the value we obtained for BZF10, due to the closer ionic radius of Zr^{4+} (72 pm), Fe^{2+} (78 pm) and Fe^{3+} (65 pm). All primary peaks showed no splitting or distortion towards the identified perovskite phase, which indicated a structure with high stability.

Figure 2.2b presents low-angle XRD data used to study the minor features in the material. The d-spacing values which could not be indexed to the primary cubic phase were identified as secondary phases presented in Table 2.2. Those secondary phases

matched with patterns reported for materials from the Ba-O, Zr-O, Fe-O and Ba-Fe-O systems in the JCPDS Set-Cards. All the secondary features are identified as a combined BaO, ZrO_2 and $BaFeO_{3-x}$ phases, but their low concentrations confirm that this material is relatively pure.

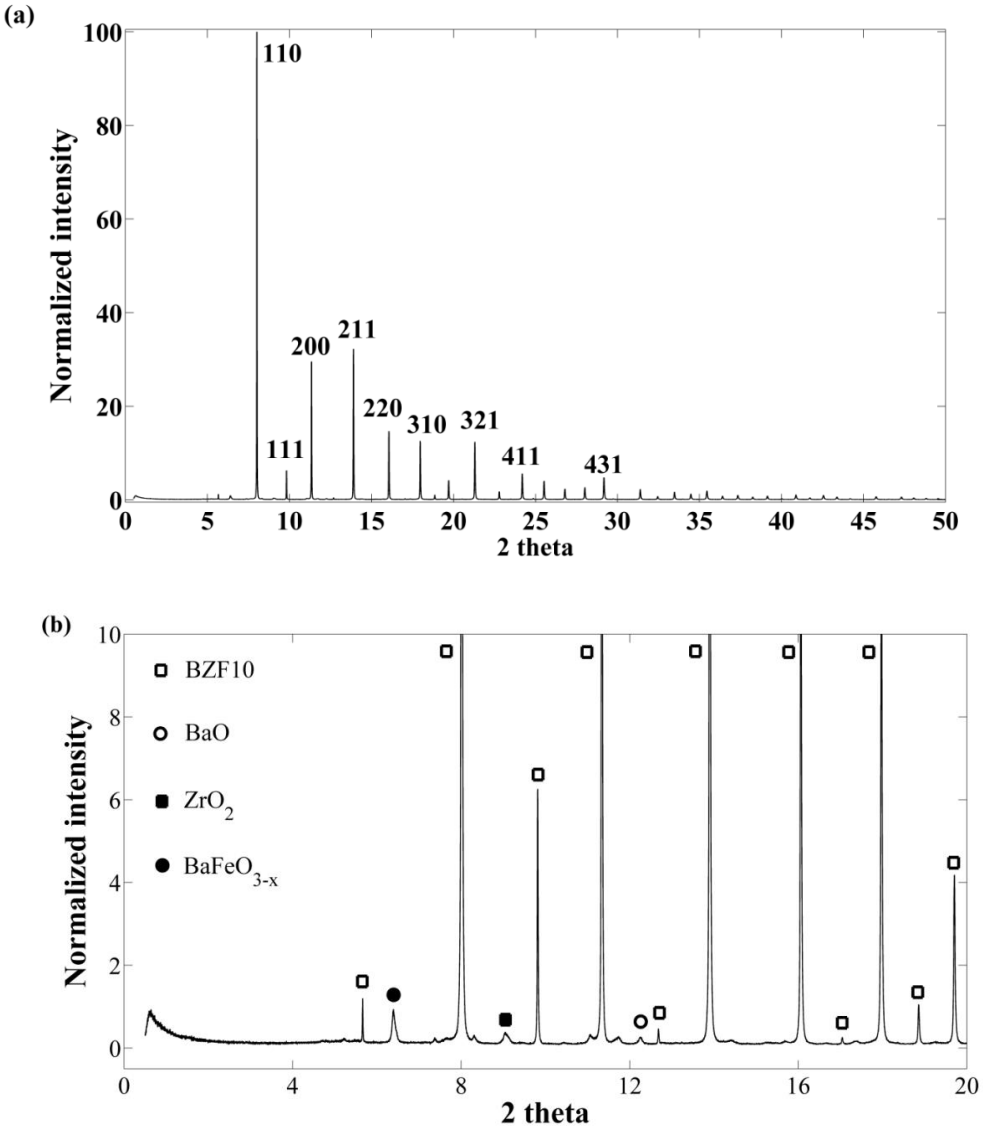

Figure 2.2: (a) Synchrotron X-ray diffraction pattern of BZF10 powder after heat-treated at 1600^{o}C for 12 hours; (b) Low 2-theta range of part (a).

Table 2.2: Reported and measured d-spacing values.

Observed d-spacings (Å) (Secondary phases)	3.711	3.221	2.857	2.623	2.147	2.023	1.935
Reported d-spacings (Å) BaO (PDF#01-0746)		3.200 (111)	2.750 (200)				1.950 (220)
Reported d-spacings (Å) ZrO_2 (PDF#65-2357)		3.207 (-111)	2.871 (111)	2.635 (020)		2.021 (-202)	
Reported d-spacings (Å) FeO (PDF#06-0615)					2.153 (200)		
Reported d-spacings (Å) Fe_2O_3 (PDF#16-0653)		3.240 (022)		2.573 (-213)	2.176 (521)	2.018 (050)	1.973 (-441)
Reported d-spacings (Å) $BaFeO_{2.9}$ (PDF#25-0068)	3.700 (105)		2.845 (110)		2.099 (207)	2.013 (208)	
Reported d-spacings (Å) $BaFeO_{2.6}$ (PDF#39-0183)	3.680 (003)		2.876 (150)	2.600 (230)	2.113 (054)	2.015 (208)	1.977 (073)
Reported d-spacings (Å) $BaFeO_3$ (PDF#74-0646)	3.700 (015)		2.845 (110)		2.098 (027)	2.015 (208)	1.974 (10$\underline{1}$3)
Reported d-spacings (Å) $BaFe_2O_4$ (PDF#25-1191)		3.160 (402)	2.736 (610)	2.590 (701)	2.110 (004)	2.051 (422)	
Reported d-spacings (Å) $BaFe_2O_4$ (PDF#26-0158)		3.260 (102)	2.730 (110)	2.613 (111)	2.092 (202)	2.033 (104)	

Table 2.2: Continued

Reported d-spacings (Å) $BaFe_2O_4$ (PDF#44-0897)		3.203 (102)		2.683 (110)		2.057 (202)	1.997 (104)
Reported d-spacings (Å) $Ba_2Fe_2O_5$ (PDF#39-1296)	3.670 (610)*	3.210 (231)	2.880 (720)	2.652 (531)*	2.187 (740)*	2.068 (802)	1.940 (160)*

* denotes low intensity peak. (nkl) denotes n, k, l in a 3D space. n, k, l are all integers. If it is above 9 (e.g. 11), the underline is used to identify the parameter. Underline denotes an integer above 9.

2.3.2 Pellet properties

Total porosity of the pellet was measured to be 11.06 % and its mean pore diameter was 10.25 nm. Measurements of the density of the BZF10 pellets yielded an average sintered density of 5.80 g/cm^3, which is greater than the theoretical density of $BaFeO_{3-x}$ (5.64 g/cm^3) while samller than that of $BaZrO_3$ (5.85 g/cm^3).

A typical TEM image of the cross-section area of the as-sintered pellet is shown in Figure 2.3a, with electron diffraction patterns presented in Figure 2.3b. The pellet had a polycrystalline structure with grain sizes in the range of 0.3–1 μm. Well-defined grain boundaries were observed, shown in Figure 2.3c. A high-magnification image of one specific grain is presented in Figure 2.3d, indicating minor cracks were located at the intergranular boundary regions. In the same high-magnification image, defects suggesting a brittle nature were also observed within the grain. A detailed analysis of the d-spacings is given in Table 2.3. The d-spacing data, measured from the diffraction pattern in Figure 2.3b and marked in Table 2.3, match well with those corresponding to the cubic barium zirconate phase and the primary phase of BZF10 identified by

synchrotron XRD technique. The lattice parameter of this phase is very close to that of the pure cubic $BaZrO_3$ phase. Multiple concentric Debye rings were observed in the diffraction pattern, confirming the polycrystalline structure of the sintered pellet. Additional diffraction spots were indicative of the presence of BaO, ZrO_2 and $BaFeO_{3-x}$ in minor quantities. As most of the d-spacings of these phases are quite similar to those of the barium zirconate phase, additional chemical mapping would be required to confirm their presence.

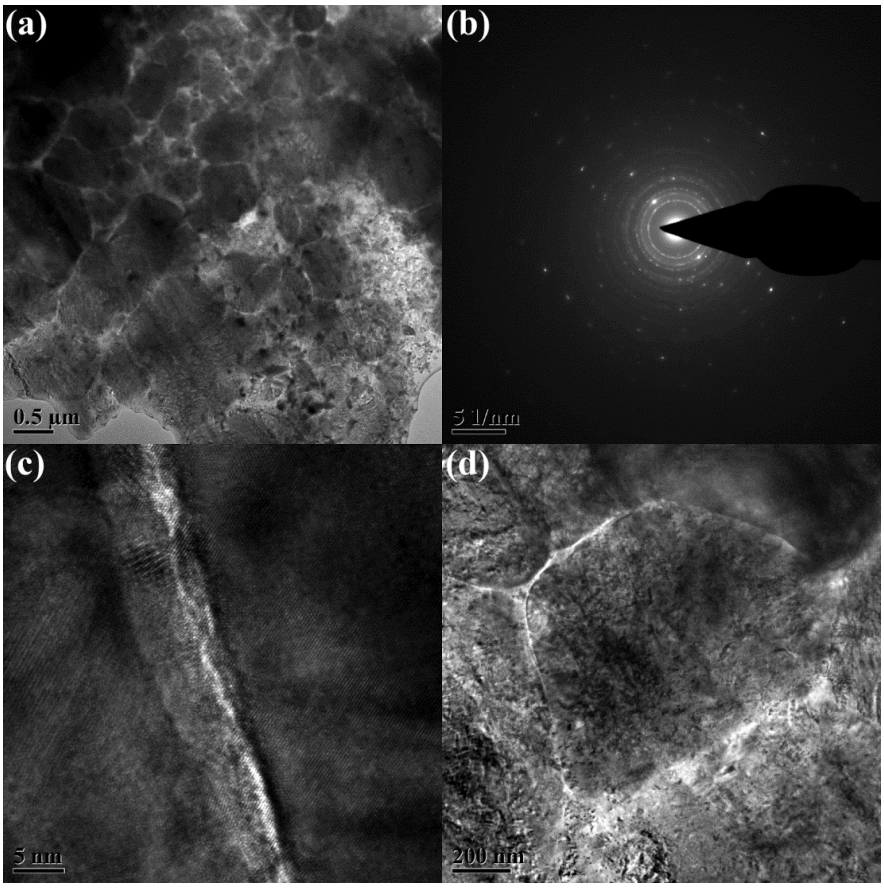

Figure 2.3: (a) TEM image of the as-sintered BZF10 pellet sample; (b) Diffraction pattern of the as-sintered BZF10 pellet sample; (c) High-resolution TEM image of the clear grain boundary; (d) High-resolution TEM image of a specific grain.

Table 2.3: Comparison and analysis of the calculated d-spacings from BZF10.

Calculated d-spacing (Å) (powder XRD)	Calculated d-spacing (Å) (as-sintered pellet DP)	Reported d-spacing (Å) ($BaZrO_3$) PDF#06-0399	Reported d-spacing (Å) ($BaFeO_3$) PDF#74-0646	Phase Identification
4.190 (100)	4.188	4.194 (100)	4.030 (104)	BZF10
3.712	3.727	--	3.700 (015)	$BaFeO_{3-\delta}$
2.964 (110)	2.955	2.965 (110)	2.845 (110)	BZF10
2.623	2.621	--	--	ZrO_2
2.095 (200)	2.096	2.097 (200)	2.098 (027)	BZF10
1.935	1.934	--	1.974 (10$\underline{13}$)	BaO
1.711 (211)	1.715	1.711 (211)	1.688 (217)	BZF10
1.482 (220)	1.480	1.482 (220)	1.422 (220)	BZF10
1.325 (310)	1.329	1.325 (310)	1.293 (137)	BZF10
1.120 (321)	1.125	1.120 (321)	1.128 (31$\underline{14}$)	BZF10
0.937 (420)	0.940	0.937 (420)	--	BZF10

(nkl) denotes n, k, l in a 3D space. n, k, l are all integers. If it is above 9 (e.g. 11), the underline is used to identify the parameter. Underline denotes an integer above 9.

The SEM image, STEM image and its corresponding analytical maps for Ba, Zr and Fe for a specific grain and the intergranular regions of the as-sintered pellet are shown in Figure 2.4. It is observed in the Ba map that Ba was uniformly present across the sample without any particular tendency for segregation. Zr appeared to favor towards

grains over intergranular areas. Fe segregated without favoring granular or intergranular regions. The ultra-thin region in the upper left corner (intergranular region) and the thick area in the right bottom (part of a neighbor grain) both happened to be Fe-rich segregated regions, which further confirms Fe is randomly distributed. It appears that, after the heat treatment of the raw powder, Ba is still present in the grains and grain boundaries in the formula of BaO, Zr mostly diffuses into the grains to form ZrO_2, and Fe randomly segregates in the form of FeO_x in particular parts covering both grain interior and boundary regions. Thus, STEM–XEDS analysis of the as-sintered material indicates a primary $BaZrO_3$ phase and a minor $BaO–FeO_x$ ($BaFeO_{3-x}$) phase, which agrees well with the results of synchrotron XRD pattern and electron diffraction pattern.

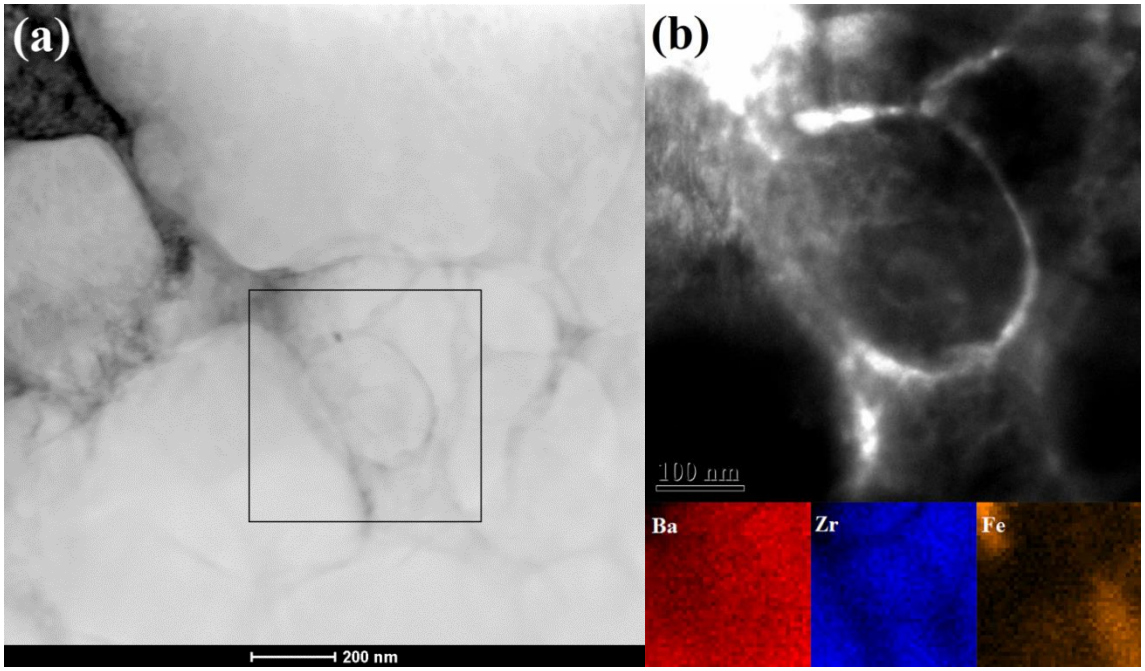

Figure 2.4: STEM-XEDS analysis of as-sintered BZF10 pellet sample; (a) SEM image of prepared sample; (b) STEM image of sample with inset elemental maps for Ba, Zr and Fe.

3. ELECTRICAL CONDUCTIVITY RELAXATION (ECR) AND OXYGEN PERMEATION OF IRON-DOPED BARIUM ZIRCONATE*

3.1 Introduction

This chapter primarily presents the electrical conductivity relaxation (ECR) measurement and oxygen permeation test on dense $BaZr_{0.9}Fe_{0.1}O_{3-\delta}$ (BZF10) disk. The ECR technique allows simultaneous probing of bulk conductivities and surface kinetics when the button cell is subjected to a step change in gas-phase reactant partial pressures while monitoring the transient response of electrical conductivity as the material equilibrates to the change in gas environments via surface electrochemical reactions. The transient electrical conductivity data is subsequently normalized and fitted to a one-dimensional, cartesian solution of Fick's 2nd law assuming surface electrochemical reaction of 1st-order dependence upon oxygen-ions. The variable parameters obtained by this fitting are the bulk ionic diffusion coefficient D_v (m^2/s) and the surface exchange coefficient k' (m/s). Oxygen permeation flux through BZF 10 membrane is measured and compared to literature reported values from similar perovskite materials. A BZF10 membrane shows comparable oxygen permeability, indicating BZF10 may be a promising material for multiple membrane applications. The material was observed to be electrochemically and mechanically stable over both electrochemical and permeation

* Part of this chapter is reprinted with permission from "Materials Synthesizing, Electrochemical Characterization and O_2 Permeation Properties of Fe-Doped Barium Zirconates" by H. Zhang et al. / Solid State Ionics 266 (2014) 58–67, http://dx.doi.org/10.1016/j.ssi.2014.08.011; and "Electrochemical, Catalytic and O_2-Permeation Studies of Iron-Doped Barium Zirconates for Membrane Reactor Applications" by ECS Transactions, 61 (1) 307-318 (2014), 10.1149/06101.0307ecst.

tests, which is especially significant for its implementation in high-temperature energy applications.

3.2 Experimental

3.2.1 Electrochemical analysis

Dense, as-sintered 13mm BZF10 button cells were prepared for ECR (electrical conductivity relaxation) analysis by applying a porous Pt electrode on one face of the cell and a dense Pt blocking electrode on the other. First, a conductive, adhesive Pt paste (Heraeus, A4338A) was screen-printed on one face of the pellet, then dried in stagnant air at room temperature for 1 hour followed by annealing at 950^{o}C in stagnant air for 1 hour with heating and cooling rates of 3^{o}C/min forming a porous electrode. For the blocking electrode, a 13mm diameter cylindrical Pt disk (Surepure Chemicals) was attached to the opposite side of the pellet using Pt paste, followed by annealing at 950^{o}C in stagnant air for 1 hour with heating and cooling rates of 3^{o}C/min.

Electrochemical analysis was performed using a single-chamber compression-sealed cell (Figure 3.1), which provided a cross-flow of the desired gas atmosphere across porous electrode face. Both electrodes were connected through Pt wires (Alfa Aesar, 43288) via coaxial cables to a frequency response analyzer (Solarton, SI 1260) and potentiostat (Solarton, SI 1287) for electrochemical measurement, controlled by PC equipped with Corrware and Zplot software for ECR and EIS analysis, respectively. A gas-mixing panel equipped with digital mass-flow controllers (Alicat) allowed precise blending of feed stream from UHP (99.999%) Ar (Praxair) and an O_2 containing

mixture gas (20%O_2, 5%He, balanced with Ar, Praxair) to achieve the desired oxygen partial pressure within the electrochemical cell. The whole assembly was inserted into an electric tube-furnace (Carbolite, MTF 10/25/130) for precise temperature control.

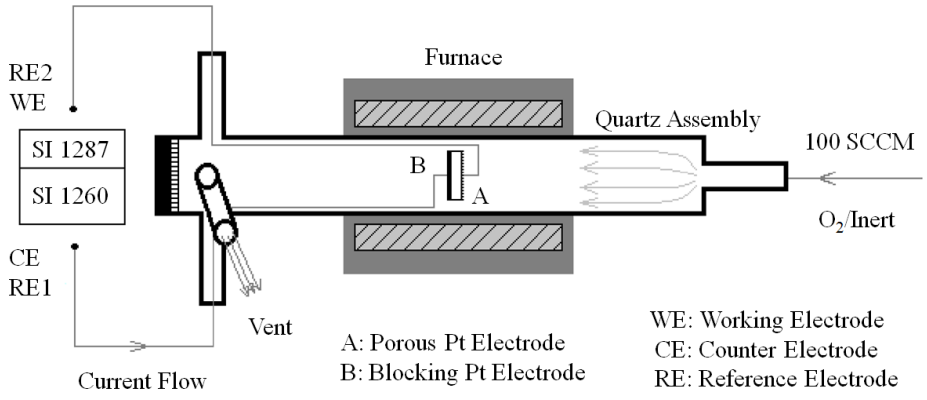

Figure 3.1: Schematic of single-chamber electrochemical cell.

ECR analysis is performed using a dense disk substrate of 13mm diameter and 0.73mm thickness, placed within the assembly such that the porous electrode face is exposed directly to gas environment. Electrical conductivity is calculated from the voltage across the porous and blocking electrodes, which is continuously monitored using a two-point galvanostatic measurement at 10 mA excitation current. The transient response in electrical conductivity ($\sigma_{ECR}(t)$) to a step change in oxygen partial pressure was recorded at 600-800^{o}C in dry 2.5 - 20 mol% O_2/Ar.

3.2.2 Oxygen permeation

Oxygen-permeation experiments were performed in a vertical high temperature 2-volume permeation/reaction cell shown schematically in Figure 3.2. The polished

dense membrane with thickness 1.15 mm was sealed onto a supporting ceramic tube by filling the gap between the membrane and the supporting tube with a sealing mixture. The sealing material was a well-ground wet mixture of glass powder (VIOX # 10584), BZF10 powder, and sodium aluminate (Riedel-de Haën # 13404) with a mass ratio 5:4:1. The mixture was manually ground with appropriate amount of deionized water to form a sticky paste. After the seal was dried in air at room temperature for 2 hours, the supporting tube with attached membrane in the permeation set up was heated up to 900^{o}C in air. After 30 minutes at 900^{o}C, Air was introduced to the volume between the outer quartz tube and the inner ceramic tube (feed side) and pure Ar was introduced to the volume inside the inner ceramic tube (sweep side) continually. The nitrogen contents in the sweep side were analyzed by a Gas Chromatography (Agilent 3000 Micro GC). Once the nitrogen signal detected in the sweep was minimized, the system was cooled to 600^{o}C and immediately employed for oxygen permeation measurement.

Dry compressed air (Praxair) was used for the feed stream and UHP (99.999%) Ar (Praxair) was used in the sweep stream for all oxygen permeation measurements. The gas flow rates on both sides were maintained at 100 mL/min and set and monitored by ALICAT gas flow controllers. The effective membrane surface area was ~1.60 cm^{2}. Permeate gas composition after reaching of equilibrium was monitored by GC. Measurements were taken at 600^{o}C and subsequently at 50^{o}C intervals up to 900^{o}C. An oxygen mass balance was used to calculate the oxygen permeation rate from measured sweep effluent composition, accounting for small yet finite gas crossover due to

imperfections in sealing, using nitrogen as a leak indicator (Equation 3.1) following a methodology previously reported by Kniep et al. [32]

$$J_{O_2} = (\%O_2 - \frac{21}{79} \cdot \%N_2) \cdot \frac{q}{A} \tag{3.1}$$

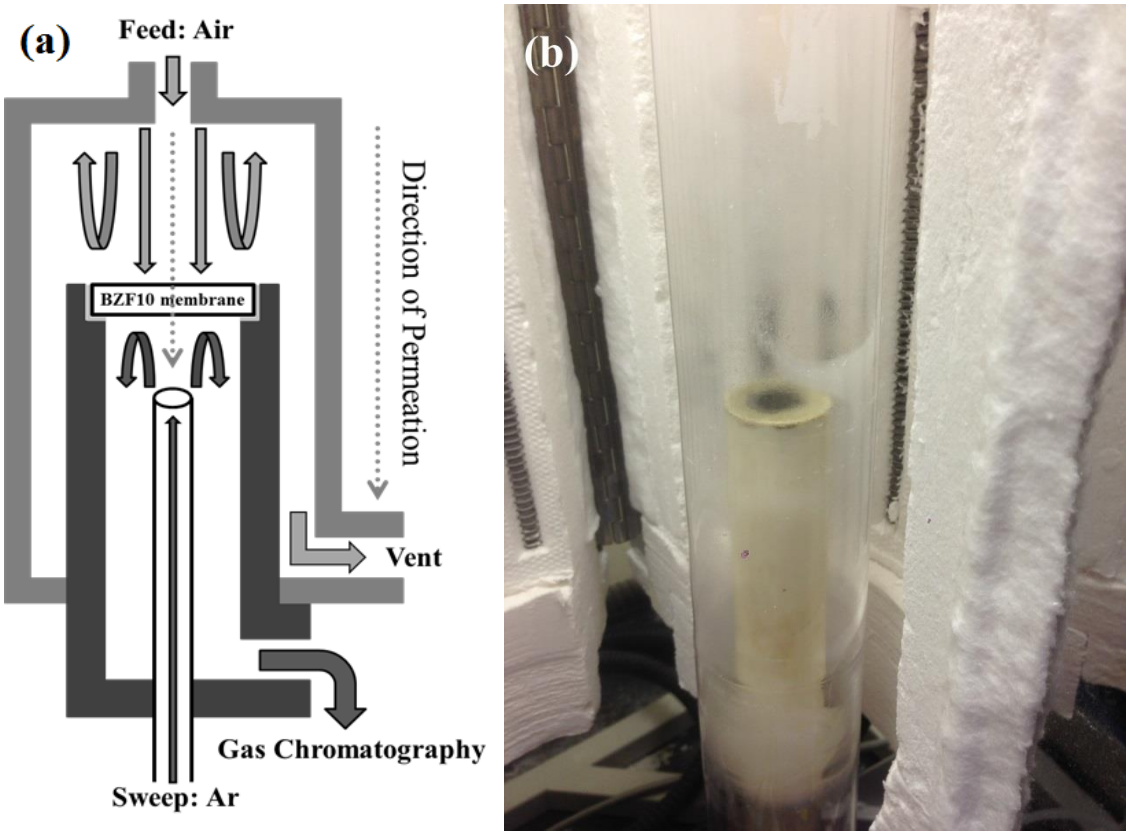

Figure 3.2: Experimental apparatus for measuring oxygen permeation; (a) schematic of two-chamber gas permeation cell; (b) actual permeation cell, with sealed membrane disk visible. [reprinted with permission from Ref. 182]

3.3 ECR theory

The present work employed a dense pellet geometry of sufficient aspect ratio ($d_p >> t_p$) that charge-carrier transport between either face of the pellet may be described by the following 1-D form of Fick's second law:

$$D_V \frac{\partial^2 C_V(x,t)}{\partial x^2} = \frac{\partial C_V(x,t)}{\partial t} \tag{3.2}$$

where C_V denotes the local concentration of oxygen vacancies within the ceramic, D_V denotes the diffusivity of oxygen vacancies, which is assumed both isotropic and independent of local concentration, x denotes the axial position within the ceramic disk of thickness t_p ($0 \le x \le t_p$), and t denotes time. A zero-flux inner boundary condition is employed to describe the blocking electrode, while a Robin-type outer boundary condition is employed to equate flux of vacancies at the porous electrode surface to the rate of the oxygen-surface electrochemical reaction, assuming an elementary rate expression in terms of solid-phase charge carrier concentrations. Lastly, the initial vacancy concentration is assumed to be uniform.

$$C_V(x,0) = C_{V,0} \tag{3.3}$$

$$D_V \left.\frac{\partial C_V}{\partial x}\right|_{x=0} = 0 \tag{3.4}$$

$$-D_V \left.\frac{\partial C_V}{\partial x}\right|_{x=t_p} = k'\left(C_V - C_{V,eq}\right) \tag{3.5}$$

In the above model, k' represents a gas-phase lumped kinetic parameter, which directly reflects the surface catalytic activity of oxygen vacancies for accepting oxygen

from chemisorbed gas-phase species (O_2). Solution of Equations (3.3-3.5) yields an infinite series-solution describing oxygen vacancy concentration in terms of t_p, k':

$$\frac{C_V(x,t)-C_V(0)}{C_V(\infty)-C_V(0)}=1-\sum_{n=1}^{\infty}\left[\frac{4\sin(\lambda_n)\cos(\lambda_n x/t_p)}{2\lambda_n+\sin(2\lambda_n)}\exp(-\frac{\lambda_n^2 D_V}{t_p^2}t)\right] \tag{3.6}$$

where $C_V(x,t)$ and $C_V(\infty)$ are, respectively, the instantaneous and equilibrated molar concentrations of oxygen vacancies at the outer surface ($x=t_p$), and $\{\lambda_n\}$ are the positive roots of the transcendental equation:

$$\lambda_n \tan(\lambda_n)=\frac{k'}{D_V}t_p \tag{3.7}$$

Equation 3.6 can be cast in terms of local electrical conductivity assuming that total electrical conductivity varies linearly with concentration. The normalized overall conductivity of the sample is then obtained by integrating Equation 3.6 over the entire sample thickness:

$$\hat{\sigma}=\frac{\sigma(t)-\sigma(0)}{\sigma(\infty)-\sigma(0)}=1-\sum_{n=1}^{\infty}\left[\frac{4\sin^2(\lambda_n)}{2\lambda_n^2+\lambda_n\sin(2\lambda_n)}\exp(-\frac{\lambda_n^2 D_V}{t_p^2}t)\right] \tag{3.8}$$

where $\sigma(0)$ and $\sigma(\infty)$ are, respectively, the initial and final equilibrated conductivities of the pellet. This solution represents a Cartesian analog to the established cylindrical-coordinate solution reported in the literature. [183-185] Transient electrical conductivity data were normalized and fitted to Equation 3.8 to obtain values for the bulk ionic diffusion coefficient D_V (m^2/s) and the surface exchange coefficient k' (m/s).

3.4 Results and discussions

3.4.1 ECR

Figure 3.3 shows typical electrical conductivity relaxation transients together with the respective fitting curve for BZF10, following a pO_2 change from 0 to 0.025 atm at 700°C. Similar results were acquired for each temperature and oxygen step-change, showing good agreement with the proposed vacancy transport model. The chemical diffusion coefficient D_V and surface kinetic parameter k' obtained from the fitted data were plotted as a function of pO_2 on log-log scale to assess order-dependence upon oxygen pressure, assuming single power-law relationship (Equations 3.9, 3.10).

$$D_V = D_{V0} \cdot pO_2^m \tag{3.9}$$

$$k' = k'_0 \cdot pO_2^n \tag{3.10}$$

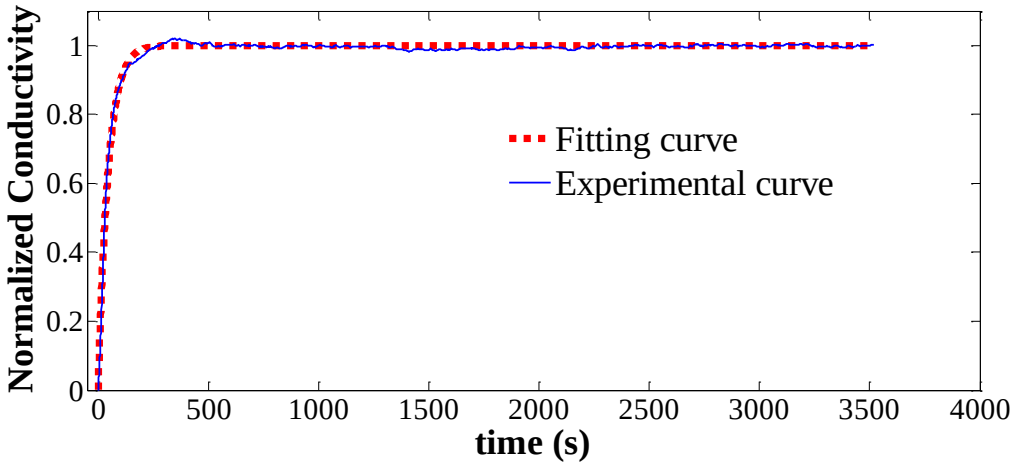

Figure 3.3: Normalized conductivity relaxation plot for BZF10 at 700°C for oxidation step change in pO_2 with a final pO_2 of 0.025 atm.

Fitted values of D_V and k' for BZF10 are presented in Figure 3.4 as a function of pO_2, and values of m and n are shown in Table 3.1. Arrhenius plots for D_V and k' at constant pO_2 are presented in Figure 3.5, with resulting activation energies obtained for D_V and k' summarized in Table 3.2. The general trend observed is that both D_V and k' increase with pO_2. Within the pO_2 range used in this study, both parameters vary approximately according to power law of pO_2.

As shown in Figure 3.4, calculated oxygen vacancy diffusion coefficients D_V are in the range 10^{-8}-10^{-7} m^2/s from 600-800^{o}C, which is comparable in magnitude to values reported for a similar Ba-containing perovskite material ($BaTiO_{3-\delta}$), [186] and one order of magnitude greater than other ceramic conductors ($SrFeO_{3-\delta}$ [187], $La_{0.6}Sr_{0.4}Cr_{0.2}Fe_{0.8}O_{3-\delta}$ [188]). D_V depends on oxygen nonstoichiometry (δ) and at constant pO_2, the nonstoichiometry increases with increasing $\left[Fe'_{Zr}\right]$, thus, the relatively high D_V calculated for BZF10 suggests a significant concentration of B-site acceptor dopant $\left[Fe'_{Zr}\right]$. D_V is proportional to pO_2^m, with m = ~0.34 for all temperatures studied (Table 3.1). A similar power-law dependence with m = ~0.33 in the same pO_2 region was observed in the results of ECR analysis on $BaTiO_{3-\delta}$ [186] and m= ~0.37 on $La_{0.6}Sr_{0.4}Co_{0.2}Fe_{0.8}O_{3-\delta}$ [188]. At constant pO_2, a higher temperature gives a higher D_V due to an increase in defect migration between lattice sites and a higher oxygen vacancy concentration. As m remains constant over the temperature range studied herein, activation energies may be obtained from Arrhenius curves of D_V at values of 0.20-0.26 eV and E_a increases with decreasing pO_2 as shown in Figure 3.5 and Table 3.2. A

possible explanation for increasing E_a with decreasing pO_2 is: 1) oxygen vacancies are distributed in the lattice sites with a high concentration, ordering, and enhanced interaction at low pO_2; 2) the migration energy $\Delta H_{D_V}^m$ and formation energy $\Delta H_{D_V}^f$ of oxygen vacancies via Reaction 1.4 associated to E_a for D_V increase with decreasing pO_2; 3) large values of $\Delta H_{D_V}^m$ and $\Delta H_{D_V}^f$ contribute to a large activation energy for D_V. The high D_V with small activation energy of BZF10 is in good agreement with that from $LaCrO_3$ doped with 5 mol% Mg determined by ECR techniques and thermal gravimetry analysis by Yu *et al.* [189] They explained that their high D_V (1.15-2.3×10^{-7} m^2/s) and the related small activation energy (0.20 eV) were governed by grain boundary diffusion with no significant lattice diffusion observed. They further suggested that the insignificant lattice diffusion was due to the accumulation of oxygen vacancies at the grain boundaries and a relative small grain size (1 μm). Therefore, it can be concluded that the primary mechanism of diffusion coefficients D_V in BZF10 is grain boundary diffusion.

Values of the surface kinetic parameter (k') are in the range 1.0-8.5×10^{-5} m/s from 600-800°C (Figure 3.4), which is similar in magnitude to the results reported for $SrFeO_{3-\delta}$, $La_{0.5}Sr_{0.5}FeO_{3-\delta}$, and $La_{0.2}Sr_{0.8}Cr_{0.2}Fe_{0.8}O_{3-\delta}$. [187] Experimental data indicate that k' is proportional to pO_2^n, with $0.67 \leq n \leq 0.79$, as summarized in Table 3.1. Reaction 1.4 indicates k' depends on pO_2^n since the oxygen vacancy concentration has a negative dependence on pO_2. If Reaction 1.4 were the rate determining step, the overall pO_2^n dependence with $n < 0.5$ would be expected, corresponding to rate determining

step involving a single oxygen atom. [187] In contrast, a value of $n > 0.5$ observed in this study suggests a different mechanism with molecular oxygen involved in the rate determining step of the surface reaction, as reported elsewhere for $La_{0.2}Sr_{0.8}Cr_{0.2}Fe_{0.8}O_{3-\delta}$ and $La_{0.6}Sr_{0.4}Co_{1-y}Fe_yO_{3-\delta}$ materials. [187, 190] The activation energy of *k'* is found to decrease with increasing pO_2 as presented in Figure 3.5 and Table 3.2, while values of ~16 – 28kJ/mol are consistent with absorption being rate-limiting. Thus, the observed decrease in activation energy with increasing pO_2 may be explained by an increase in the oxidation state of Fe cations which facilitates the chemisorption of oxygen [191].

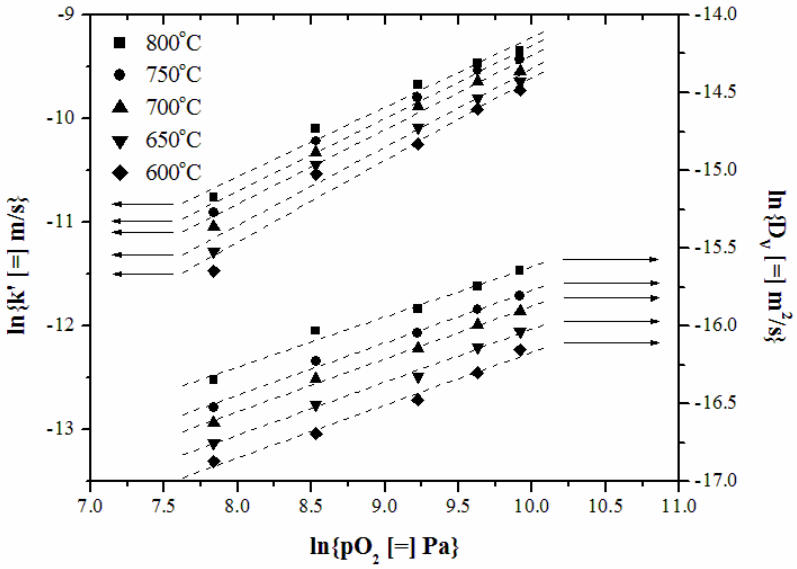

Figure 3.4: Log-log plots of D_V (m^2/s) and *k'* (m/s) versus pO_2 (Pa).

Table 3.1: Values of *m* and *n* for D_V and *k'* dependence upon pO_2 for BZF10 at various temperatures.

Temperature (^oC)	800	750	700	650	600
m (order with D_V)	0.32	0.34	0.34	0.34	0.34
n (order with *k'*)	0.67	0.70	0.72	0.76	0.79

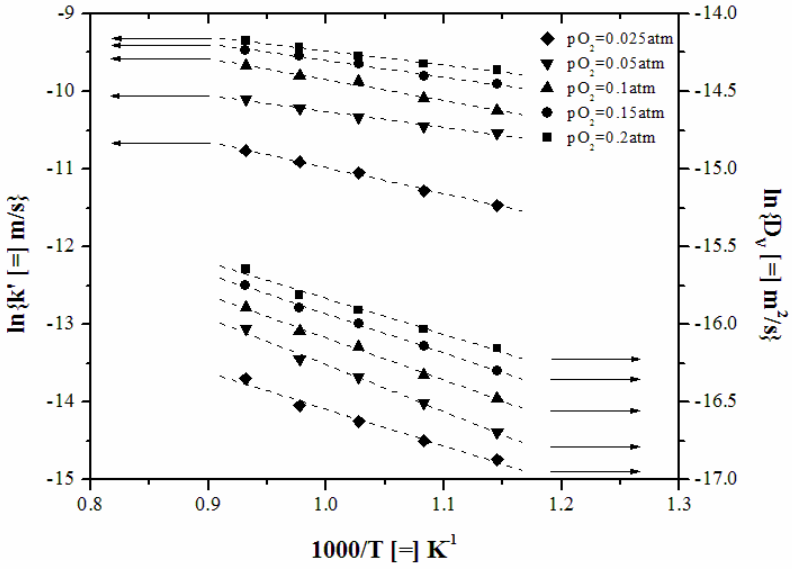

Figure 3.5: Semi-log plots of D_V (m^2/s) and *k'* (m/s) versus $1000/T$ (K^{-1}).

Table 3.2: Activation energies for D_V and *k'* from temperature dependence at various pO_2.

pO_2 (atm)	0.025	0.05	0.10	0.15	0.20
E_a of D_V (eV)	0.20	0.26	0.23	0.22	0.20
E_a of *k'* (eV)	0.29	0.18	0.23	0.19	0.16

Table 3.2 shows that both D_V and k' exhibit comparable activation energies, implying a strong correlation between these two parameters. This is further confirmed by the observation that both parameters increase with increasing pO_2. Figure 3.6 shows the correlation between D_V and k' for BZF10 and the slope from the ln(k')-ln(D_V) plot is almost constant with little temperature dependence.

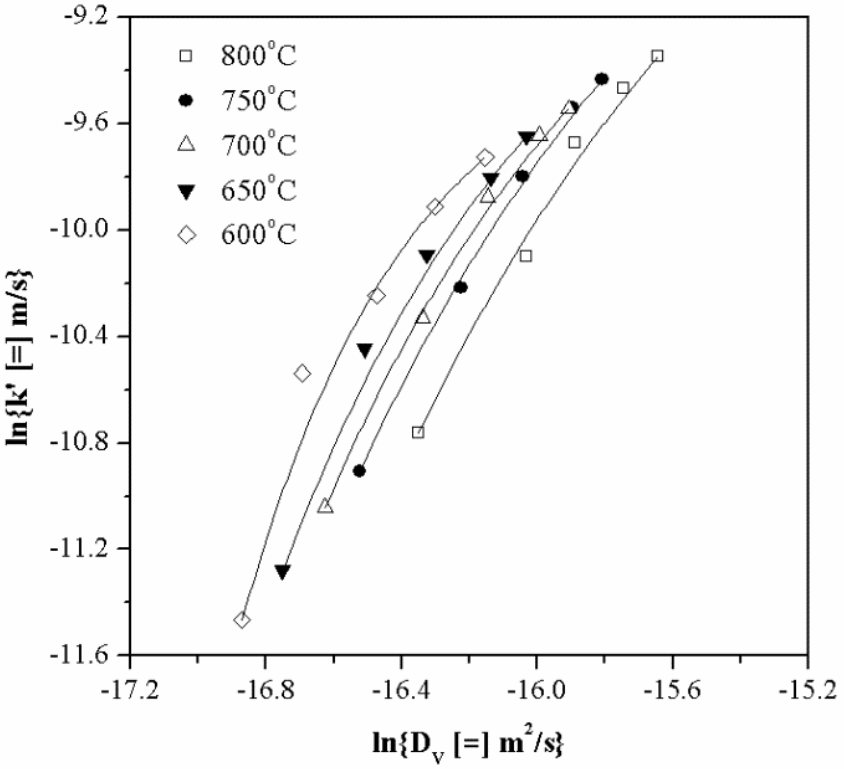

Figure 3.6: Double logarithmic plot of the correlation between D_V and k' for BZF10.

3.4.2 Oxygen permeation

Figure 3.7a shows the effects of temperature on oxygen flux/permeability through the BZF10 membrane and the related Arrhenius plots are shown in Figure 3.7b.

The oxygen permeability was determined by the oxygen permeation flux (J_{O_2}), thickness of the membrane (L), and the oxygen partial pressure difference (Equation 3.11). The highest oxygen flux was measured to be 0.102 mL/(min·cm^2) at 900^{o}C and the resulting oxygen permeability is 4.11×10^{-11} mol/(m·Pa·s). The oxygen flux increased slowly with temperature, indicating a thermally activated process with low activation energy (21.1 kJ/mol); this suggests the oxygen permeation is limited by the oxygen exchange between the gas phase and the membrane surface [192]. The constant activation energy suggests that no phase transition or change in the transport mechanism occurred between 600-900^{o}C. As summarized in Table 3.3, a BZF10 membrane has a relative high oxygen permeability and small activation energy in comparison to the results from other researchers with similar materials. The combination of low activation energy and high materials stability indicates BZF10 may be a promising material for multiple electrochemical membrane applications (e.g., methane partial oxidation, hydrogen production via water splitting, ethanol reforming).

$$Permeability\big|_{O2} = J_{O_2} \cdot \frac{L}{pO_2^{feed} - pO_2^{sweep}} \tag{3.11}$$

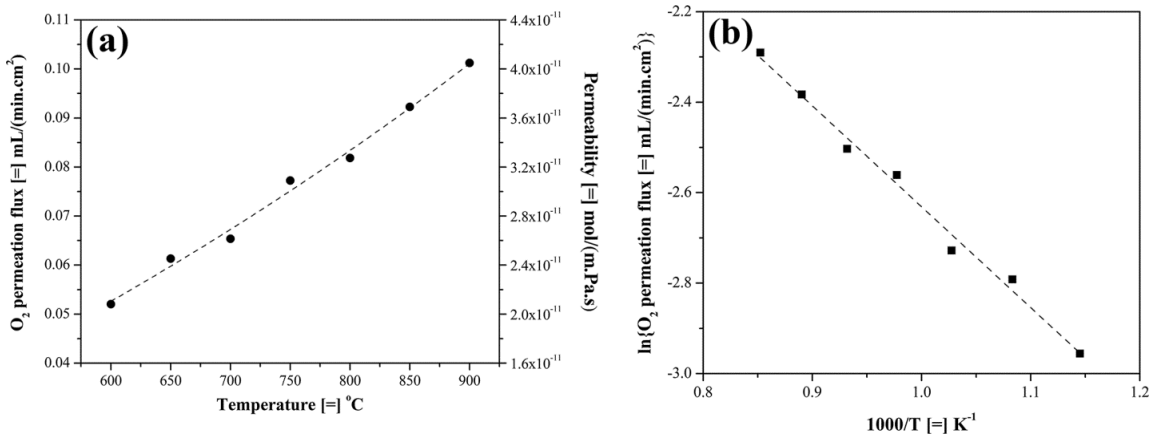

Figure 3.7: (a) Oxygen permeation flux and oxygen permeability of BZF10 membrane; (b) resulting Arrhenius plots of the oxygen permeation flux.

Table 3.3: Comparison of oxygen permeation flux between BZF10 and similar materials in various atmospheres.

Composition	E_a	J_{O_2} at 900°C	T range	Permeability at 900°C	Reference
	(kJ/mol)	(mL/min·cm^2)	(°C)	(mol/m·Pa·s)	
$Ba_{0.9}Zr_{0.9}Fe_{0.1}O_{3-\delta}$	21.1	0.102	600-900	4.11×10^{-11}	This work
$Ba_{0.5}Sr_{0.5}Zn_{0.2}Fe_{0.8}O_{3-\delta}$	~14	0.33 (925°C)	925-975	1.49×10^{-10} (925°C)	[192]
$SrCo_{0.5}FeO_x$	48	0.006	700-900	2.52×10^{-12}	[32]
$SrCoFeO_x$	65	0.018	700-900	7.55×10^{-12}	[32]
$Sm_{0.4}Ba_{0.6}Co_{0.2}Fe_{0.8}O_{3-\delta}$	127	0.110	750-900	3.08×10^{-11}	[193]

4. ELECTROCHEMICAL AND CATALYTIC CHARACTERIZATION OF IRON-DOPED BARIUM ZIRCONATE*

4.1 Introduction

This chapter reports the investigation of 10%Fe-doped $BaZrO_3$ (BZF10) over a full cycle of oxidizing and reducing (dry O_2, dry CO_2, humidified inert Ar, CO and H_2, then back to dry O_2) environments expected for both solid oxide electrolysis cell (SOEC) and solid oxide reversible fuel cell (SORFC) applications.

The in-situ electrochemical probing techniques discussed in Chapter 3 will be integrated with ex-situ effluent gas compositional analysis of gas exiting the chamber of the electrochemical cell, in order to provide information regarding overall catalytic reaction rates and reaction pathway selectivity. The effluent gas analysis via mass spectrometer will be employed in tandem with single-chamber ECR/EIS techniques under a wide range of gas environments to relate the observed electrochemical surface behavior to overall reaction rates of CO oxidation, CO_2 reduction and H_2 production. Results indicate that BZF10 exhibits catalytic activity towards CO_2 reduction to CO and O_2 under an intermediate surface carbonate ions formation and decomposition mechanism when exposed to dry CO_2/inert conditions and promotes water-gas-shift

* Part of this chapter is reprinted with permission from "Materials Synthesizing, Electrochemical Characterization and O_2 Permeation Properties of Fe-Doped Barium Zirconates" by H. Zhang et al. / Solid State Ionics 266 (2014) 58–67, http://dx.doi.org/10.1016/j.ssi.2014.08.011; and "Electrical Conduction and Reaction Analysis on Mixed Conducting Iron-Doped Barium Zirconates" by H. Zhang, B.A. Wilhite / Solid State Ionics 286 (2016) 7–18, http://dx.doi.org/10.1016/j.ssi.2015.11.023; and "Electrochemical, Catalytic and O_2-Permeation Studies of Iron-Doped Barium Zirconates for Membrane Reactor Applications" by ECS Transactions, 61 (1) 307-318 (2014), 10.1149/06101.0307ecst.

reaction under CO/H_2O/inert environments. Exposure to humidified H_2 results in increase in conductivity with pH_2, indicating n-type semi-conduction under this gas environment.

4.2 Experimental

4.2.1 Electrochemical characterization coupled with reaction study

Fe-doped $BaZrO_3$ perovskites powders were synthesized via solid-state reaction using precursor nitrate powders to target a final composition of $BaZr_{0.9}Fe_{0.1}O_{3-\delta}$ (BZF10), and subsequently fabricated into 13mm diameter dense pellets. Analysis of the as-synthesized powders confirmed a final perovskite composition of $Ba_{0.9}Zr_{0.9}Fe_{0.1}O_{3-\delta}$. A detailed report of the powder synthesis technique, pellet fabrication process, material characterization using synchrotron XRD, TEM, STEM-XEDS, etc. and electrochemical analysis under dry O_2/Ar atmosphere at 600-800^oC of BZF10 can be found in Chapter 2. The 13 mm diameter, 0.72 mm thick cylindrical button cell was prepared with a porous Pt electrode annealed on one face and a dense Pt blocking electrode adhered on the other prior to placement within a quartz-ceramic tube-in-tube single-chamber assembly (Figure 4.1), and continuously investigated via combined electrochemical and catalytic experiments over the sequence of oxidizing and reducing environments detailed below. The single-chamber apparatus provides continuous gas flow over the cell surface while enabling electrical connections to porous and blocking electrodes. Both electrodes were connected via coaxial cables to a frequency response analyzer (Solartron, SI 1260) and potentiostat (Solartron, SI 1287) operated by CorrWare and Zplot software to perform

electrical conductivity relaxation (ECR) and electrochemical impedance spectroscopy (EIS) analysis, respectively. A gas mixing panel equipped with digital mass flow meters (Alicat Scientific Inc.) allowed precise blending of feed gases to achieve target partial pressures within the chamber. A temperature-controlled bubbler filled with de-ionized water was used to introduce steam at variable steam partial pressure for analysis under humidified inert (Ar) and reducing (CO or H_2) gases. Effluent gases passed through a liquid trap filled with dry ice to remove moisture prior to gas analysis via quadropole mass spectrometer (QMS) (RGA 100, Stanford Research Systems). The QMS was calibrated using a "five-point" external standard technique for each gas species of interest (O_2, CO_2, CO, CH_4, H_2 and Ar) prior to experiments and recalibrated upon completion of all gas exposures.

The single-chamber assembly was inserted into a programmed tube-furnace (Carbolite, MTF 10/25/130) and heated to 800^{o}C at a rate of 3^{o}C/min under 100 cm^3/min dry Ar flow. Dry O_2/Ar was first introduced into the electrochemical cell at 800^{o}C and subsequently at 50^{o}C intervals down to 600^{o}C. After the electrochemical characterization under dry O_2/Ar, a 24-hours dry Ar washing (100 cm^3/min) at 600^{o}C was employed to blow away all the O_2 remaining in the system and bring the cell back to the fresh as-sintered state to initialize the subsequent CO_2 gas exposure analysis. At this point, the combined electrochemical and catalytic investigations of the BZF10 material were performed as follows. Upon equilibration of the electrochemical cell with Ar, the assembly was heated to 800^{o}C at a rate of 3^{o}C/min. Once at temperature, the material was exposed to a sequence of step-changes in CO_2 partial pressure (pCO_2 = 0.01, 0.025,

0.05, 0.075, 0.10 atm) in dry gas conditions and the CO_2 stream was diluted in Ar maintaining a total flowrate of 100 mL/cm^3. After each step-change in gas composition, the transient response in electrical conductivity was measured using a two-point technique with an excitation current of 10 mA and recorded with time until equilibration of the material with the new gas environment was reached. Once the measured electrical conductivity stabilized, a sequence of five impedance spectra was obtained over the frequency range of 1 MHz down to 0.1 Hz (amplitude ~10 mV). Based upon an assumed equivalent circuit (discussed in Section 4.3), the resulting Nyquist plots allow determination of bulk material resistance from the left-most x-intercept and provide insight into grain boundary resistance through the middle semi-circle and surface kinetics based upon the right-most tail/semi-circle. After the dry CO_2/Ar exposure, the same dry Ar washing procedure was employed to blow away all the carbon containing gases in the material and also recalled when finishing other gases (H_2O, CO, H_2) exposure test. Following the same procedure, the electrochemical cell was exposed to a sequence of step-changes in steam partial pressure (pH_2O = 0.021, 0.042, 0.073, 0.12, 0.20 atm), CO partial pressure in humidified condition through steam bubbler (pCO = 0.01, 0.025, 0.05, 0.075, 0.10 atm) and H_2 partial pressure in humidified condition through steam bubbler (pH_2 = 0.025, 0.05, 0.10, 0.15, 0.20 atm). For humidified gases tests, the steam bubbler temperature was set at room temperature (19^{o}C) followed by 30, 40, 50, 60^{o}C for H_2O exposure tests under inert (Ar) atmosphere and remained fixed at room temperature (19^{o}C) for all subsequent CO, H_2 exposures.

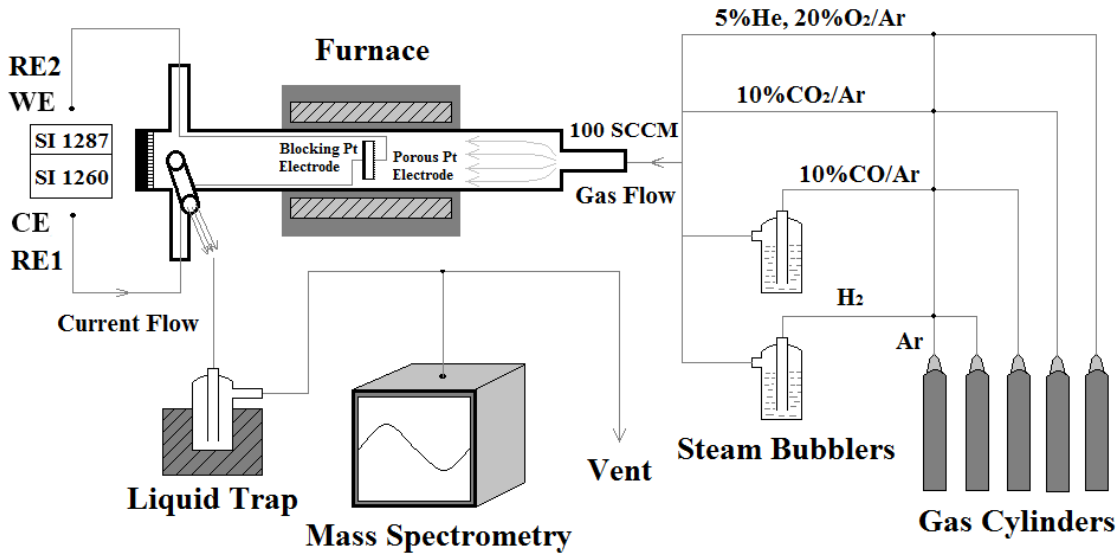

Figure 4.1: Schematic of the single-chamber apparatus for combined electrochemical and catalytic analysis. [reprinted with permission from Ref.182]

4.3 Analysis of electrochemical impedance spectra

Total electrical conductivities (σ_{EIS} [=] mS/cm) were calculated using the first *x*-axis intercept of the resulting Nyquist spectra (R_∞ in Figure 4.2), which should be in good agreement with equilibrated conductivities obtained from ECR experiments ($\sigma_{ECR}(\infty)$). Based on an ideal equivalent circuit model (Figure 4.2), the resulting impedance spectra were fitted to a corresponding impedance model to determine the bulk and grain boundary resistance values using the least squares fitting procedure of Zview software. Logarithms of the conductivities were plotted versus oxygen partial pressure to allow the determination of the conduction mechanism. Semi-log plots of σT (S·K/cm) versus 1000/T (K^{-1}) were plotted to determine the apparent activation energies for conduction (E_a) as per Equation 4.1, where R is the gas constant (8.314 J/mol·K).

$$\sigma \cdot T = A \cdot \exp(-E_a / RT) \tag{4.1}$$

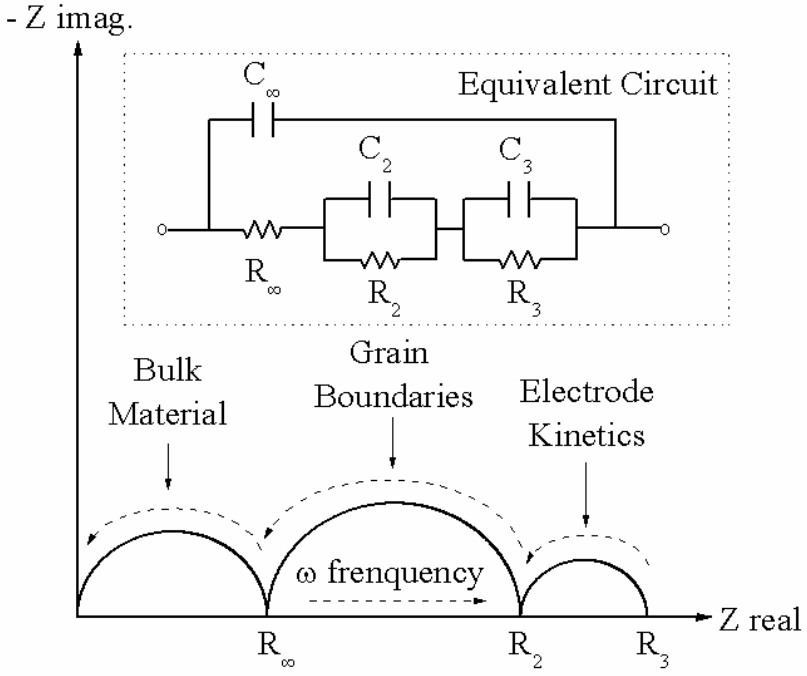

Figure 4.2: Ideal impedance spectra employed for analyzing EIS data and its corresponding equivalent circuit model.

4.4 Results and discussions

4.4.1 Dry O_2

Figure 4.3a shows Nyquist plots obtained from EIS techniques at 800^{o}C, and indicates negligible grain resistances. Figure 4.3b shows the pO_2 dependence of σ_{EIS} (total electrical conductivity measure by EIS) at 600-800^{o}C. EIS results indicated the stability was particularly excellent under dry oxidizing condition (high pO_2). Under dry oxidizing atmospheres, the total conductivity increases with pO_2, showing the expected primarily p-type behavior with an order close to 1/4 at all temperatures. Conduction in this material under dry oxygen may be viewed as comprising of two steps in series: 1) reaction between oxygen and oxygen-ion vacancies at the gas-solid interface to generate

electron-holes, via Reaction 4.2; 2) transport of electron-holes across the thickness of the pellet by hopping between Fe^{n+} sites. Thus, conduction would be limited by step 1 alone at 600-800°C. Above 600°C, conductivity increased with increasing pO_2 by an order predicted by thermodynamics, which is consistent with a controlling resistance involving the gas phase. Semi-log plots of $\sigma_{EIS}T$ versus 1000/T are presented in Figure 4.3c. The activation energy of BZF10 in dry oxyen is in the range of 0.16-0.18 eV at 600-800°C.

$$\frac{1}{2}O_2(g) + V_O^{\bullet\bullet} \leftrightarrow O_O^X + 2h^{\bullet} \tag{4.2}$$

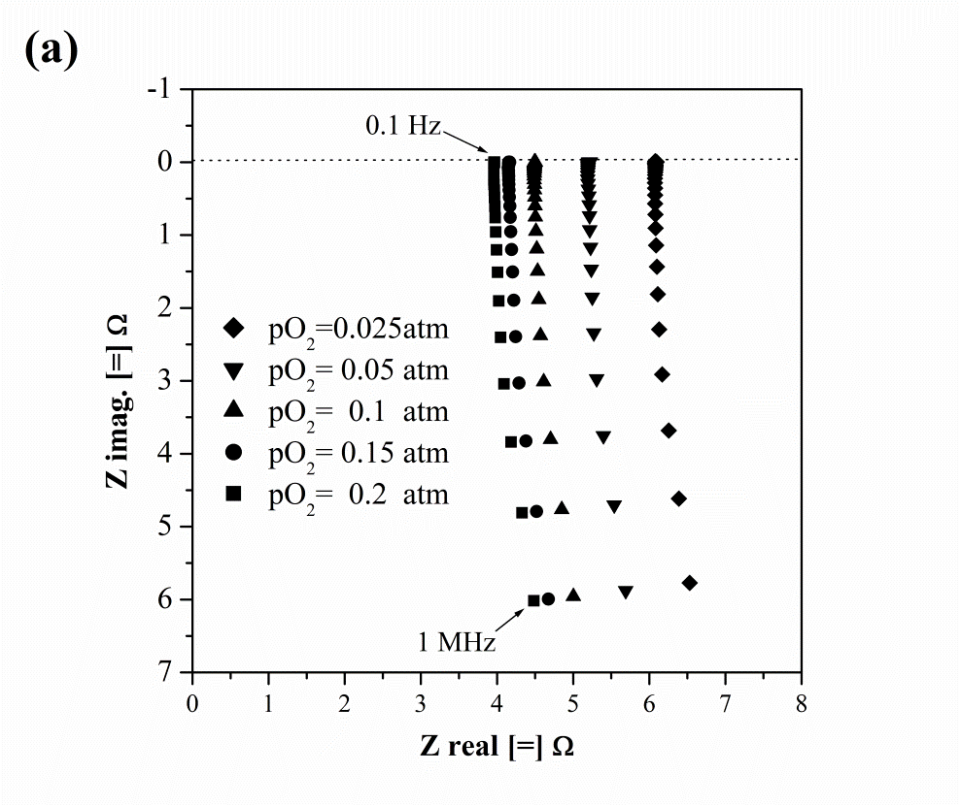

Figure 4.3: (a) Nyquist plot for oxygen exposure at 800°C; (b) Log-log plots of σ_{EIS} (mS/cm) versus pO_2 (Pa) for oxygen exposure; (c) Semi-log plots of $\sigma_{EIS}T$ (mS·K/cm) versus 1000/T (K^{-1}) for oxygen exposure.

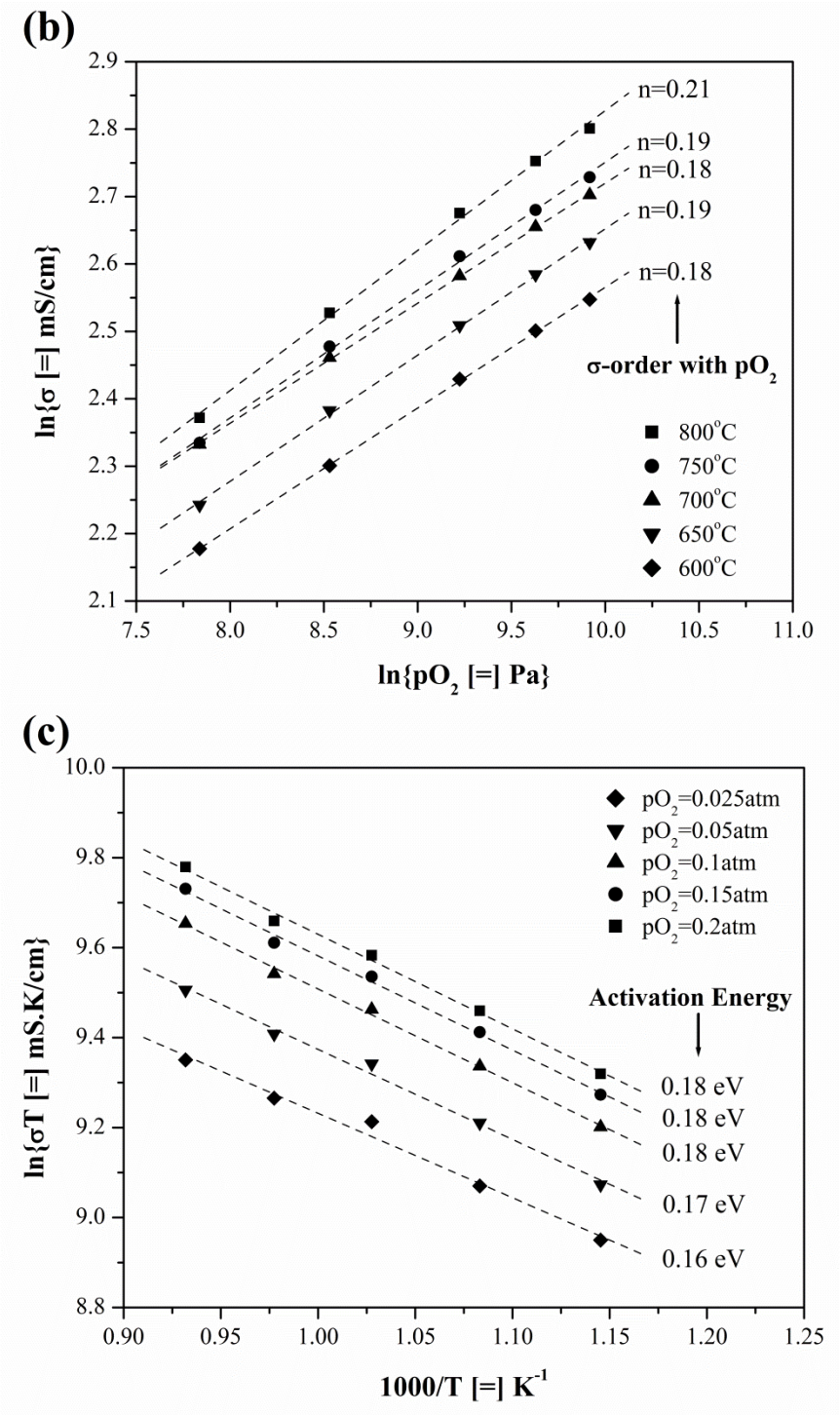

Figure 4.3: Continued

4.4.2 Dry CO_2

Figure 4.4a-b present the EIS results in the form of Nyquist plots obtained under dry CO_2/Ar environment at 800^{o}C and 600^{o}C, respectively. At 800^{o}C, the Nyquist plots started with a high-frequency tail, which was located in the positive imaginary resistance zone and attributed to inductance, continued with a mid-frequency arc indicating grain boundary conduction and ended with a low-frequency tail suggesting the presence of surface reactions that influence bulk electrical conductivity. EIS data obtained at 800^{o}C indicate increasing grain resistances at higher CO_2 partial pressure (pCO_2) and the presence of surface reaction at all CO_2 partial pressures. EIS data obtained at 600^{o}C likewise consist of a high-frequency arc located fully within the negative imaginary resistance zone, which was attributed to grain boundary transport and a low-frequency tail indicating the presence of surface reaction mechanism as that at 800^{o}C. In contrast to the trend observed at 800^{o}C, Nyquist plots at 600^{o}C indicate higher grain boundary resistances at low pCO_2, suggesting a different semi-conduction mechanism from that at 800^{o}C.

Figure 4.4c presents the total electrical conductivity as a function of pCO_2 on a log-log plot. Consistent with the p-type semi-conduction mechanism described in Section 4.4.1 under dry O_2 environment, an increase in electrical conductivity resulting from CO_2 introduction via similar reaction of oxidizing gas with oxygen vacancies would be expected (Reaction 4.3), where subscript “s” and “g” denote surface and gaseous species, respectively, and the describing all other species using Kröger-Vink notation [177].

$$CO_{2(g)} + V_O^{\bullet\bullet} \leftrightarrow CO_{(g)} + O_O^X + 2h^{\bullet} \quad (4.3)$$

However, at 650-800^{o}C, the electrical conductivity is found to decrease with increasing pCO_2 when introducing dry CO_2/Ar to the electrochemical cell, which indicates that Reaction 4.3 fails to describe the electrochemical reaction at high pCO_2. An alternative mechanism (Reaction 4.4) explains this electrochemical behavior by assuming that CO_2 first reacts with surface lattice oxygen (O_O^X) to generate surface carbonate ion ($CO_{3\ (s)}^{2-}$) and oxygen vacancies ($V_O^{\bullet\bullet}$), followed by the subsequent decomposition of $CO_{3\ (s)}^{2-}$ to produce CO and O_2 (Reaction 4.5).

$$CO_{2(g)} + O_O^X \leftrightarrow CO_{3\ (s)}^{2-} + V_O^{\bullet\bullet} \quad (4.4)$$

$$CO_{3\ (s)}^{2-} + 2h^{\bullet} \leftrightarrow CO_{(g)} + O_{2(g)} \quad (4.5)$$

The assumption of an intermediate carbonate ion formation at the BZF10 surface is supported by multiple literature reports of ion formation on both Fe-based oxide catalyst [105-106] and mixed conducting ceramic membrane surfaces [194-195]. The overall reaction (Reaction 4.6, as a combination of Reaction 4.4-4.5) thus consists of molecular CO_2 being incorporated by surface lattice oxygen and two electron holes to release molecular CO and O_2 while leaving behind a mobile oxygen vacancy, which describes the observed decrease in electrical conductivity with increasing pCO_2. Additional mathematical proof is presented in Appendix A.

$$CO_{2(g)} + O_O^X + 2h^{\bullet} \leftrightarrow V_O^{\bullet\bullet} + CO_{(g)} + O_{2(g)} \quad (4.6)$$

Figure 4.4d presents the total electrical conductivity as a function of temperature on a semi-log plot. The related activation energy is calculated to be 0.44-0.70 eV, which decreases with increasing pCO_2 becoming significantly larger than that associated with the dry O_2/Ar exposure (0.16-0.18 eV). These higher activation energies support the above argument of a different semi-conduction mechanism from that under dry O_2 exposure. Additionally, the electrical conductivity of the BZF10 material reduced from 16.4 $mS \cdot cm^{-1}$ to 1.6 $mS \cdot cm^{-1}$ after exposure to CO_2, suggesting an initial net reduction of BZF10 material via Reaction 4.3, before Reactions 4.6 come to dominate the electrochemical response. The expected oxygen vacancy sites are 2.93×10^{-4} mol within the material, and the steady-state CO production confirmed by QMS measurement of CO levels in effluent gas (Figure 4.4e) can be up to 1.25×10^{-3} mol (each experiment duration is 1 hour), thus a steady-state catalytic reaction rather than a transient respond is confirmed. The presence of steady-state surface reaction first-order kinetics with respect to pCO_2 at both high and low CO_2 partial pressures with maximum reaction rate of 3.06×10^{-3} $mol \cdot s^{-1} \cdot m^{-2}$ at 0.1 atm pCO_2 and 800^{o}C.

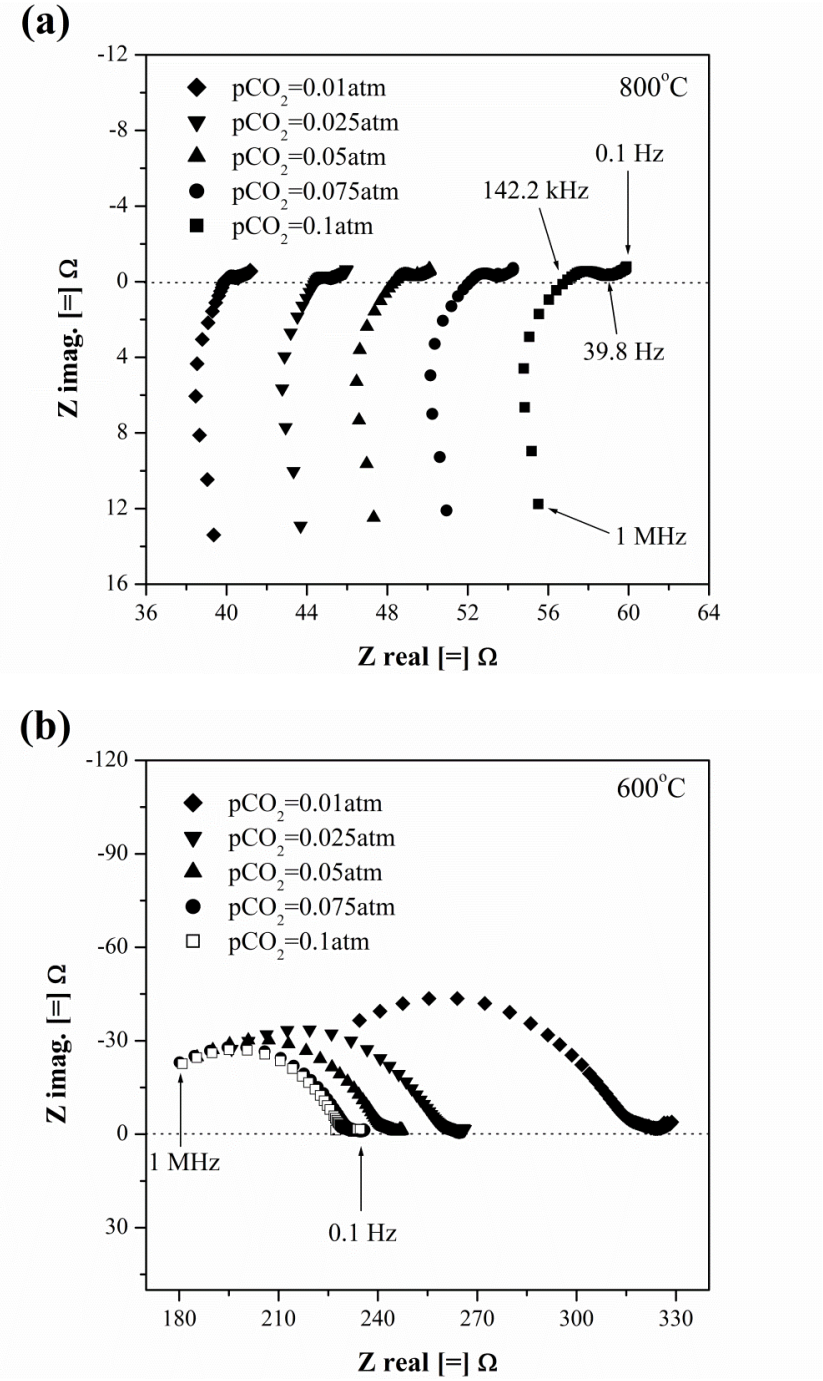

Figure 4.4: (a) EIS spectra obtained upon equilibration of BZF10 with dry CO_2/Ar exposure at 800°C; (b) EIS spectra obtained upon equilibration of BZF10 with dry CO_2/Ar exposure at 600°C; (c) Log-log plots of electrical conductivity versus CO_2 partial pressures (pCO_2) at 600-800°C; (d) Semi-log plots of σT versus 1000/T under CO_2 exposure; (e) Log-log plots of reaction rate versus pCO_2 at 600-800°C.

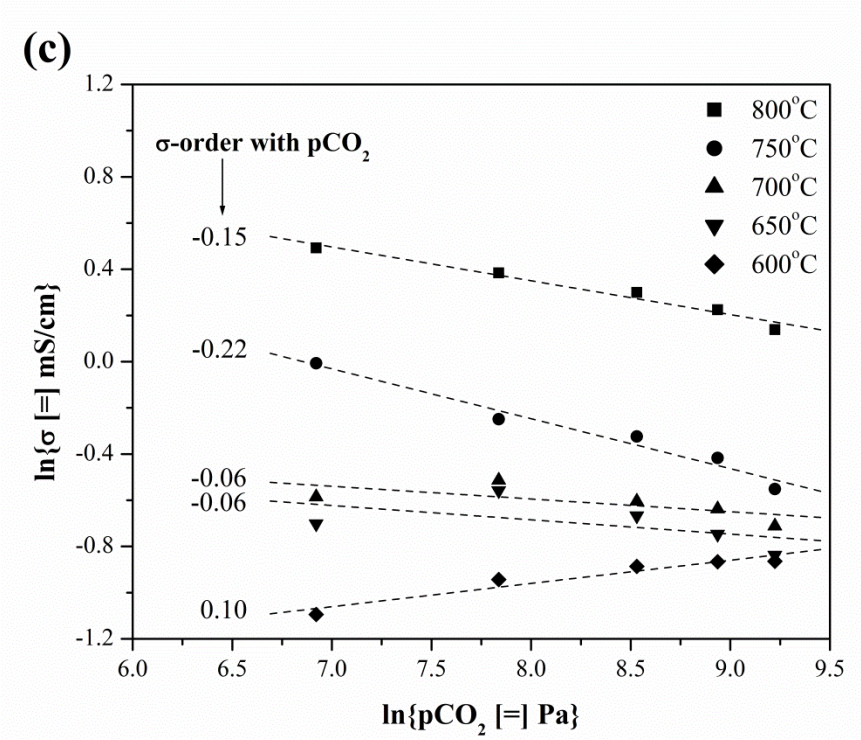

Figure 4.4: Continued

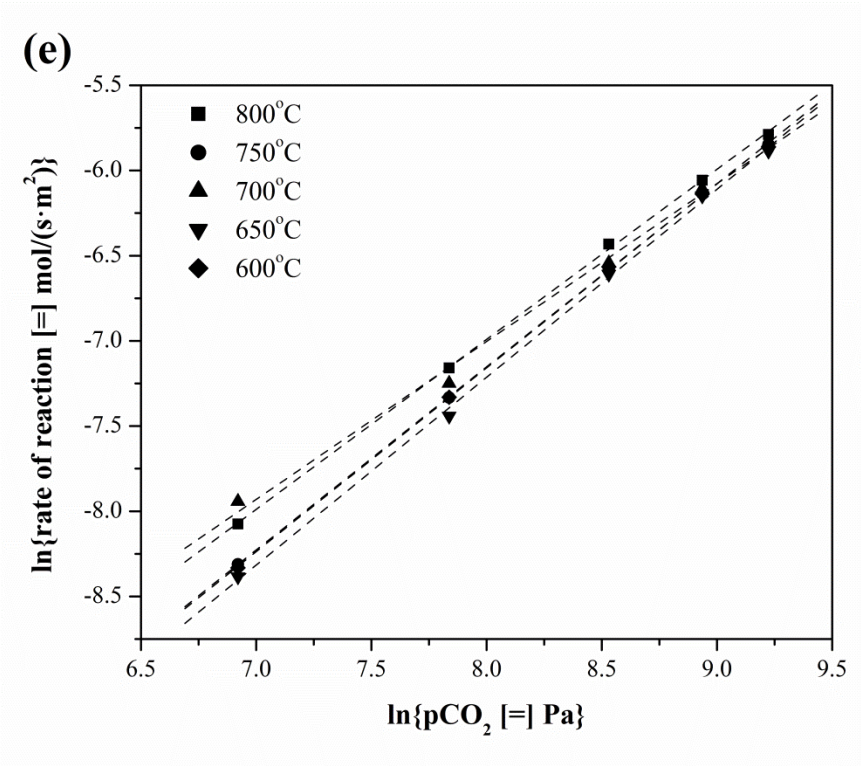

Figure 4.4: Continued

4.4.3 H_2O

Figure 4.5a presents the Nyquist plots obtained under H_2O/Ar environment at 800°C and 600°C. At both temperatures, the Nyquist plots started with a high-frequency inductive tail, continued with a small semi-circle indicating finite grain boundary resistance and a short low-frequency tail suggesting negligible surface reaction. EIS data indicates the material is less active at a lower temperature, while the similar shape of Nyquist plots suggests an identical mechanism between 600-800°C.

Log-log plots of electrical conductivity versus H_2O partial pressure (pH_2O) presented in Figure 4.5b indicate a slight decrease in total conductivity ($\Delta\sigma < 0.7\%$) with

increasing pH_2O, corresponding to an order dependency of -0.02 at 800°C and ~0 at 600-750°C. The zero slope suggests only slight decrease in mobile charge carrier concentrations occurring within the cell. The related activation energy is calculated to be 0.23 eV (Figure 4.5c), which is found to be invariant with steam partial pressure. Negligible conversion of steam to oxygen and hydrogen or reactions with any possible remainder carbonaceous species from previous dry CO_2 exposure was verified by the QMS results, which showed <500 ppm H_2, O_2, CO, CO_2 and CH_4 contents existing in the dry effluent.

The calculated oxygen vacancy diffusion coefficients D_V of BZF10 are in the range of 10^{-8} – 10^{-7} m^2/s from 600–800°C as shown in Section 3.4.1. It gives a diffusion time of 2.6 – 26 seconds across the thickness of the button cell, which is much smaller than the duration of experiment (1 hour), indicating the electrical conductivity change is not limited by bulk diffusion. Under exposing to H_2O/Ar, Fe ions were difficult to be largely reduced, otherwise a subsequent obvious change in electronic conductivity would be expected. Thus the slight decrease in electrical conductivity may be explained by protonic charge carrier uptake via electrochemical reaction of an H_2O molecule splitting a proton combining with a surface lattice oxygen atom and a hydroxyl ion occupying an oxygen vacancy site to generate two hydroxyl ions ($OH_O^{\bullet}$) via Reaction 4.7,

$$H_2O + V_O^{\bullet\bullet} + O_O^X \leftrightarrow 2OH_O^{\bullet} \tag{4.7}$$

assuming that the resulting hydroxyl ions are slightly less mobile than oxygen vacancies at 600-800°C. Reaction 4.7, a commonly verified mechanism for acceptor-doped perovskites [156, 196-197], suggests the presence of proton conduction; however the

observed ~0 slope at 600-800°C implies either minimal surface electrochemical reaction, or the increase of proton conductivity by water incorporation and the increase of electronic conductivity by reduction of Fe ions compensating the decrease of conductivity caused by the consumption of mobile oxygen vacancies in the absence of reducing gas species i.e., $(\Delta\sigma_{OH_O^\bullet} \approx \Delta\sigma_{V_O^{\bullet\bullet}})$.

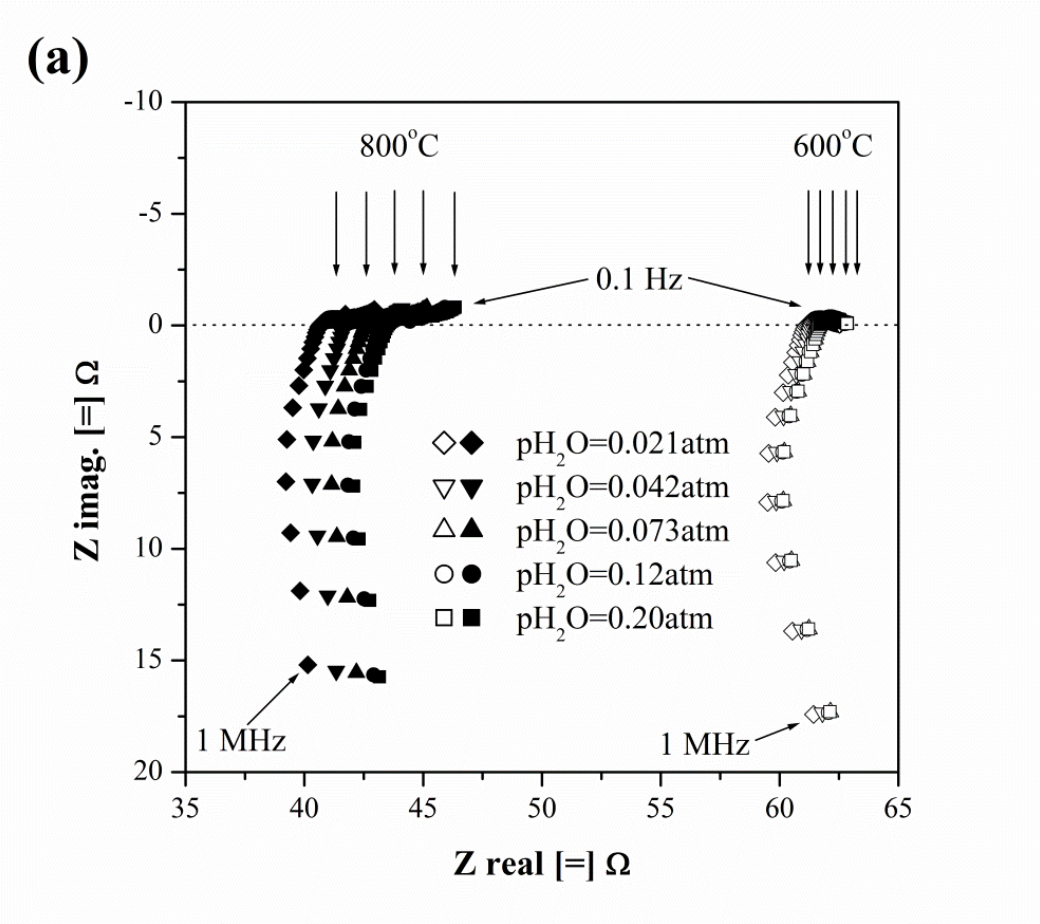

Figure 4.5: (a) EIS spectra obtained upon equilibration of BZF10 with H_2O/Ar exposure at 800°C and 600°C; (b) Log-log plots of electrical conductivity versus H_2O partial pressures (pH_2O) at 600-800°C; (c) Semi-log plots of σT versus 1000/T under H_2O exposure.

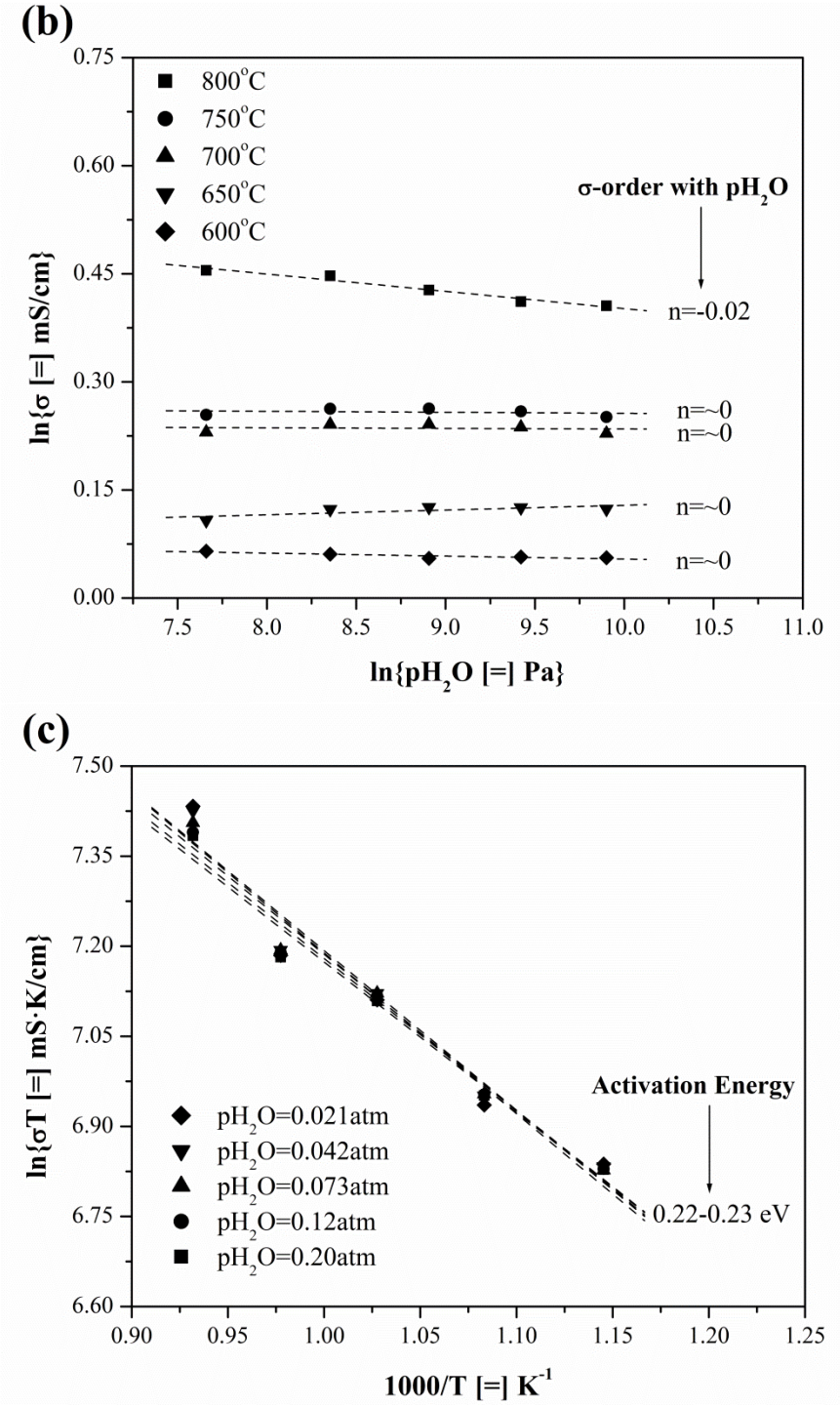

Figure 4.5: Continued

4.4.4 Humidified CO

Nyquist plots obtained in the presence of humidified CO/Ar reducing gas at 800^{o}C (Figure 4.6a) show two primary shapes under different CO partial pressure (*pCO*). When CO/H_2O was first introduced into the electrochemical cell (*pCO* → 0.01 atm), the resulting Nyquist plot started with a flattened semi-circle at high resistance followed by a short tail suggesting significant grain boundary resistance and mild surface reaction rates. With increasing *pCO*, the resistance was reduced while high-frequency inductive tail remained and grain boundary transport reduced significantly. At 600^{o}C, the inductive tail completely disappears from the Nyquist plots (Figure 4.6b). All plots display a high-frequency semi-circle and a low-frequency tail, both of which are consistent with the shape obtained at 0.01 atm *pCO* and 800^{o}C.

Log-log plots of electrical conductivity as a function of CO partial pressure present two distinct regions corresponding to low (≤ 0.05 atm) and high (≥ 0.05 atm) *pCO* at 600-800^{o}C. In the low *pCO* region, a positive dependence approaching ½-order was observed at 800^{o}C (Figure 4.6c) which decreased to 0.04 at 600^{o}C, suggesting that temperature is the rate limiting factor at 600^{o}C, not the reagent concentration. The related activation energies (Figure 4.6d) are 0.48-0.78 eV, which increase with *pCO*. Conductivity under humidified CO/Ar environment is lower than that under humidified inert. However, at high *pCO* the observed negative dependence varied from −1-order at 800^{o}C to −0.5-order at 600^{o}C (Figure 4.6c). The related activation energies (Figure 4.6d) are 0.69-0.78 eV, which are found to be lower at higher *pCO* in this region, suggesting a different dominant mechanism under these conditions. Effluent gas QMS analysis

indicated that steady-state rates of H_2 and CO_2 production (Figure 4.6e) increased with *pCO* following distinctly separate order dependencies.

Based upon the above observations, the following mechanism is proposed. The appearance of CO_2 may be explained via Reaction 4.8, in which a CO molecule combines with a lattice oxygen and two mobile electron holes to generate CO_2 and an oxygen vacancy site:

$$CO + O_O^X + 2h^\bullet \leftrightarrow CO_2 + V_O^{\bullet\bullet} \tag{4.8}$$

The appearance of H_2 may then be explained using a pair of established electrochemical reactions from the literature [198]. In the presence of humidified CO, Reaction 4.7 may be assumed to occur, generating hydroxyl ions from lattice oxygen and vacancies (consumed and/or generated via equilibration of Reaction 4.8). Secondly, literature has established that when introducing H_2 into proton conductors, protons may be reversibly expressed in a hydroxide form [198], thus the reverse of this reaction (Reaction 4.9) may be assumed to occur such that gaseous hydrogen may equilibrate with hydroxyl ions within the proton conductor. Therefore, by combining Reaction 4.7 and Reaction 4.9, one may expect gaseous H_2O molecules to react with oxygen vacancies to create hydrogen and electron holes (Reaction 4.10):

$$2OH_O^\bullet \leftrightarrow H_2 + 2O_O^X + 2h^\bullet \tag{4.9}$$

$$H_2O + V_O^{\bullet\bullet} \leftrightarrow H_2 + O_O^X + 2h^\bullet \tag{4.10}$$

The introduction of CO facilitates Reaction 4.10 by generating sufficient oxygen vacancies via Reaction 4.8. From the resulting mechanism (Reactions 4.7-4.9),

increasing electron hole concentration with *pCO* may be expected if $pCO < pH_2O$, as the presence of CO promotes H_2O electrolysis in turn contributing to a positive-order dependence of electrical conductivity upon *pCO*. Once *pCO* is increased sufficiently for the system to be considered saturated with oxygen vacancies, Reaction 4.8 may be expected to be dominate such that decreasing electron hole concentration with *pCO* would result in a negative-order dependence of electrical conductivity upon *pCO*. The above mechanism combines to yield the water-gas-shift overall reaction (Reaction 4.11) which is experimentally confirmed via co-generation of CO_2 and H_2 from humid CO environment.

$$CO + H_2O \leftrightarrow CO_2 + H_2 \tag{4.11}$$

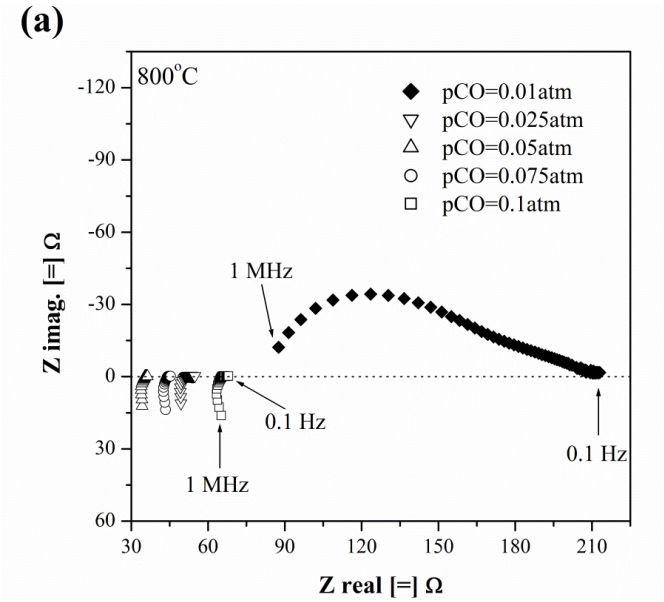

Figure 4.6: (a) EIS spectra obtained upon equilibration of BZF10 with $CO/H_2O/Ar$ exposure at 800°C; (b) EIS spectra obtained upon equilibration of BZF10 with $CO/H_2O/Ar$ exposure at 600°C; (c) Log-log plots of electrical conductivity versus CO partial pressures (*pCO*) at 600-800°C; (d) Semi-log plots of σT versus $1000/T$ under CO exposure; (e) Log-log plots of CO_2 and H_2 production rate versus *pCO* at 600-800°C; (f) H_2/CO_2 selectivity at 600-800°C.

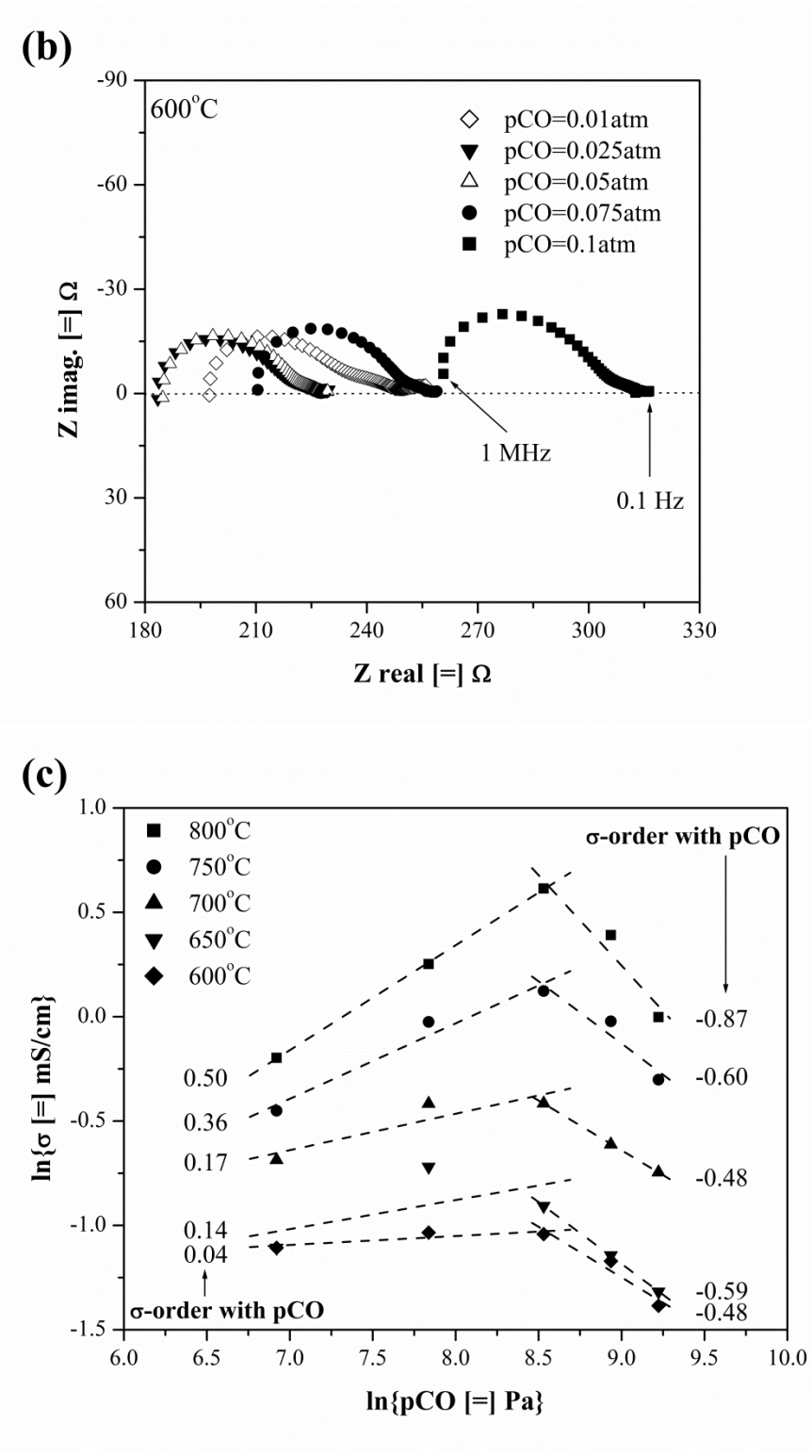

Figure 4.6: Continued

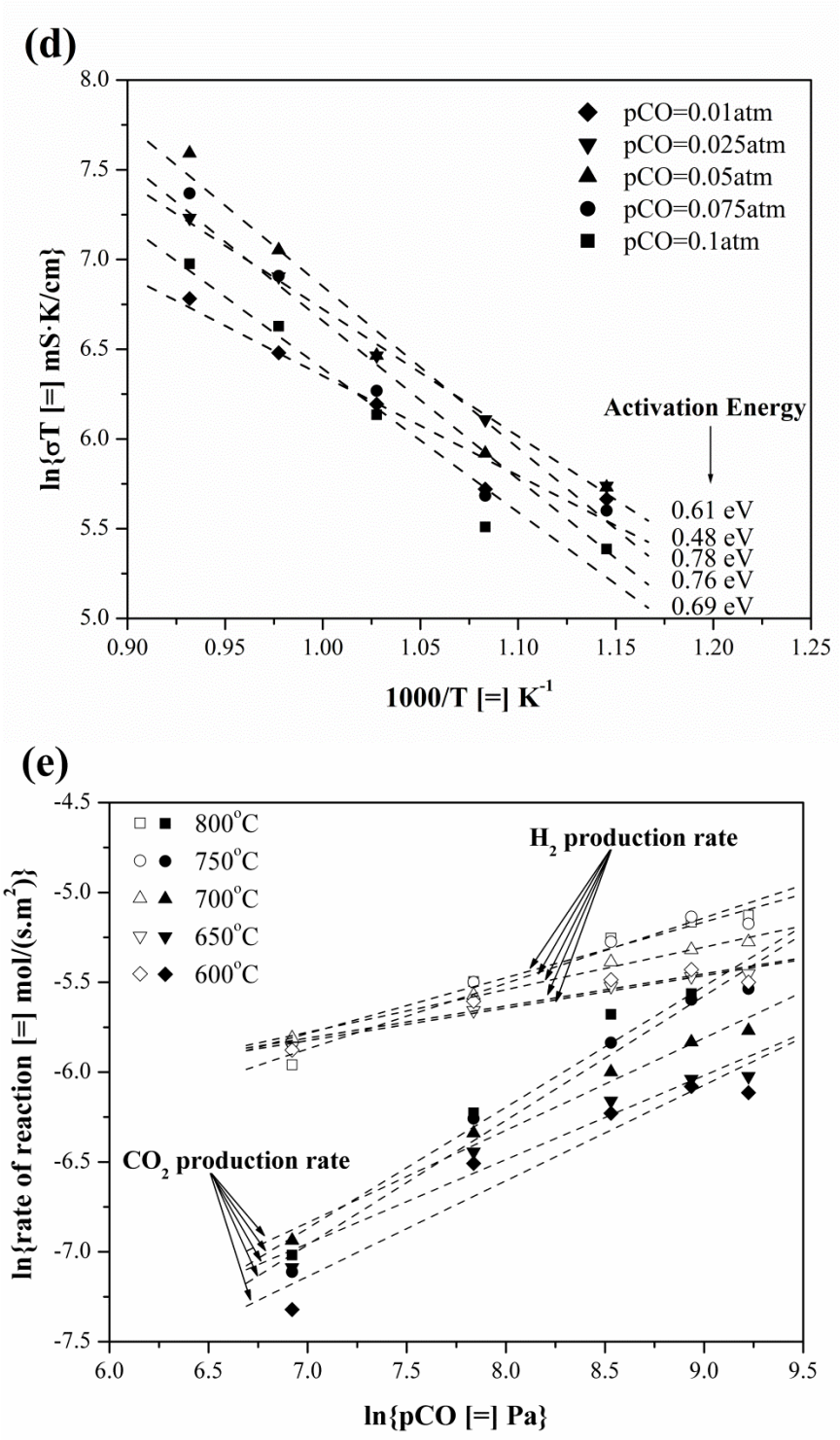

Figure 4.6: Continued

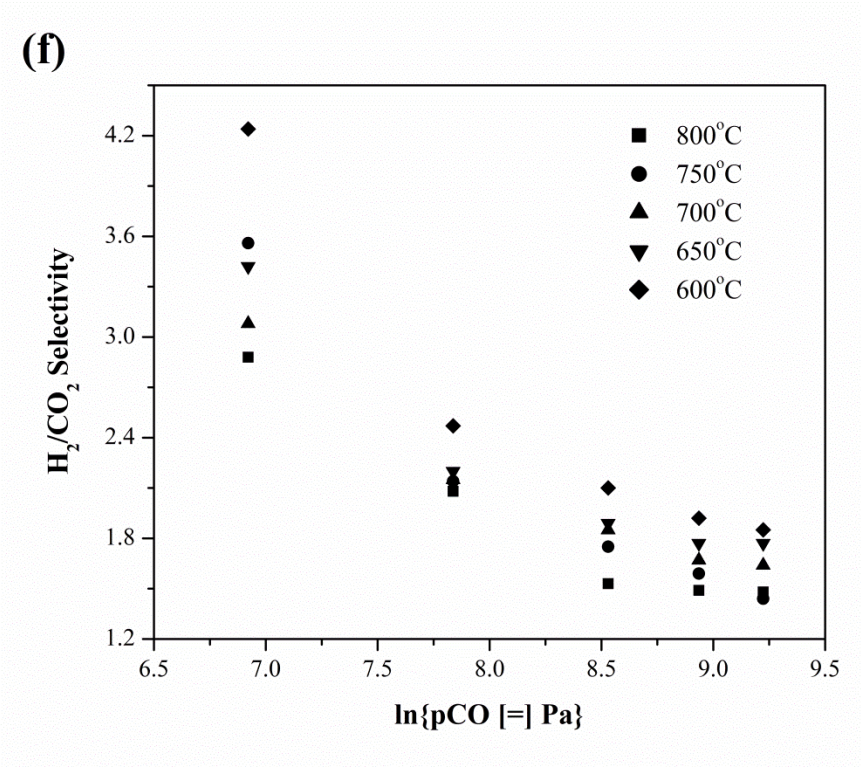

Figure 4.6: Continued

4.4.5 Humidified H_2

Impedance spectra obtained under humidified H_2/Ar environment at both 800°C (Figure 4.7a) and 600°C (Figure 4.7b) did not present the high-frequency inductance tail, which was observed for most of the previous gas environments. The high-frequency inductance tail was attributed to the long lead (0.5 mm diameter and 30 cm length) and clearly observed especially under either high temperatures or non-reducing environments. Additionally, the left-most semi-circle associated with grain-boundary transport was seen to be significantly larger than that observed under H_2O/Ar and humidified CO/Ar environments. Surface reaction was observed at both temperatures

due to the presence of low-frequency tail/arc. Electrical conductivity is found to increase mildly (Figure 4.7c) with H_2 partial pressure (pH_2) under constant H_2O partial pressure (pH_2O) with a power-law order 0.11-0.13 at 700-800^{o}C. At 600-650^{o}C, the transient conductivity responded very slowly to environment change (T, pH_2), especially when $pH_2 \leqslant 0.05$ atm, indicating temperature is the rate limiting factor. Activation energies are calculated to be 0.82-0.92 eV (Figure 4.7d), indicating a more reducing environment would contribute to a higher activation energy. The QMS measurement confirms initial consumption of hydrogen by the button cell upon introduction of moist H_2.

Most acceptor-doped perovskites are unsuitable as p-type semi-conductors under reducing conditions, owing to the rapid drop of p-type electronic conductivity with decreasing oxygen activity. [143] However, materials have been shown to exhibit n-type semi-conduction under reducing conditions despite the suppression of free electron concentration created by acceptor doping [143]. Thus, the observed electrochemical behavior of the Fe-doped perovskite under humidified H_2/Ar may be explained by two n-type semi-conduction mechanisms:

$$H_2 + 2O_O^X \leftrightarrow 2OH_O^\bullet + 2e' \tag{4.12}$$

$$H_2 + O_O^X \leftrightarrow H_2O + V_O^{\bullet\bullet} + 2e' \tag{4.13}$$

The former mechanism described by Reaction 4.12 shows the introduction of humidified hydrogen into the lattice of the material would generate hydroxyl ions $(OH_O^\bullet)$, which is formed by the combination of an interstitial proton associating strongly with an oxygen ion in its neighborhood. This mechanism would lead to protonic as well

as electronic conductivity, which has been observed in other acceptor-doped barium zirconates capable of hydrogen permeation [33]. Alternatively, increasing n-type conductivity with pH_2 may occur due to oxygen abstraction (Reaction 4.13), in which a hydrogen molecule combines with a lattice oxygen atom to form a water molecule and leave an oxygen vacancy site; however this mechanism is suspect as the reverse was not observed under variable H_2O exposure. Interestingly, the observed activation energy under humidified hydrogen (0.82-0.92 eV) is significantly greater than that observed under oxygen-acceptor behavior (E_a = 0.16-0.18 eV) in dry O_2 exposure (Section 4.4.1).

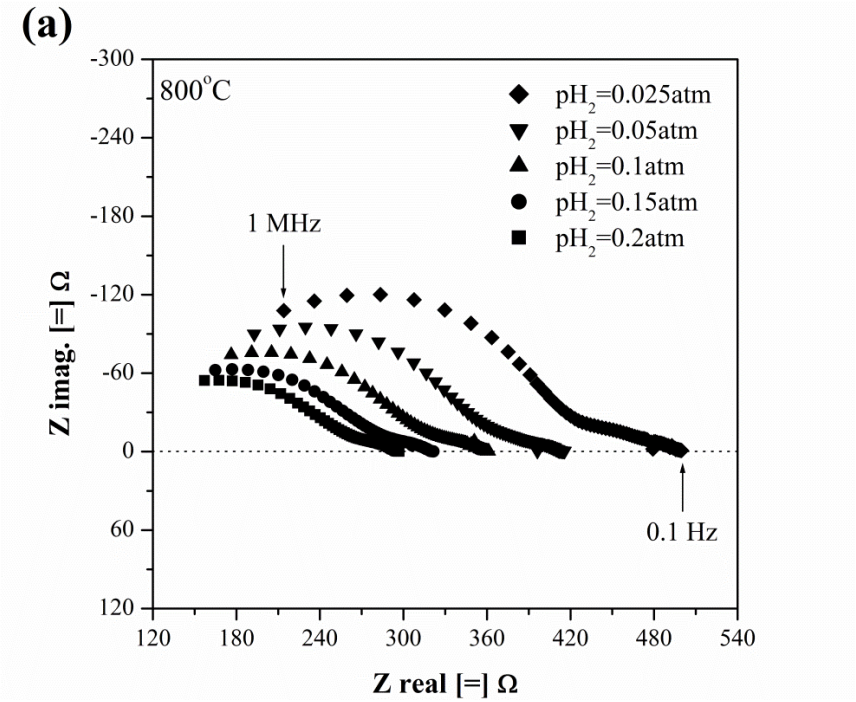

Figure 4.7: (a) EIS spectra obtained upon equilibration of BZF10 with H_2/H_2O/Ar exposure at 800°C; (b) EIS spectra obtained upon equilibration of BZF10 with H_2/H_2O/Ar exposure at 600°C; (c) Log-log plots of electrical conductivity versus H_2 partial pressures (pH_2) at 600-800°C; (d) Semi-log plots of σT versus 1000/T under H_2 exposure.

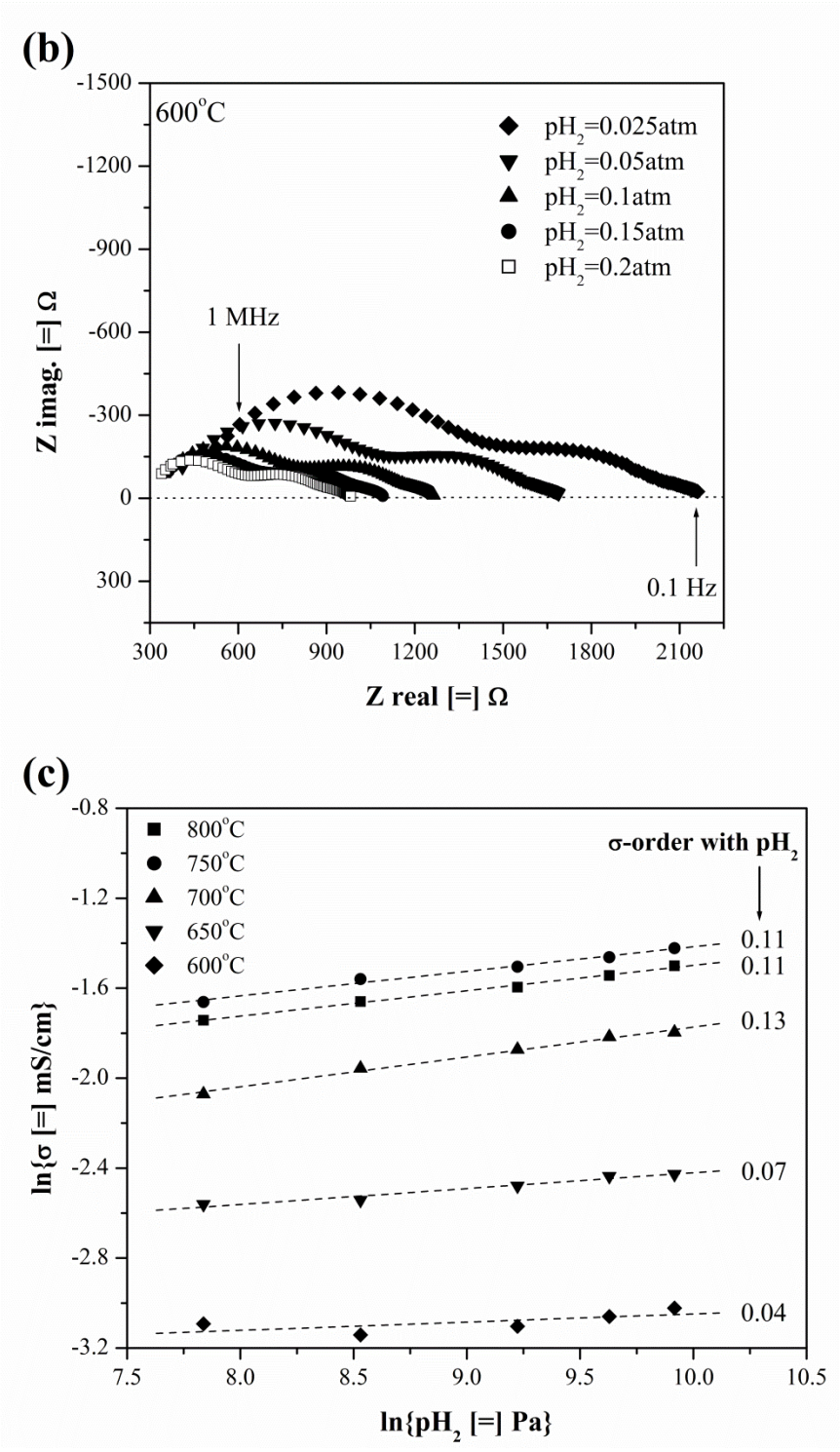

Figure 4.7: Continued

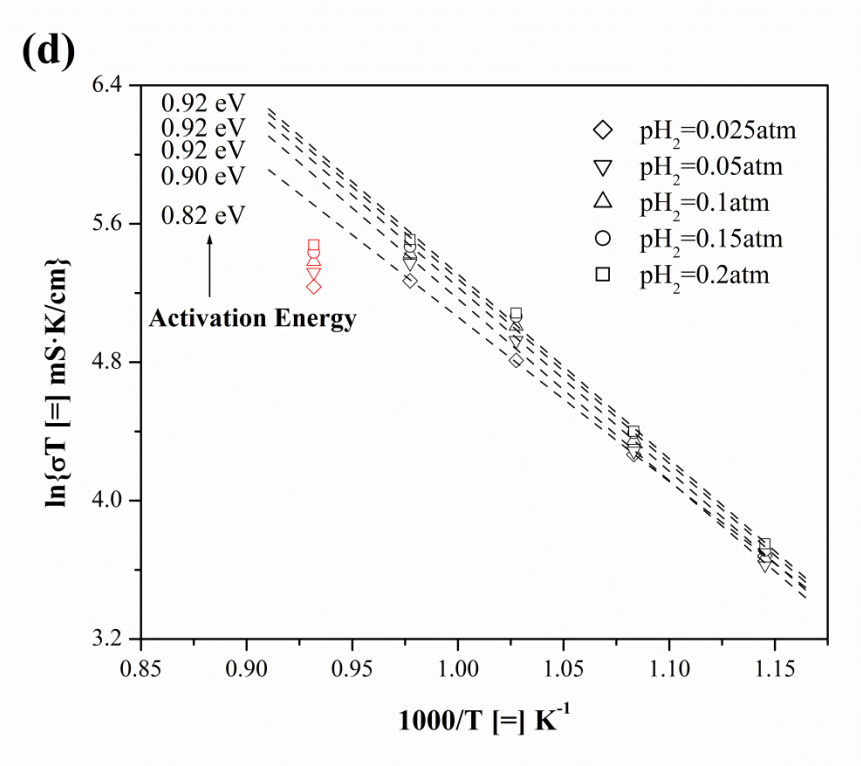

Figure 4.7: Continued

4.4.6 2nd dry O_2

Dry O_2 exposure (2nd O_2 exposure) was applied upon completing the above cycle of dry O_2, dry CO_2, H_2O, humidified CO, and humidified H_2 exposures, aiming to explore the reversible performance and recovery potential of the BZF10 cell in comparison to the 1st O_2 exposure result (Section 4.4.1). Nyquist plot of the reduced BZF10 material under dry O_2/Ar (Figure 4.8a) shows negligible grain boundary resistance due to the absence of the mid-frequency semi-circle. Power-law dependence of the electrical conductivity on O_2 partial pressure (pO_2) presented in Figure 4.8b is shown to be in better agreement with the expected + ¼-order dependence corresponding

to p-type semi-conduction behavior (Reaction 4.14) than prior to reducing gas exposure, while a ~ 85% reduction in electrical conductivity is also observed. Figure 4.8c presents the semi-log plots of σT verses 1000/T. The activation energy of BZF10 under this O_2 exposure is in the range of 0.31-0.36 eV at 600-800^{o}C, which is almost twice as large as that of the 1st O_2 exposure (0.16-0.18 eV).

$$\frac{1}{2}O_2 + V_O^{\bullet\bullet} \leftrightarrow O_O^X + 2h^{\bullet} \tag{4.14}$$

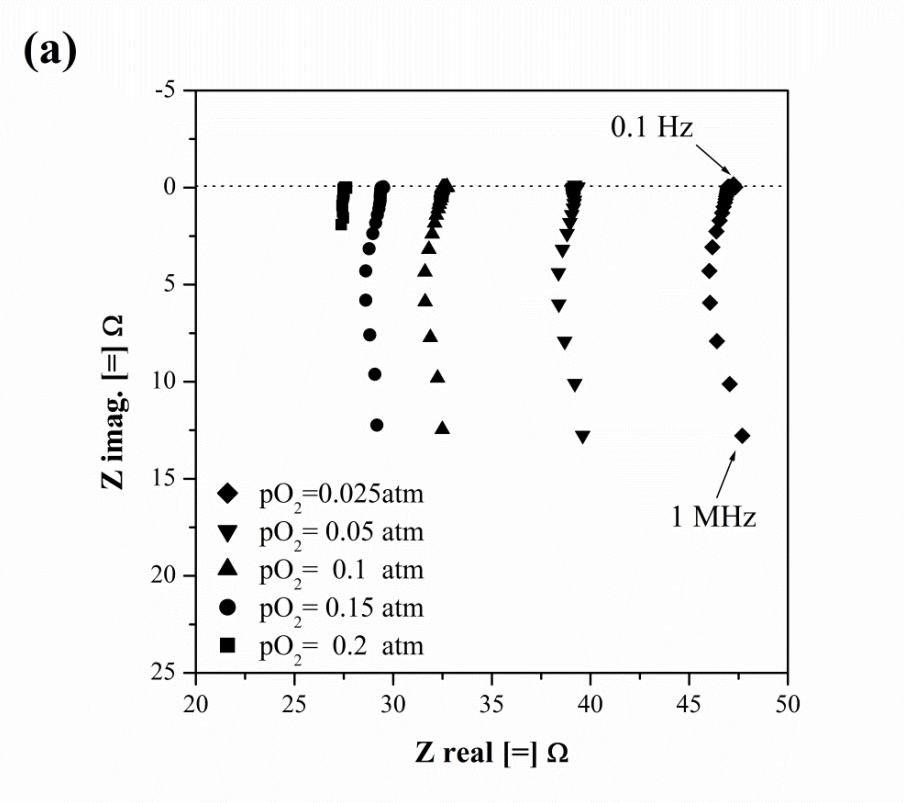

Figure 4.8: (a) EIS spectra obtained upon equilibration of BZF10 with dry O_2/Ar exposure at 800^{o}C; (b) Log-log plots of electrical conductivity versus O_2 partial pressures (pO_2) at 600-800^{o}C; (c) Semi-log plots of σT versus 1000/T under O_2 exposure.

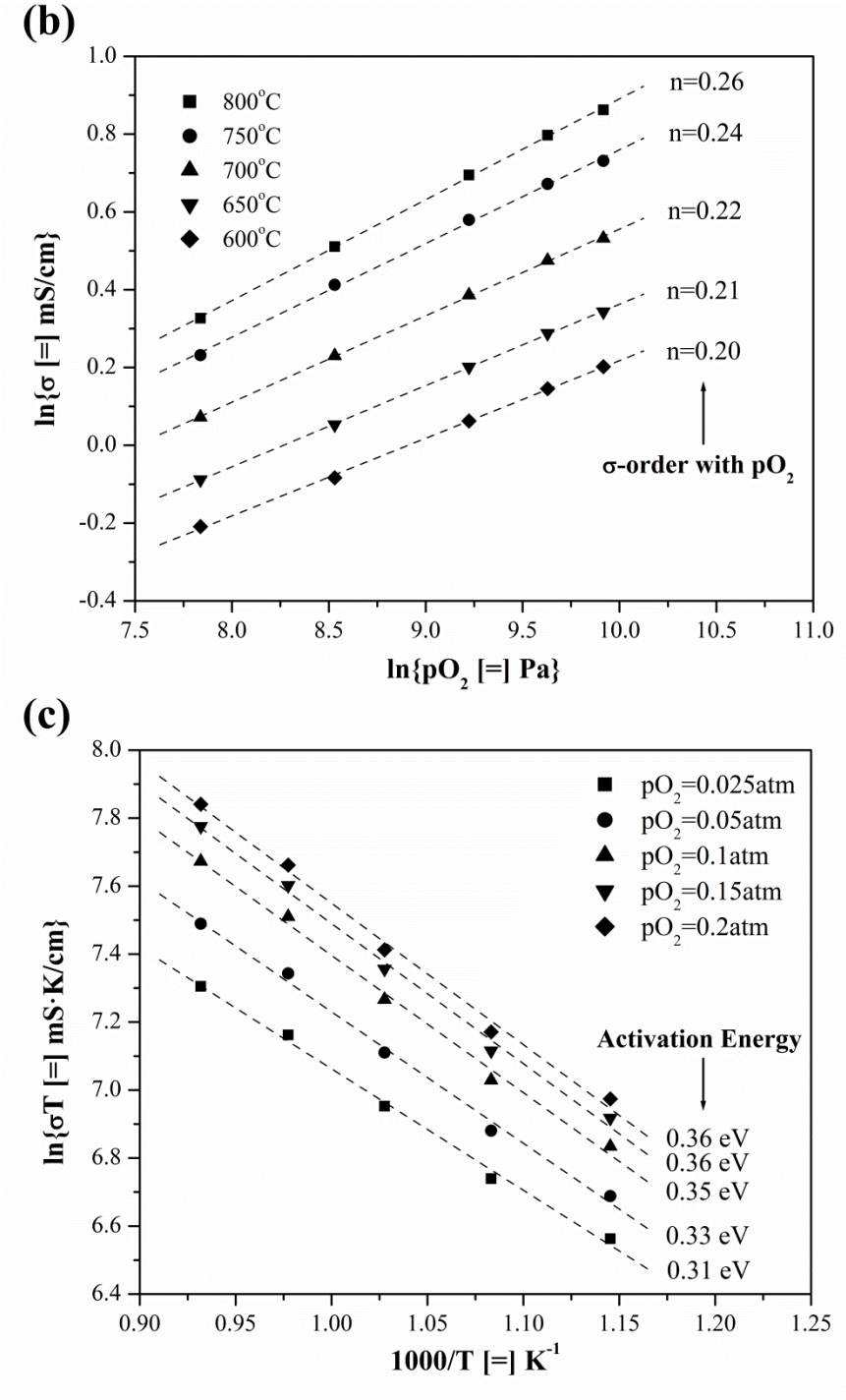

Figure 4.8: Continued

Figure 4.9 shows pictures of the 13mm button cell before and after testing, confirming the absence of any visible cracks, defects or degradation as a result of the above exposures at 600-800^{o}C, which indicates there is no disintegration or loss of mechanical stability during the whole button cell test. The total time on-stream for the pellet was ~1080 hours over the cycle of dry oxidizing, humidified inert, humidified reducing and dry oxidizing environments. Thus, this material is found to be mechanically stable over a range of both oxidizing and reducing gas environments associated with solid-oxide electrolytic cell (SOEC) and solid-oxide reversible fuel cell (SORFC) operations.

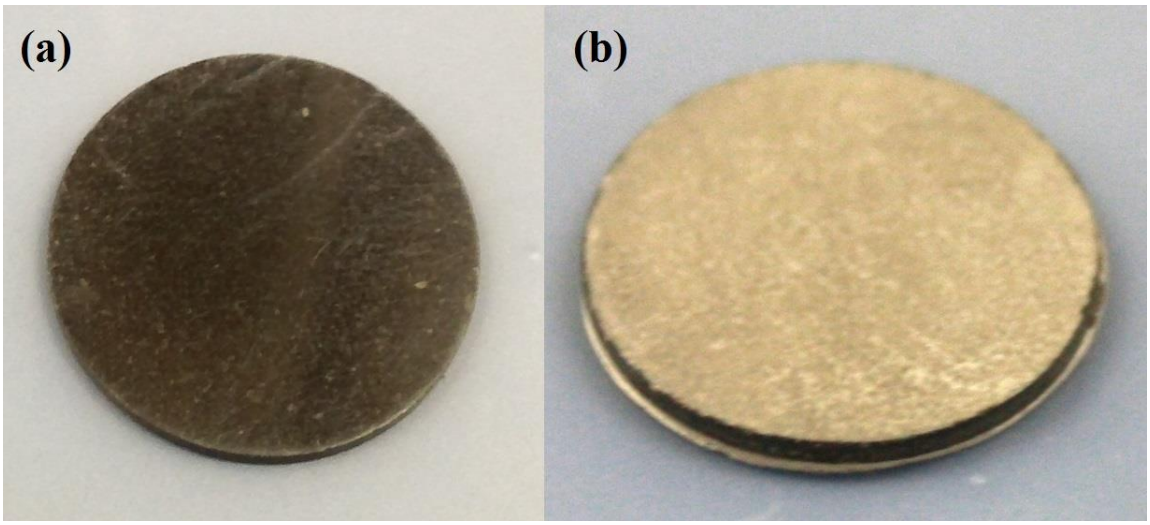

Figure 4.9: (a) Picture of the as-sintered pellet before all the tests; (b) Picture of the used pellet with porous Pt electrode on the top and blocking Pt electrode in the bottom after all the tests.

These observations suggest a subtle structure change during the above sequence of oxidizing and reducing gas exposures which introduces additional barriers to mobile

charge species transport, leading to the observed conductivity degradation at 600-800^{o}C. Material analysis (synchrotron XRD, TEM, STEM-XEDS, etc.) of the BZF10 pellet used in all gases exposure is proposed to verify the final phase composition and reveal the nature of conductivity degradation.

5. MATERIALS ANALYSIS OF THE AS-USED IRON-DOPED BARIUM ZIRCONATE PELLET*

5.1 Introduction

This chapter describes the detailed materials characterizations via synchrotron X-ray diffraction (XRD), transmission electron microscopy (TEM), scanning transmission electron microscopy coupled with energy dispersive X-ray spectroscopy (STEM-XEDS) on the as-exposed $BaZr_{0.9}Fe_{0.1}O_{3-\delta}$ (BZF10) pellet upon completion of >1,000 hours of continuous exposure to a range of oxidizing and reducing gas environments in comparison to the results obtained from the as-synthesized BZF10 material as discussed in Chapter 2 to assess the final, stable reduced perovskite microstructure and composition.

In Chapter 4, a ~80% conductivity degradation was observed after the 2nd oxygen exposure. Elemental maps via XEDS indicate Fe fully segregates into the intergranular region, which decreases the oxygen vacancies concentrations in the grains and closely corresponds to the conductivity drop after all gases test. Synchrotron XRD, TEM and diffraction pattern data all confirm the same $BaZrO_3$-based cubic structure as the primary phase in the material and the minor features are only in very small quantities. Results thus demonstrate the long-term materials stability of the acceptor-doped BZF10

* Part of this chapter is reprinted with permission from "Electrical Conduction and Reaction Analysis on Mixed Conducting Iron-Doped Barium Zirconates" by H. Zhang, B.A. Wilhite / Solid State Ionics 286 (2016) 7–18, http://dx.doi.org/10.1016/j.ssi.2015.11.023.

perovskites under both oxidizing and reducing environments at high temperatures (600-800^{o}C).

5.2 Experimental

5.2.1 Materials characterization

Upon completion of all gas exposure tests, a portion of the pellet was ground into powder and characterized by synchrotron X-ray diffraction analysis using a scan rate of 0.6^{o}/min and $0.5^{o} \leq 2\theta \leq 50^{o}$ scan range, at Advanced Photon Source, Argonne National Lab (IL, USA). Microscopy analysis of a fracture cross-section of the as-used BZF10 pellet and its chemical maps were investigated by transmission and scanning transmission electron microscopy (TEM & STEM) coupled with energy dispersive X-ray spectroscopy (XEDS). Cross-section TEM specimens were prepared by manual grinding and thinning of fractured samples, followed by dimpling and subsequent ion milling (PIPS 691 ion polishing system, 3.7 keV) to achieve suitably thin (electron-transparent) specimens. A TEM (FEI Tecnai G2 F20 ST microscope with a point resolution of 0.24 nm) operated at 200 kV and a TEM–STEM attachment of the same microscope operated at 200 kV were used for conventional and analytical imaging of the sample, respectively.

5.3 Results and discussions

5.3.1 Synchrotron XRD

Figure 5.1 presents the high-resolution XRD pattern obtained from the used BZF10 pellet (Figure 4.9b), which denotes the BZF10 pellet used in all gases exposure (O_2, CO_2, H_2O, CO, H_2, O_2), and the as-sintered BZF10 pellet (Figure 4.9a), respectively. A detailed analysis of the XRD pattern of the as-sintered sample (Figure 5.1b) was reported in Section 2.3.1. All the primary peaks from the reduced pellet sample (Figure 5.1a) could be indexed into a cubic perovskite phase structure with a lattice parameter of 4.19 Å, which is in agreement with that of the as-sintered sample (4.19 Å). The low-angle XRD data in Figure 5.1a is used to identify the minor features (secondary phases) in the material. Table 5.1 presents the d-spacing values which could not be indexed to the primary cubic phase. Those secondary phases match with patterns reported for materials from the Ba-O, Zr-O, Fe-O and Ba-Fe-O systems in the JCPDS Set-Cards. All the matched d-spacing values and the related space groups are presented in Table 5.1 for phase identification. All the secondary features are identified as a combined BaO, ZrO_2 and $BaFeO_{3-x}$ phases, while their low concentrations confirm that the material remained in a relatively pure perovskite phase. In comparison to the secondary phases revealed in the as-sintered sample, the high temperature wet reducing atmospheres exposure did not introduce new phase structure or increase the existed minor phase intensity, which indicates an overall chemical stability of the material under both oxidizing carbonaceous and reducing carbonaceous and non-carbonaceous environments.

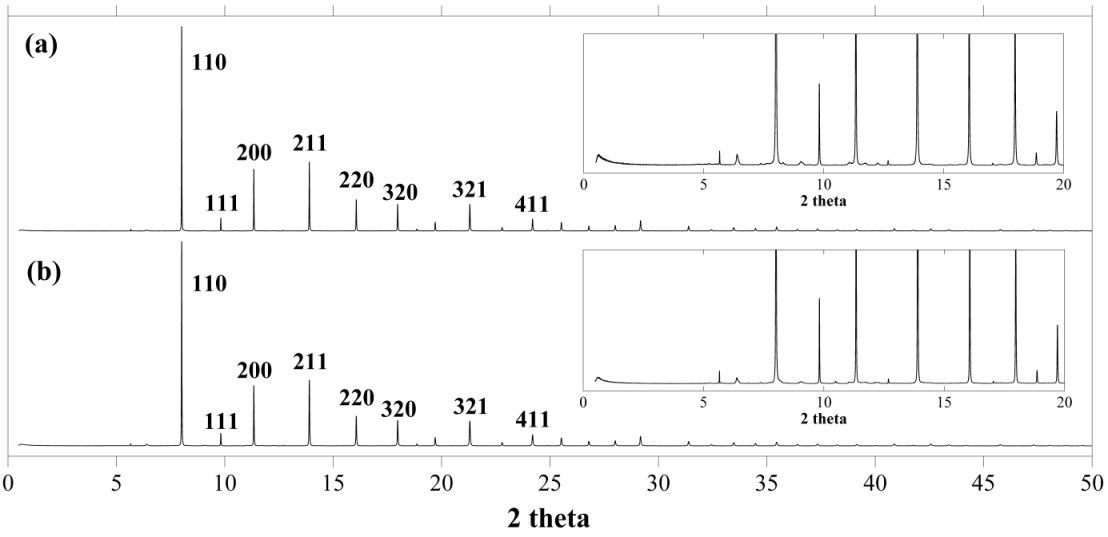

Figure 5.1: Synchrotron XRD patterns of BZF10. (a) used pellet; (b) as-synthesized pellet.

Table 5.1: Reported and measured d-spacing values.

Observed d-spacings (Å) (Secondary phases)	3.719	3.220	2.627	2.265	2.149	2.028	1.960	1.935
Reported d-spacings (Å) BaO (PDF#01-0746)		3.200 (111)					1.950 (220)	
Reported d-spacings (Å) ZrO_2 (PDF#65-2357)		3.207 (-111)	2.635 (020)			2.021 (-202)		

Table 5.1: Continued

Reported d-spacings (Å) FeO (PDF#06-0615)					2.153 (200)			
Reported d-spacings (Å) Fe_2O_3 (PDF#16-0653)		3.240 (022)	2.573 (-213)		2.176 (521)	2.018 (050)	1.973 (-441)	
Reported d-spacings (Å) $BaFeO_{2.9}$ (PDF#25-0068)	3.700 (105)			2.253 (205)	2.099 (207)	2.013 (208)		
Reported d-spacings (Å) $BaFeO_{2.6}$ (PDF#39-0183)	3.680 (003)		2.600 (230)	2.270 (134)	2.113 (054)	2.015 (208)	1.977 (073)	
Reported d-spacings (Å) $BaFeO_3$ (PDF#74-0646)	3.700 (015)			2.255 (205)	2.098 (027)	2.015 (208)	1.974 (10$\underline{13}$)	

Table 5.1: Continued

Reported d-spacings (Å) $BaFe_2O_4$ (PDF#25-1191)		3.160 (402)	2.590 (701)	2.265 (503)	2.110 (004)	2.051 (422)		1.930 (404)
Reported d-spacings (Å) $BaFe_2O_4$ (PDF#26-0158)		3.260 (102)	2.613 (111)	2.254 (004)	2.092 (202)	2.033 (104)		
Reported d-spacings (Å) $BaFe_2O_4$ (PDF#44-0897)		3.203 (102)	2.683 (110)	2.295 (112)		2.057 (202)		
Reported d-spacings (Å) $Ba_2Fe_2O_5$ (PDF#39-1296)	3.670 (610)*	3.210 (231)	2.652 (531)*	2.270 (541)	2.187 (740)*	2.068 (802)	1.984 ($\underline{11}$20)*	1.940 (160)*

* denotes low intensity peak. (nkl) denotes n, k, l in a 3D space. n, k, l are all integers. If it is above 9 (e.g. 11), the underline is used to identify the parameter. Underline denotes an integer above 9.

5.3.2 TEM, diffraction pattern and XEDS

The TEM images and their corresponding diffraction pattern data of the cross-section area of the used pellet are given in Figure 5.2a-d. Especially after humidified reducing gases exposure at 600-800^{o}C, the grains and grain boundaries (Figure 5.2a) remained well-defined without any visible structural degradation, indicating promising stability of the crystal structure of the Ba-Zr-Fe-O system under wet reductive atmosphere. The size of the polycrystalline grains after reduction was 0.3-1.0 μm (average ~0.7 μm), which was consistent with the grain size of the as-sintered pellet. Myriad cracks, initially formed during the ion-milling process, were still observed inside the grains without any significant growth during the reduction process and no mesh areas were created alongside the intergranular region, both of which indicate that negligible hydrolysis of BZF10 during wet reducing gases exposure at 600-800^{o}C. In a high magnification image of a specific grain (Figure 5.2c), well-defined grain boundaries were observed, while visible defects and cracks (attributing to sample preparation) indicates a brittle structure within the grain. High resolution TEM image (Figure 5.2d) presents multiple parallel well-structured (1,0,0) planes confirmed by the calculated d-spacing (~4.20 Å). A detailed analysis of diffraction pattern (Figure 5.2b) is given in Table 5.2. The polycrystalline structure of this reduced pellet was further confirmed by multiple concentric Debye rings observed in the diffraction pattern. All calculated d-spacings data based upon this sample slightly shifted to higher values, but were still in good match with the primary phase and secondary phases identified by synchrotron XRD technique. The diffraction pattern data did not reveal any additional secondary

phase formation through wet reduction while observed d-spacings indicated the presence of the original primary BZF10 phase along with minimal BaO, ZrO_2 and $BaFeO_{3-\delta}$.

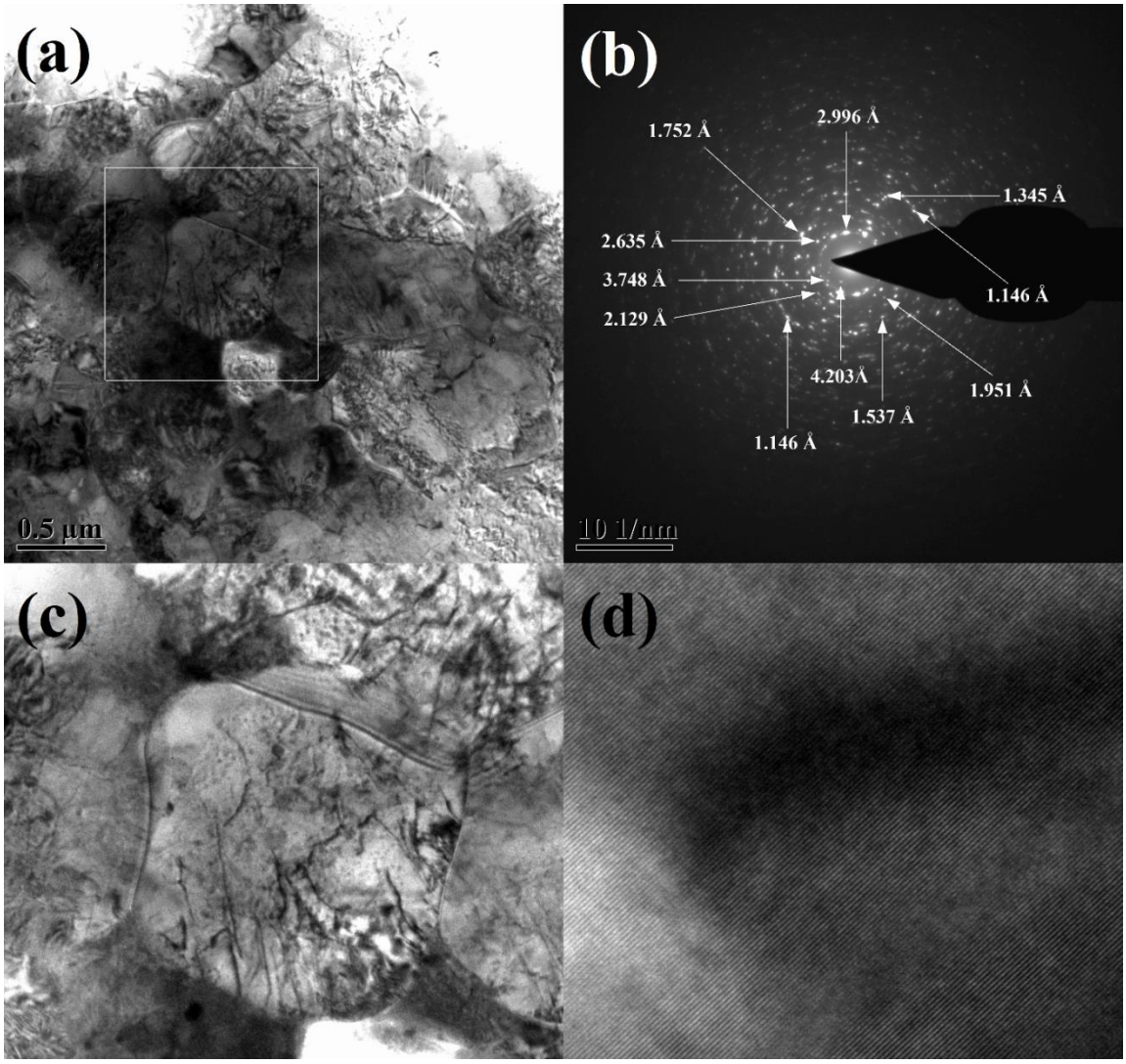

Figure 5.2: (a) TEM image of the used BZF10 pellet sample; (b) Diffraction pattern obtained from the crystalline grain structures of part (a); (c) High-resolution TEM image of the clear grain boundary; (d) High-resolution TEM image of a specific grain.

Table 5.2: Comparison and analysis of the calculated d-spacings from BZF10.

Calculated d-spacing (Å) (powder XRD)	Calculated d-spacing (Å) (as-sintered pellet DP)	Calculated d-spacing (Å) (as-used pellet DP)	Reported d-spacing (Å) ($BaZrO_3$) PDF#06-0399	Reported d-spacing (Å) ($BaFeO_3$) PDF#74-0646	Phase Identification
4.190 (100)	4.188	4.203	4.194 (100)	4.030 (104)	BZF10
3.712	3.727	3.748	--	3.700 (015)	$BaFeO_{3-\delta}$
2.964 (110)	2.955	2.996	2.965 (110)	2.845 (110)	BZF10
2.623	2.621	2.635	--	--	ZrO_2
2.095 (200)	2.096	2.129	2.097 (200)	2.098 (027)	BZF10
1.935	1.934	1.951	--	1.974 (10$\underline{13}$)	BaO
1.711 (211)	1.715	1.752	1.711 (211)	1.688 (217)	BZF10
1.482 (220)	1.480	1.537	1.482 (220)	1.422 (220)	BZF10
1.325 (310)	1.329	1.345	1.325 (310)	1.293 (137)	BZF10
1.120 (321)	1.125	1.146	1.120 (321)	1.128 (31$\underline{14}$)	BZF10
0.937 (420)	0.940	0.955	0.937 (420)	--	BZF10

(nkl) denotes n, k, l in a 3D space. N, k, l are all integers. If it is above 9 (e.g. 11), the underline is used to identify the parameter. Underline denotes an integer above 9.

The used pellet specimen was chemically and elementally mapped by STEM–XEDS for Ba, Zr and Fe (Figure 5.3). A specific grain and surrounding intergranular regions were chosen for elemental mapping to allow simultaneous mapping of representative grain and grain boundary regions. Ba was uniformly distributed throughout the material without any tendency of segregation, with the exception of a small localized intergranular area where Ba was absent (upper left part of Ba map). Zr primarily located within the grains, and comparison with previously reported STEM-XEDS of the as-sintered material indicates a great segregation of Zr in favor of grain regions after reduction. Fe signals increased within the grain boundaries while decreasing in the grains, as compared to the as-sintered sample, providing strong evidence that Fe had full segregated into the localized regions along the grain boundaries during reduction. These observations suggest that upon reduction of the as-sintered pellet Ba remains in both grain and grain boundaries in the formula of BaO while Zr diffuses into the grains to form ZrO_2 and Fe segregates in the form of FeO_x in regions where Zr amount is the lowest (intergranular regions) and where Ba is absent (upper left part of the map). This observation confirms that the grains are primarily comprised of pure barium zirconate ($BaZrO_3$) after reduction. In the grain boundary regions, FeO_x is present either in a Ba-lack region or alongside BaO forming a $BaFeO_{3-\delta}$ phase. Therefore, the intergranular phases may be identified as $FeO_x/BaFeO_{3-\delta}$, but the newly formed Fe-rich phase does not dominate the total electrical conductivity from dry oxidizing to wet reducing atmospheres.

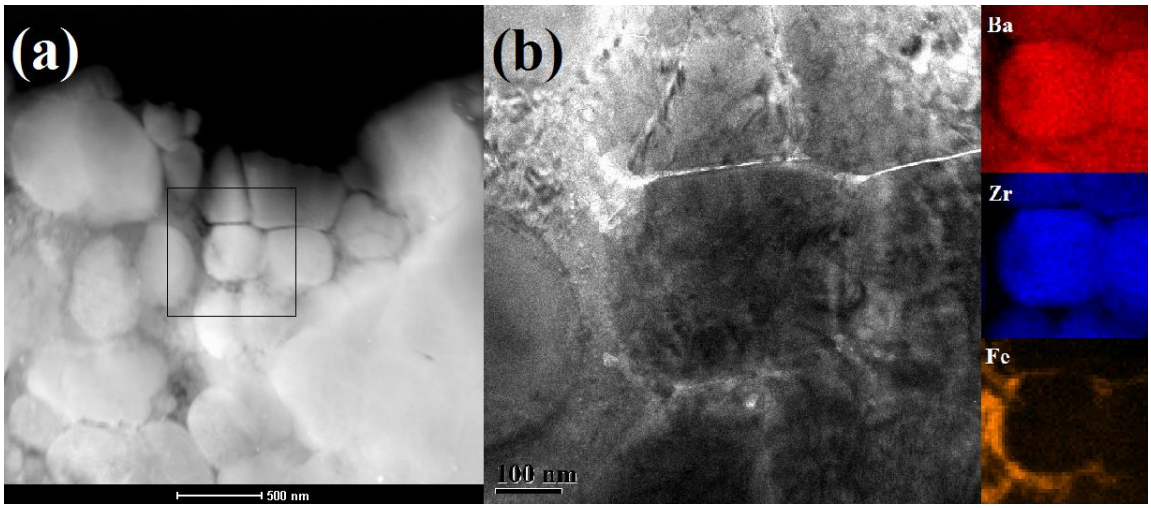

Figure 5.3: STEM-XEDS map obtained from the used pellet sample; (a) SEM image of prepared sample; (b) STEM image of sample with inset elemental maps for Ba, Zr and Fe.

Although the material analysis of the used sample via synchrotron XRD, TEM, diffraction pattern and STEM-XEDS all shows great consistency in phase structure with that of the as-sintered sample prior to all tests, subtle changes in minor quantities are also observed in this study. The chemical maps of Zr and Fe both indicate an irreversible elemental transportation during the high-temperature reducing gas exposure, which affects the minor phase composition and appears to be the primary reason of the conductivity degradation. The complete segregation of Fe in the intergranular region further reduced the dopant concentration inside the grains, which closely corresponds to the conductivity degradation by decreasing oxygen vacancy concentration.

6. ELECTRICAL CONDUCTION AND HYDROGEN PERMEATION OF IRON-DOPED BARIUM ZIRCONATE

6.1 Introduction

This chapter shows the hydrogen permeation investigation of 10% Fe-doped $BaZrO_3$ (BZF10) membrane. In Chapter 5, BZF10 is verified to be a mixed protonic and electronic conducting material under H_2 containing environments. The key advantage of the resulting mixed ionic-electronic conducting membrane for hydrogen production is that no external circuits is needed, thus offering an economic solution in comparison to power-based technologies.

Results show that in the examined thickness (0.97-1.40 mm), hydrogen permeation flux increases monotonically with the reciprocal of the membrane thickness, indicating bulk diffusion is the rate-limiting step and the hydrogen flux is comparable to other similar perovskite materials. In the range of 600-700^{o}C, the hydrogen permeation is limited by the electronic transport with higher activation energy; while in the range 700-900^{o}C, the hydrogen permeation is limited by the mixed protonic-electronic transport with low activation energy. Effect of steam on hydrogen permeation is also investigated. When the steam level reached 0.3 atm, hydrogen permeation process was promoted by the formation of extra protons in the form of hydroxyl ions. BZF10 membrane exhibits high mechanical and chemical stability over dry and humidified hydrogen containing gas environments.

6.2 Experimental

6.2.1 Membrane preparation and characterization

10% Fe-doped $BaZrO_3$ (BZF10) membranes were prepared from metal nitrate precursors using conventional solid-state reaction method, as follows. High purity nitrate powders of $Ba(NO_3)_2$ (Sigma-Aldrich, 99+%), $ZrO(NO_3)_2 \cdot 6H_2O$ (Aldrich Chemistry, 99%), and $Fe(NO_3)_3 \cdot 9H_2O$ (Sigma-Aldrich, ≥ 98%) were mixed and ground into powder. The blended powder was heat-treated at 1150^{o}C for 4 hours with heating and cooling rates 5^{o}C/min, followed by addition of acetone and grinding for 10 minutes to homogenize the partially calcined powder, followed by drying at 120^{o}C for 1 hour. The resulting powder was subsequently heat-treated at 1600^{o}C for 12 hours with heating and cooling rates 5^{o}C/min, ground again, and uniaxially pressed into pellets using a 25 mm die (Carver, 4369) at 199.6 MPa. The pellets were sintered at 1700^{o}C for 4 hours with heating and cooling rates 3^{o}C/min and polished to remove any surface contaminants. Relative density was measured by Archimedes test, as detailed in Section 2.2.2. The phase structures of the sintered disk were characterized by synchrotron XRD at Advanced Photon Source, Argonne National Lab (IL, USA). Microscopy analysis of fracture cross-section of the as-sintered BZF10 pellet and its chemical maps were investigated by scanning electron microscopy (SEM). An SEM (JEOL JSM-7500F) operated at 5 kV was used for conventional and analytical imaging of the sample.

6.2.2 Hydrogen permeation

Hydrogen permeation experiments were performed in a vertical high temperature 2-volume permeation cell presented schematically in Figure 6.1. Three polished dense

membranes with thickness 0.97, 1.15, 1.40 mm were prepared for the permeation test. Each membrane was sealed onto a supporting ceramic tube by filling the gap between the membrane and the supporting tube with a sealing mixture, comprised of a well-ground wet mixture of glass powder (VIOX # 10584), BZF10 powder, and sodium aluminate (Riedel-de Haën # 13404) of mass ratio 5:4:1. The mixture was manually ground with appropriate amount of deionized water to form a sticky paste. After the sealing was dried in air at room temperature for 2 hours, the supporting tube with attached membrane was sealed in the permeation set up and heated to 900^{o}C in air with heating and cooling rates 3^{o}C/min. After 30 minutes at 900^{o}C, pure He was introduced to the volume between the outer quartz tube and the inner ceramic tube (feed side) and pure Ar was introduced to the volume inside the inner ceramic tube (sweep side) continually. The He content of the sweep side was analyzed by a Gas Chromatography (Agilent 3000 Micro GC) to confirm a gas-tight seal. Once the He signal detected in the sweep reduced to a stable minimum ($\leq$ 0.003 mL/min), the system was cooled down to 600^{o}C immediately employed for hydrogen permeation measurement. H_2 balanced with an inert mixture gas (5%N_2 in Ar) was used in the feed stream and pure Ar was used in the sweep stream for all hydrogen permeation measurements. The gas flow rates on both sides were maintained at 100 mL/min via digital gas flow meters (Alicat Scientific Inc.). The effective membrane surface area was ~3.08 cm^2, which was determined by the surface area of membrane that was not covered by the sealing materials. Steady-state permeate stream gas composition was measured by GC. For all gas permeation tests, both permeate and retentate under 5 feed hydrogen partial pressures (0.025 – 0.20 atm)

at 600^{o}C and subsequently at 50^{o}C intervals up to 900^{o}C in dry conditions. Then the same measurements were taken at 700^{o}C with 3 different feed steam partial pressures 0.023, 0.097, 0.307 atm.

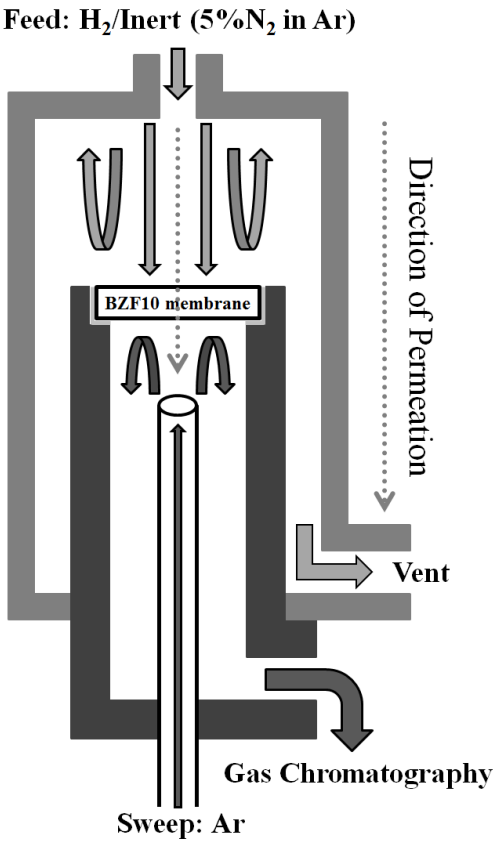

Figure 6.1: Schematic of two-chamber gas permeation cell.

6.3 Results and discussion

6.3.1 Membrane characterization

The membranes had a relative density of 92%. Measurement of the density of BZF10 yielded an average sintered density of 5.80 g/cm^3. Total porosity of the

membrane was measured to be 11.06% with a mean pore diameter of 10.25 nm. The sintered membrane has a dark grey color with good mechanical strength. No visible defects on the surface were found after polishing. Figure 6.2 presents the high resolution XRD patterns of BZF10 membrane prepared in this work. In this pattern, all the visible primary peaks can be indexed according to the standard JCPDS Set-Card of a cubic perovskite phase with a lattice parameter of a ~ 4.19Å. Secondary phases were determined to be BaO, ZrO_2, and $BaFeO_{3-x}$. It shows that the BZF10 membrane kept its single-phase perovskite structure after final sintering at 1700^{o}C.

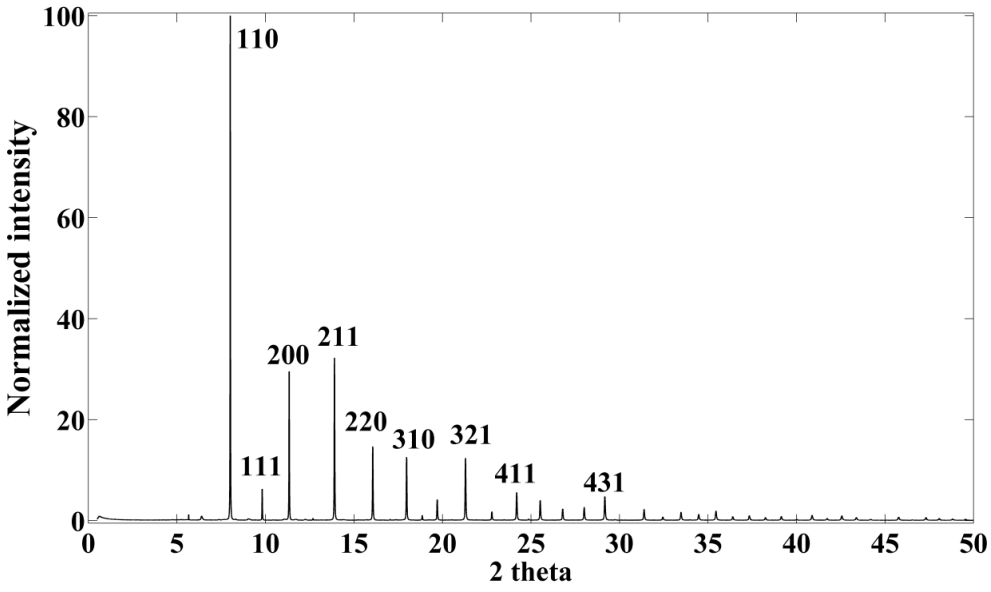

Figure 6.2: Synchrotron X-ray diffraction pattern of dense BZF10 membrane.

Figure 6.3a presents SEM images of the fracture surface of BZF10 membrane sintered at 1700^{o}C for 4 hours. The membrane appeared dense with well-defined grains and grain boundaries, and no open pores were found along the surface. The membrane

had a uniform grain size with average grain size in the range of 0.3 – 1 μm. Figure 6.3b presents the surface of the unpolished membrane, revealing the original ellipse-ball shape of the grains.

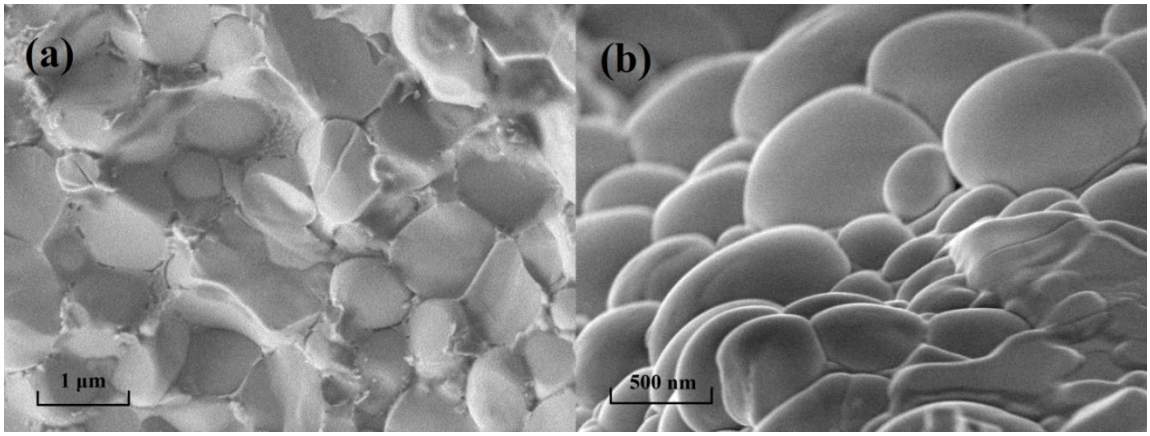

Figure 6.3: (a) SEM images of the fracture area of BZF10 membrane; (b) SEM images of the surface of unpolished BZF10 membrane.

6.3.2 Hydrogen permeation

Figure 6.4 shows the hydrogen permeation flux (J_{H_2}) versus the reciprocal of membrane thickness for BZF10 under identical conditions (900^{o}C, 20%H_2/inert in feed). The hydrogen permeation flux decreases with increasing membrane thickness. Theoretically, if the hydrogen permeation is limited by bulk diffusion, J_{H_2} is expected to be proportional to the reciprocal of the membrane thickness (L), as shown in Equation 6.1.

$$\frac{J_{H_2}(L_1)}{J_{H_2}(L_2)} = \frac{L_2}{L_1} \tag{6.1}$$

Alternatively, if surface kinetics limits permeation rates, Equation 6.2 is proposed:

$$\frac{J_{H_2}(L_1)}{J_{H_2}(L_2)} = const \tag{6.2}$$

In Figure 6.2, J_{H_2} is found to increase monotonically with L^{-1}, which suggests that bulk transport is the rate-limiting step. A perfect linear relationship is hard to achieve due to the smaller driving force for the thinner membrane. [156] The hydrogen flux data also provide insight to permeation behavior when surface reactions are at equilibrium.

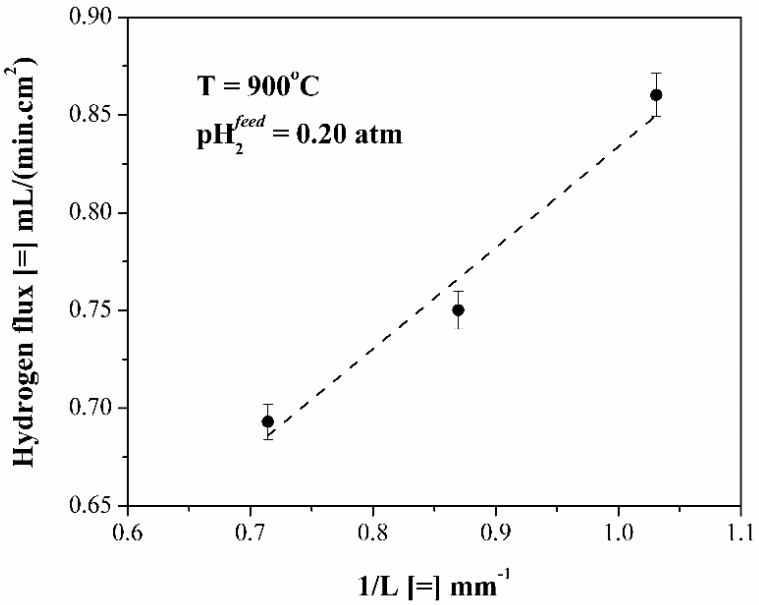

Figure 6.4: Hydrogen permeation flux versus membrane thickness for BZF10 membrane.

Figure 6.5 presents the effect of feed side hydrogen partial pressure (pH_2^{feed}) on the hydrogen permeation flux (J_{H_2}) for BZF10 membrane on a log-log plot. The hydrogen permeation flux increases with pH_2^{feed} due to the increase of the net driving

force for hydrogen transport and it can be fitted to power law order dependence upon pH_2^{feed} with n = 1.13 – 1.23 at 600-900°C (Equation 6.3).

$$J_{H_2} = (J_{H_2})_0 \cdot (pH_2^{feed})^n \tag{6.3}$$

The hydrogen permeability was determined by the hydrogen permeation flux (J_{H_2}), thickness of the membrane (L), and the hydrogen partial difference (Equation 6.4), which normalized the membrane thickness and the driving force, assuming 1st-order dependence on ΔpH_2, following the traditional relationship between driving force and flux for gas separation membranes. [199] The highest hydrogen permeation flux observed was 0.75 mL/(min·cm^2) at 900°C when 20%H_2/Ar was used as feed gas, and the resulting hydrogen permeability was 3.58×10^{-10} mol/(m·Pa·s).

$$Permeability\big|_{H_2} = J_{H_2} \cdot \frac{L}{pH_2^{feed} - pH_2^{sweep}} \tag{6.4}$$

Figure 6.6 shows the effect of temperature on hydrogen permeability through BZF10 membrane. The hydrogen permeability increased with temperature significantly in the low temperature range and tended to level off at higher temperatures up to 900°C. At higher temperatures (≥ 700°C), the weaker dependence of hydrogen permeability upon temperature may be attributed to the increasing amount of H_2 permeated to the sweep side compensating the increase of driving force for H_2 permeation.

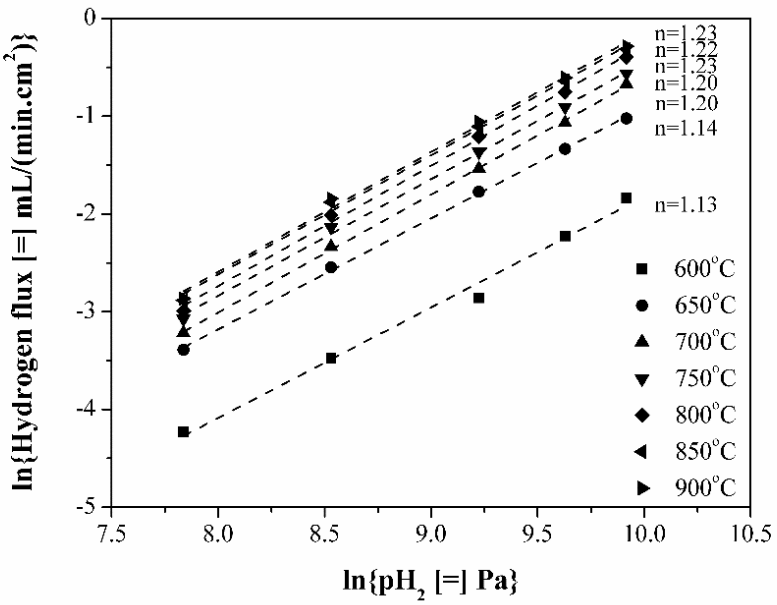

Figure 6.5: Log-log plots of feed hydrogen partial pressure versus hydrogen permeation flux of BZF10 membrane.

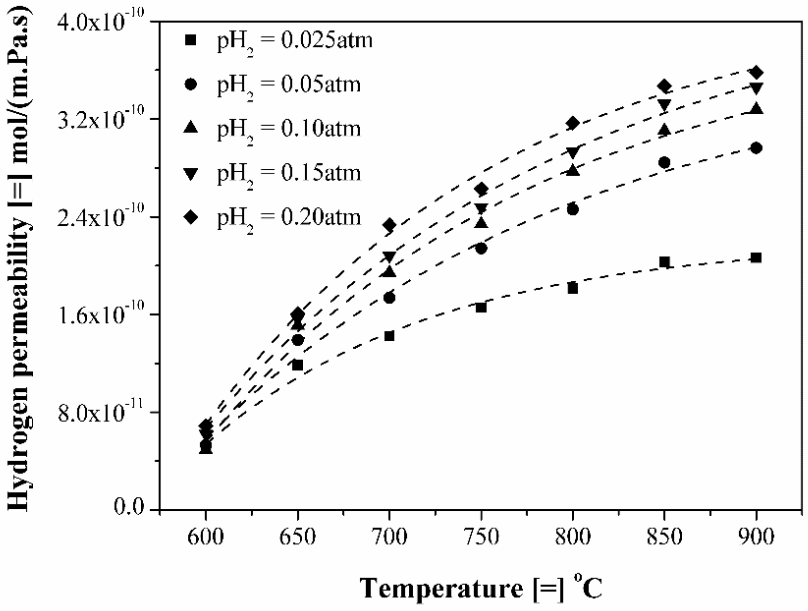

Figure 6.6: Hydrogen permeability versus temperature for BZF10 membrane.

Figure 6.7 shows the effects of temperature on hydrogen permeation flux through BZF10 membrane with different pH_2^{feed} . J_{H_2} is found to increase with increasing temperature since both bulk diffusion and surface kinetics are promoted at higher temperature. The Arrhenius plot presents two distinct regions corresponding to low (≤ 700^{o}C) and high (≥ 700^{o}C) temperature at 0.025 atm ≤ pH_2^{feed} ≤ 0.20 atm, suggesting a mechanism change of the mixed protonic-electronic semi-conduction around 700^{o}C, thus introducing two different activation energies corresponding to the two regions, respectively. In the lower temperature region, a higher activation energy (72 – 94 kJ/mol) was determined, while in the higher temperature region, a lower activation energy (18 – 23 kJ/mol) was determined.

A possible explanation for two distinct activation energies was presented by Cheng et al. [200], who proposed that hydrogen permeation is limited by the electronic transport in the lower temperature range (600-700^{o}C), while mixed protonic-electronic transport is limiting in the higher temperature range (700-900^{o}C). It is difficult to separate protonic conductivity (σ_{H^+}) and electronic conductivity (σ_{e^-}) from the electrochemical measurement under H_2/inert atmospheres on BZF10, while it is reasonable to conform to this interpretation based upon the following reasons. Firstly, it was reported by Iwahara et al. [201] that the activation energies of σ_{H^+} and σ_{e^-} for $SrCe_{0.95}Yb_{0.05}O_{3-\alpha}$ were 40 kJ/mol and 140 kJ/mol, respectively, the difference in magnitude of which should be comparable to the activation energies corresponding to σ_{H^+} and σ_{e^-} for BZF10. Secondly, the doping of iron may promote σ_{e^-} due to the good

transition capability of Fe^{2+}/Fe^{3+}; in higher temperature region, σ_{e^-} may become comparable to σ_{H^+} and contribute to a conduction mechanism change. Thus, the primary reason of the lower activation energy at high temperature is the increasing of electronic conductivity.

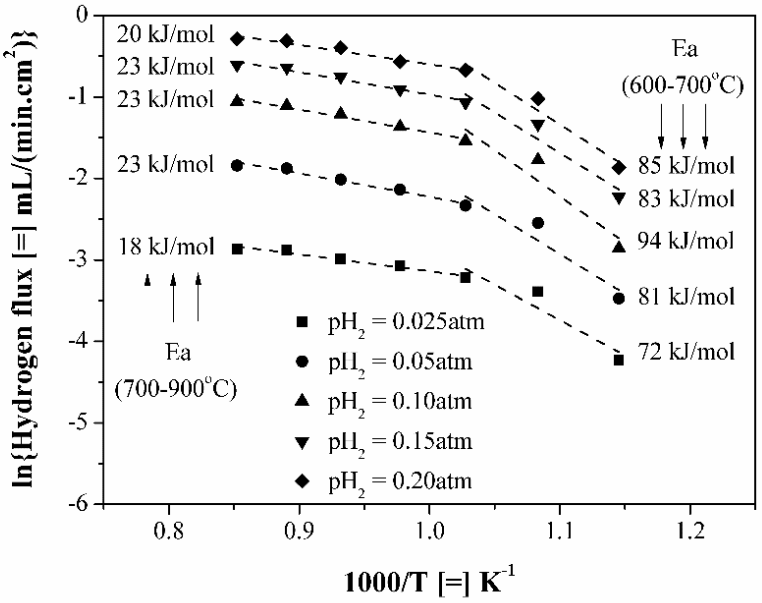

Figure 6.7: Semi-log plots of temperature dependence of hydrogen permeation flux of BZF10 membrane.

Figure 6.8 presents the hydrogen permeation flux verse pH_2^{feed} at 700°C with existence of water. It shows that J_{H_2} was not largely influenced when the addition of water vapor was relatively low (below 0.1 atm). This observation is consistent with Section 4.4.3 which showed that neither the protonic conduction nor the electronic conduction within BZF10 was promoted when exposed to steam up to pH_2O = 0.2 atm.

When the water vapor level was increased to ~0.3 atm the measured hydrogen flux increased clearly, indicating a change in mechanism. This promotion of hydrogen permeation by steam partial pressure > 0.3 atm may be explained as follows. Hydrogen permeation flux through a mixed protonic-electronic conducting membrane under bulk diffusion-controlled conditions is described by the Wagner equation (Equation 6.5):

$$J_{H_2} = \frac{RT}{4F^2L} \cdot \int_{pH_2^{feed}}^{pH_2^{sweep}} \frac{\sigma_{OH^\bullet}(\sigma_{h^\bullet} + \sigma_{e'})}{\sigma_t} d\ln(pH_2) \tag{6.5}$$

where F is the Faraday constant, L is the thickness of membrane, σ_i is the partial conductivity of defect species i. Subscripts $OH^\bullet$, $h^\bullet$, e', and t denote proton (in the form of hydroxyl ion by combining with an oxygen ion in its neighborhood), electron hole, electron, and total defect species, respectively. Thus, J_{H_2} is determined by the concentration of charge carriers which is dictated by gaseous species H_2O, and H_2 via equilibrium reactions (Equation 4.7, 4.12). As demonstrated in Section 4.4, Reaction 4.7 may be facilitated in sufficiently humidified reducing environments (i.e. $H_2O/H_2/Ar$, $H_2O/CO/Ar$), thus producing additional hydroxyl ions with increasing steam partial pressure. Hydrogen flux increases due to the increase of driving force for proton transport, suggesting the amount of water vapor as high as 0.3 atm can promote the hydrogen permeation.

The total time on-stream for the BZF10 membrane was above 200 hours in both dry and humidified reducing environments at 600-900^{o}C. This material did not show any tendency to become fragile after completion of permeation experiments, but remained mechanically and chemically stable during the whole process.

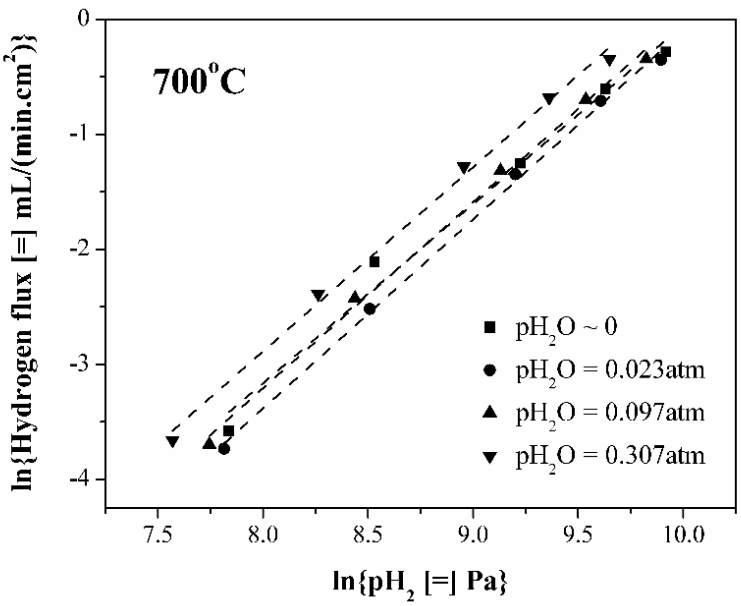

Figure 6.8: Hydrogen permeation flux versus hydrogen partial pressure at 700°C in wet conditions.

Table 6.1 provides a comparison of presently reported hydrogen permeability against literature values of similar perovskite membranes. Since literature hydrogen flux data are reported over a range of conditions, it is difficult to evaluate the membrane performance with J_{H_2} using actual permeation rates; for this reason a 1st-order relationship between driving force and permeability is assumed. From Table 6.1, BZF10 membrane is found to have comparable hydrogen permeability to other well-studied electroceramic materials.

Table 6.1: Comparison of hydrogen permeation flux / hydrogen permeability between BZF10 and similar perovskite materials in various atmospheres.

Perovskite Composition	J_{H_2} at 900°C	pH_2^{feed}	L	Permeability at 900°C	E_a	T range	Membrane surface coating	Reference
	mL/(min·cm^2)	atm	mm	mol/(m·Pa·s)	kJ/mol	°C		
$BaZr_{0.9}Fe_{0.1}O_{3-\delta}$	0.347	0.1	1.15	3.28×10^{-10}	94.3	600-700	No	This work
					23.3	700-900		
$SrCe_{0.95}Tm_{0.05}O_{3-\delta}$	0.0766	0.1	0.8	6.47×10^{-11}	111.5	600-700	No	[200]
					12.32	700-950		
$SrCe_{0.95}Y_{0.05}O_{3-\delta}$	0.0615	0.8	0.05	2.82×10^{-13}	132	750-950	No	[202]
	0.137	0.8	0.056	7.04×10^{-13}	107		Yes	
$SrCe_{0.95}Yb_{0.05}O_{3-\delta}$	0.0228	0.01	1.0	1.68×10^{-10}	N.A.	900	Yes	[203]
SCZY/Ni-SCZY	4.122 (800°C)	0.0493	1.0	6.14×10^{-9} (800°C)	N.A.	500-800	No	[163]

*SCZY/Ni-SCZY: $Sr(Ce_{0.6}Zr_{0.4})_{0.85}Y_{0.15}O_{3-\delta}$/Ni-$Sr(Ce_{0.6}Zr_{0.4})_{0.85}Y_{0.15}O_{3-\delta}$

BZF10 membrane was found to exhibit noticeable oxygen permeation flux in Section 3.4.2. The highest oxygen permeation flux was measured to be 0.101 mL/(min·cm^2) at 900^{o}C with air/Ar gradient, which is relatively low compared to the highest hydrogen permeation flux of 0.75 mL/(min·cm^2) also at 900^{o}C when 20%H_2/Ar was used as feed gas. Since this electroceramic material is found to 1) exhibit mixed ionic-electronic conduction under oxidizing conditions; 2) exhibit mixed protonic-electronic conduction under both dry and humidified reducing conditions; 3) retain high materials stability under both oxidizing and reducing conditions, it may be a promising material for multiple electrochemical or non-galvanic membrane applications, such as hydrogen production via water splitting or methane dimerization.

7. CONCLUSIONS AND RECOMMENDATIONS FOR FUTURE WORK*

7.1 Conclusions

This dissertation presents the first investigation of a novel mixed conducting $BaZr_{0.9}Fe_{0.1}O_{3-\delta}$ perovskite (BZF10) in terms of electrochemical, catalytic properties, membrane separation and material characterization over a complete span of gas environments (O_2, CO_2, H_2O, CO, H_2). This electroceramic material is found to exhibit both mixed ionic-electronic conduction under oxidizing conditions and mixed protonic-electronic conduction under humidified reducing conditions. This unique combination of electrical conduction, catalytic activity and long-term material stability makes this material a promising candidate for solid-oxide electrolytic cells (SOEC) and solid-oxide reversible fuel cells (SORFC) applications.

In Chapter 2, powder of BZF10 was synthesized via solid-state reaction at 1600^{o}C. Elemental analysis indicated a Ba deficiency in the powder relative to the expected composition ($BaZr_{0.90}Fe_{0.10}O_{3-\delta}$) owing to Ba volatilization during calcination. The powder was characterized using synchrotron XRD; results indicated the presence of a primary cubic $BaZrO_3$-based perovskite phase. The powder was pressed into pellets and sintered at 1700^{o}C. TEM images and elemental maps via XEDS indicate stable grain

* Part of this chapter is reprinted with permission from "Materials Synthesizing, Electrochemical Characterization and O_2 Permeation Properties of Fe-Doped Barium Zirconates" by H. Zhang et al. / Solid State Ionics 266 (2014) 58–67, http://dx.doi.org/10.1016/j.ssi.2014.08.011; and "Electrical Conduction and Reaction Analysis on Mixed Conducting Iron-Doped Barium Zirconates" by H. Zhang, B.A. Wilhite / Solid State Ionics 286 (2016) 7–18, http://dx.doi.org/10.1016/j.ssi.2015.11.023.

structure and well-defined grain boundaries within the pellet and transition metal distribution on the grains surface.

In Chapter 3, Electrical conductivity relaxation (ECR) was carried out on the sintered pellet between 600 and 800^{o}C under a wide range of oxygen partial pressures (pO_2). ECR indicates that both chemical diffusion coefficient D_V and surface kinetic parameter *k'* increase with increasing pO_2. The oxygen permeation flux through BZF10 membrane at 900^{o}C is 0.102 mL/(min·cm^2). The material was observed to be electrochemically and mechanically stable over both electrochemical and permeation tests, which is especially significant for its implementation in high-temperature energy applications.

In Chapter 4, Electrochemical Impedance Spectroscopy (EIS) and effluent gasses analysis were carried out at 600-800^{o}C under a wide range of gas environments. Under dry O_2 conditions, this material displays p-type semi-conduction behavior, suggesting oxygen-acceptor activity via reaction with oxygen vacancies. Upon exposure to dry CO_2 atmosphere, the material shows catalytic activity towards CO_2 reduction to CO and O_2 which is attributed to an intermediate carbonate ion formation on the cell surface. Exposure to moisture inert suggests only mild interaction with steam, indicating either equivalent hydroxyl-ion and oxygen-vacancy conductivity or negligible activity for steam hydrolysis in the absence of co-reactants. Under moist CO environment, a complex conduction mechanism is displayed alongside significant rates of water-gas-shift reaction coinciding with an initial increase in electrical conductivity at low CO partial pressure (*pCO*) and subsequent decrease in electrical conductivity at high *pCO*.

Exposure to humidified H_2 results in increase in conductivity with pH_2, indicating n-type semi-conduction under this gas environment.

In Chapter 5, upon completion of >1,000 hours of continuous exposure to a range of oxidizing and reducing gas environments, physical inspection of the BZF10 electrochemical cell indicated negligible chemical or mechanical degradation. The pellet used in all gases exposure experiments was characterized using synchrotron XRD, TEM, diffraction patterns, and STEM-XEDS, indicating stable phase composition and stable grain structure within the pellet. Elemental maps via XEDS indicate Fe segregates fully into the intergranular region, which closely corresponds to the conductivity drop after all gases test.

In Chapter 6, hydrogen permeation flux (J_{H_2}) is proportional to the reciprocal of the membrane thickness, indicating bulk diffusion is the rate-limiting step. In the range of 600-700^{o}C, the hydrogen permeation is limited by the electronic transport with higher activation energy; while in the range 700-900^{o}C, the hydrogen permeation is limited by the mixed protonic-electronic transport with low activation energy. When the steam level reached 0.3 atm, hydrogen permeation process was promoted by the formation of extra protons in the form of $OH^{\bullet}$. BZF10 membrane is found to be mechanically and chemically stable over dry and humidified hydrogen containing gas environments.

7.2 Recommendations for future work

7.2.1 First-principles simulations of BZF10

First-principles simulations of single phase crystals can offer prediction of thermodynamic properties, electronic conductivities, band-gap values, and defect diffusivities in a variety of ceramic materials. The result is helpful for constructing ternary phase diagrams to predict phase equilibria and phase stability within Fe-doped $BaZrO_3$. The simulations of ionic and electronic transport of individual phases can provide the ionic and electronic conductivities estimation within the heterogeneous electroceramics. Experimental results in Chapter 2-4 can be used to validate the above simulations for the design of optimal materials from the Ba-Zr-Fe-O system.

7.2.2 Thermal gravimetric analysis (TGA)

Thermal gravimetric analysis measures the transient mass change of the powder sample when exposed to a gas condition or temperature change. In perovskite-type materials, the corresponding mass change directly reflects the change in the ionic and electronic defects concentrations by the oxygen vacancy filling and releasing from the lattice. TGA data supplements the ECR and EIS results for the charge carrier concentration as well as the electrochemical reaction rate.

7.2.3 Concentration-cell analysis

The concentration cell technique requires a two-side cell with Pt electrodes annealed on both faces, sealed into two gas volumes. Contrasting gas compositions are flowed through each volume to maintain an oxygen or hydrogen gradient, generating an electric potential from the electronic and ionic conductivity change. Effluent gasses are

measured by gas chromatography or mass spectroscopy to confirm the electrochemical reactions occurred in the cathode and anode regions, respectively.

7.2.4 Reactive membrane tests and modeling

Both experimental and modeling work will be investigated to study the electrochemical reduction of CO_2 and the integration with water-gas-shift reaction on BZF10 membrane, in order to provide evidence of the overall catalytic reaction rates and reaction pathway selectivity. This work aims to realize the combined catalytic-electrochemical conversion of waste CO_2, H_2O to syn-gas, which can be converted to synthetic petroleum products via Fischer-Tropsch synthesis (FTS) technologies.

NOMENCLATURE

a	Lattice parameter of a cubic perovskite structure, Å
A	Surface area of membrane, m^2
C_V	Concentration of oxygen vacancy, mol/m^3
$C_{V,0}$	Initial concentration of oxygen vacancy, mol/m^3
$C_{V,eq}$	Equilibrated molar concentrations of oxygen vacancy, mol/m^3
$C_V(x,t)$	Instantaneous molar concentrations of oxygen vacancy, mol/m^3
$C_V(\infty)$	Equilibrated molar concentrations of oxygen vacancy, mol/m^3
d_p	Diameter of pellet, m
D_V	Diffusivity of oxygen vacancy, m^2/s
e	Charge of an electron hole, C
E_a	Activation energy, eV or kJ/mol
F	Faraday constant, C/mol
$\Delta H^f_{D_V}$	Formation energy of oxygen vacancy, J
$\Delta H^m_{D_V}$	Migration energy of oxygen vacancy, J
J_{H_2}	H_2 permeation flux, $mL/(min \cdot cm^2)$
J_{O_2}	O_2 permeation flux, $mL/(min \cdot cm^2)$

k'	Surface kinetic parameter, m/s
K_{oxid}	Equilibrium constant of Reaction 1.5, $1/(Pa^{0.5}\cdot m^6)$
K_{red}	Equilibrium constant of Reaction 1.9, $Pa^{0.5}/m^6$
L	Thickness of O_2/H_2 permeation membrane, mm
m_A	Mass of A, kg
m_B	Mass of B, kg
n	Concentration of mobile electrons, $1/m^3$
p	Concentration of mobile holes, $1/m^3$
pCO	Partial pressure of CO, Pa
pCO_2	Partial pressure of CO_2, Pa
pH_2	Partial pressure of H_2, Pa
pH_2^{feed}	Partial pressure of H_2 in the feed side, Pa
pH_2^{sweep}	Partial pressure of H_2 in the sweep side, Pa
pH_2O	Partial pressure of steam, Pa
pO_2	Partial pressure of O_2, Pa
pO_2^{feed}	Partial pressure of O_2 in the feed side, Pa
pO_2^{sweep}	Partial pressure of O_2 in the sweep side, Pa
q	Gas flow rate, mL/min

R	Gas constant, J/(mol·K)
R_A	Radius of A-site element, m
R_B	Radius of B-site element, m
R_O	Radius of oxygen, m
R_∞	First x-axis intercept of Nyquist spectra, Ω
t	Time, s
T	Temperature, K
t_f	Tolerance factor of perovskite structure, dimensionless
t_p	Thickness of pellet, m
x	Axial position, m

Greek Letters

δ	Oxygen nonstoichiometry, dimensionless
θ	Angles that X-ray scans, ^{o}.
λ_n	The positive roots of the transcendental equation, dimensionless
μ_i	Mobility of ions, $cm^2/(V \cdot s)$
μ_p	Mobility of holes, $cm^2/(V \cdot s)$
ρ_{air}	Density of air, g/cm^3
ρ_{BZF10}	Density of BZF10, g/cm^3

$\rho_{ethanol}$	Density of ethanol, g/cm^3
σ	Electrical conductivity, mS/cm
$\sigma(0)$	Initial electrical conductivity, mS/cm
$\sigma(\infty)$	Equilibrated electrical conductivity, mS/cm
$\sigma_{ECR}(\infty)$	Equilibrated electrical conductivity obtained from ECR, mS/cm
σ_{EIS}	Electrical conductivity obtained from EIS experiments, mS/cm
σ_{ion}	Ionic conductivity, mS/cm
σ_i	Partial conductivity of defect species *i*, mS/cm
σ_n	n-type conductivity, mS/cm
σ_p	p-type conductivity, mS/cm
σ_{total}	Total electrical conductivity, mS/cm
$\hat{\sigma}$	Normalized electrical conductivity, dimensionless

Abbreviation

*BZF*10	$BaZr_{0.9}Fe_{0.1}O_{3-\delta}$
DP	Diffraction pattern
ECR	Electrical conductivity relaxation
EIS	Electrochemical impedance spectroscopy
GC	Gas chromatography

GHG	Greenhouse gasses
MIEC	Mixed ionic-electronic conducting
MS	Mass spectrometer
PIXE	Proton induced X-ray emission
SEM	Scanning electron microscopy
SOEC	Solid oxide electrolysis cell
SOFC	Solid oxide fuel cell
SORFC	Solid oxide reversible fuel cell
STEM	Scanning transmission electron microscopy
TEM	Transmission electron microscopy
TGA	Thermal gravimetric analysis
UHP	Ultra-high purity
XEDS	Energy dispersive X-ray spectroscopy
XRD	X-ray diffraction

Defect and surface species

$CO_{3\ (s)}^{2-}$	Surface carbonate ion
e'	Electrons
$Fe_{Zr}^{'}$	Fe^{3+} cation substitution for Zr^{4+}
H^{+}	Protons
$h^{\bullet}$	Electron holes

O^{2-}	Oxygen ions
O_O^X	Lattice oxygen
$OH_O^\bullet$	Hydroxyl ions
$V_O^{\bullet\bullet}$	Oxygen vacancy

REFERENCES

[1] M.A. Pena, J.L.G. Fierro, Chem. Rev. 101 (2001) 1981-2017.

[2] J.W. Stevenson, T.R. Armstrong, R.D. Carneim, L.R. Pederson, W.J. Weber, J. Electrochem. Soc. 143 (1996) 2722-2729.

[3] E. Fabbri, T. Oh, S. Licoccia, E. Traversa, E.D. Wachsman, J. Electrochem. Soc. 156 (2009) B38-B45.

[4] Y. Maeno, H. Hashimoto, K. Yoshida, S. Nishizaki, T. Fujita, J.G. Bednorz, F. Lichtenberg, Nature 372 (1994) 532-534.

[5] S. Zhang, R. Xia, T.R. Shrout, G. Zang, J. Wang, J. Appl. Phys. 100 (2006) 104108.

[6] G.A. Samara, Phys. Rev. 151 (1966) 378-386.

[7] C.C. Homes, T. Vogt, S.M. Shapiro, S. Wakimoto, A.P. Ramirez, Science 293 (2001) 673-676.

[8] G. Chiodelli, V. Massarotti, D. Capsoni, M. Bini, C.B. Azzoni, M.C. Mozzati, P. Lupotto, Solid State Commun. 132 (2004) 241-246.

[9] C.Y. Tsai, A.G. Dixon, W.R. Moser, Y.H. Ma, AIChE J. 43 (1997) 2741-2750.

[10] V. Sadykov, N. Mezentseva, G. Alikina, R. Bunina, V. Pelipenko, A. Lukashevich, S. Tikhov, V. Usoltsev, Z. Vostrikov, O. Bobrenok, A. Smirnova, J. Ross, O. Smorygo, B. Rietveld, Catal. Today 146 (2009) 132-140.

[11] S. Irusta, M.P. Pina, M. Menéndez, J. Santamaría, J. Catal. 179 (1998) 400-412.

[12] A. Musialik-Piotrowska, K. Syczewska, Catal. Today 59 (2000) 269-278.

[13] H. Ullmann, N. Trofimenko, F. Tietz, D. Stöver, A. Ahmad-Khanlou, Solid State Ionics 138 (2000) 79-90.

[14] S. Tao, J.T.S. Irvine, J. Electrochem. Soc. 151 (2004) A252-A259.

[15] H.U. Anderson, Solid State Ionics 52 (1992) 33-41.

[16] J. Kong, Y. Zhang, C. Deng, J. Xu, J. Power Sources 186 (2009) 485-489.

[17] G. Schiller, A. Ansar, M. Lang, O. Patz, J. Appl. Electrochem. 39 (2009) 293-301.

[18] J.M. Ball, M.M. Lee, A. Hey, H.J. Snaith, Energy Environ. Sci. 6 (2013) 1739-1743.

[19] M. Liu, M.B. Johnston, H.J. Snaith, Nature 501 (2013) 395-398.

[20] J.G. Mavroides, J.A. Kafalas, D.F. Kolesar, Appl. Phys. Lett. 28 (1976) 241-243.

[21] A. Kojima, K. Teshima, Y. Shirai, T. Miyasaka, J. Am. Chem. Soc. 131 (2009) 6050-6051.

[22] J. Mizusaki, H. Tagawa, Solid State Ionics 49 (1991) 111-118.

[23] Y. Teraoka, T. Nobunaga, K. Okamoto, N. Miura, and N. Yamazoe, Solid State Ionics 48 (1991) 207-212.

[24] J. Park, E.D. Wachsman, J. Electrochem. Soc. 152 (2005) A1654-A1659.

[25] A. Atkinson, A. Selcuk, Solid State Ionics 134 (2000) 59-66.

[26] M. Godickemeier, L.J. Gauckler, J. Electrochem. Soc. 145 (1998) 414-421.

[27] P. Kim-Lohsoontorn, J. Bae, J. Power Sources 196 (2011) 7161-7168.

[28] E. Iglesia, Appl. Catal. A-Gen., 161 (1997) 59-78.

[29] S. Li, S. Krishnamoorthy, A. Li, G.D. Meitzner, E. Iglesia, J. Catal. 206 (2002) 202-217.

[30] S. Krishnamoorthy, M. Tu, M.P. Ojeda, D. Pinna, J. Catal. 211 (2002) 422-433.

[31] N.Q. Minh, M.B. Mogensen, Electrochemical Society Interface 22 (2013) 55-62.

[32] J. Kniep, Q. Yin, I. Kumakiri, Y.S. Lin, Solid State Ionics 180 (2010) 1633-1639.

[33] A. Suresh, J. Basu, C.B. Carter, N. Sammes, B.A. Wilhite, J. Mater. Sci. 45 (2010) 3215-3227.

[34] J. Basu, A. Suresh, C.B. Carter, B.A. Wilhite, J. Eur. Ceram. Soc. 31 (2011) 1421-1429.

[35] Y. Teraoka, T. Nobunaga, N. Yamazoe. Chem. Lett. 17 (1988) 503-506.

[36] T. Ishihara, S. Ishikawa, C. Yu, T. Akbay, K. Hosoi, H. Nishiguchi, Y. Takita, Phys. Chem. Chem. Phys. 5 (2003) 2257-2263.

[37] H.J.M. Bouwmeester, Catal. Today 82 (2003) 141-150.

[38] Z. Shao, S. Haile, Nature 431 (2004) 170-173.

[39] J.W. Stevenson, T.R. Armstrong, R.D. Carneim, L.R. Pederson, W.J. Weber, J. Electrochem. Soc. 143 (1996) 2722-2729.

[40] T. Ishihara, H. Matsuda, Y. Takita, Solid State Ionics 79 (1995) 147-151.

[41] Y. Teraoka, H.M. Zhang, S. Furukawa, N. Yamazoe, Chem. Lett., (1985) 1743-1746.

[42] Y. Teraoka, T. Nobunaga, K. Okamoto, N. Miura, N. Yamazoe, Solid State Ionics 48 (1991) 207-212.

[43] H.J.M. Bouwmeester, A.J. Burggraaf, in A.J. Burggraaf, L. Cot (Eds.), Fundamentals of Inorganic Membrane Science and Technology, Elsevier Science B.V., Amsterdam, 1996, pp. 435.

[44] R. Moos, Int. J. Appl. Ceram. Technol. 2 (2005) 401-413.

[45] V. Esposito, E. Traversa, J. Am. Ceram. Soc. 91 (2008) 1037-1051.

[46] H. Tanaka, M. Taniguchi, M. Uenishi, N. Kajita, I. Tan, Y. Nishihata, J. Mizuki, K. Narita, M. Kimura, K. Kaneko, Angew. Chem. 118 (2006) 6144-6148.

[47] J.C. Ruiz-Morales, J. Canales-Vázquez, B. Ballesteros-Pérez, J. Peña-Martínez, D. Marrero-López, J.T.S. Irvine, P. Núñez, J. Eur. Ceram. Soc. 27 (2007) 4223-4227.

[48] H.L. Tuller, Sens. Actuators B-Chem. 187 (2013) 106-110.

[49] J. Sunarso, S. Baumann, J.M. Serra, W.A. Meulenberg, S. Liu, Y.S. Lin, J.C. Diniz da Costa, J. Membr. Sci. 320 (2008) 13-41.

[50] A. Leo, S. Liu, J.C. Diniz da Costa, Int. J. Greenh. Gas Con. 3 (2009) 357-367.

[51] W. Yang, H. Wang, X. Zhu, L. Lin, Top. Catal. 35 (2005) 155-167.

[52] A. Löfberg, H. Bodet, C. Pirovano, C. Steil, R.N. Vannier, E. Bordes-Richard, Catal. Today 117 (2006) 168-173.

[53] E.D. Bates , R.D. Mayton, I. Ntai, J.H. Davis, J. Am. Chem. Soc. 124 (2002) 926-927.

[54] A.B. Rao, E.S. Rubin, Environ. Sci. Technol. 36 (2002) 4467-4475.

[55] R. Banerjee, A. Phan, B. Wang, C. Knobler, H. Furukawa, M. O'Keeffe, O.M. Yaghi, Science 319 (2008) 939-943.

[56] X. Xu, C. Song, J.M. Andresen, B.G. Miller, A.W. Scaroni, Energ. Fuels 16 (2002) 1463-1469.

[57] H. Lunda, E. Münsterb, Appl. Energ. 76 (2003) 65-74.

[58] B.Z. Ginzburg, Renew. Energ. 3 (1993) 249-252.

[59] W. Doenitz, R. Schmidberger, E. Steinheil, R. Streicher, Int. J. Hydrogen Energ. 5 (1980) 55-63.

[60] A. Brisse, J. Schefold, M. Zahid, Int. J. Hydrogen Energ. 33 (2008) 5375-5382.

[61] G. Tao, K.R. Sridhar, C.L. Chan, Solid State Ionics 175 (2004) 615-619.

[62] J. Hartvigsen, S. Elangovan, L. Frost, A. Nickens, C.M. Stoots, J.E. O'Brien and J.S. Herring, ECS Trans. 12 (2008) 625-637.

[63] A.O. Isenberg, Solid State Ionics 3-4 (1981) 431-437.

[64] A.O. Isenberg, NASA Research Center NASA Report CR-185612 (1989).

[65] L. Elikan, J.P. Morris, C.K. Wu, NASA Research Center NASA Report CR-2014 (1972).

[66] S.D. Ebbesen, M. Mogensen, Advances in Solid Oxide Fuel Cells IV 2009.

[67] S.H. Jensen, P.H. Larsen, M. Mogensen, Int. J. Hydrogen Energ. 32 (2007) 3253-3257.

[68] Z. Zhan, W. Kobsiriphat, J.R. Wilson, M. Pillai, I. Kim, S.A. Barnett, Energ. Fuels 23 (2009) 3089-3096.

[69] P. Kim-Lohsoontorn, J. Bae, J. Power Sources 196 (2011) 7161-7168.

[70] M. Mogensen, S.H. Jensen, A. Hauch, I. Chorkendorff, T. Jacobsen, Ceram. Eng. Sci. Proc. 28 (2008) 91-101.

[71] N.Q. Minh, M.B. Mogensen, Electrochem. Soc. Interface 22 (2013) 55-62.

[72] M.A. Laguna-Bercero, J.A. Kilner, S.J. Skinner, Solid State Ionics 192 (2011) 501-504.

[73] D.M. Bierschenk, J.R. Wilson, S.A. Barnett, Energy Environ. Sci. 4 (2011) 944-951.

[74] G. Schiller, A. Ansar, M. Lang, O. Patz, J. Appl. Electrochem. 39 (2009) 293-301.

[75] M. Ni, M.K.H. Leung, D.Y.C. Leung, Int. J. Hydrogen Energ. 33 (2008) 2337-2354.

[76] A. Brisse, J. Schefold, M. Zahid, Int. J. Hydrogen Energ. 33 (2008) 5375-5382.

[77] J.D. Holladay, J. Hu, D.L. King, Y. Wang, Catal. Today 139 (2009) 244-260.

[78] S.H. Jensen, X. Sun, S.D. Ebbesen, R. Knibbe, M. Mogensen, Int. J. Hydrogen Energ. 35 (2010) 9544-9549.

[79] L. Adijanto, V.B. Padmanabhan, R. Küngas, R.J. Gorte, J.M. Vohs, J. Mater. Chem. 22 (2012) 11396-11402.

[80] X. Li, H. Zhao, F. Gao, Z. Zhu, N. Chen, W. Shen, Solid State Ionics 179 (2008) 1588-1592.

[81] J.Q. Li, P. Xiao, J. Eur. Ceram. Soc. 21 (2001) 659-668.

[82] J. Mizusaki, T. Saito, H. Tagawa, J. Electrochem. Soc. 143 (1996) 3065-3073.

[83] S.J. Skinner, Fuel Cells Bull. 33 (2001) 6-12.

[84] H.J. Hwang, J.W. Moon, S. Lee, E.A. Lee, J. Power Sources 145 (2005) 243-248.

[85] H.J.M. Bouwmeester, Catal. Today 82 (2003) 141-150.

[86] C.Y. Tsai, A.G. Dixon, W.R. Moser, Y.H. Ma, AIChE J. 43 (1997) 2741-2750.

[87] D.P. Fagg, V.V. Kharton, A.V. Kovalevsky, A.P. Viskup, E.N. Naumovich, J.R. Frade, J. Eur. Ceram. Soc. 21 (2001) 1831-1835.

[88] T. Ishihara, T. Yamada, H. Arikawa, H. Nishiguchi, Y. Takita, Solid State Ionics 135 (2000) 631-636.

[89] S. Mulmi, R. Kannan, V. Thangadurai, Solid State Ionics 262 (2014) 274-278.

[90] S. Imashuku, T. Uda, Y. Nose, G. Taniguchi, Y. Ito, Y. Awakura, J. Electrochem. Soc. 156 (2009) B1-B8.

[91] H. Matsumoto, T. Shimura, T. Higuchi, H. Tanaka, K. Katahira, T. Otake, T. Kudo, K. Yashiro, A. Kaimai, T. Kawada, J. Mizusaki, J. Electrochem. Soc. 152 (2005) A488-A492.

[92] J.L. Delattre, A.M. Stacy, T. Siegrist, J. Solid State Chem. 177 (2004) 928-935.

[93] Z. Chen, R. Ran, W. Zhou, Z. Shao, S. Liu, Electrochim. Acta 52 (2007) 7343-7351.

[94] L.W. Tai, M.M. Nasrallah, H.U. Anderson, D.M. Sparlin, S.R. Sehlin, Solid State Ionics 76 (1995) 259-271.

[95] Z. Tao, L. Bi, Z. Zhu, W. Liu, J. Power Sources 194 (2009) 801-804.

[96] X. Zhu, H. Wang, W. Yang, Chem. Commun. 24 (2004) 1130-1131.

[97] X. Zhu, Y. Cong, W. Yang, J. Membr. Sci. 283 (2006) 158-163.

[98] P. Babilo, S. Haile, J. Am. Ceram. Soc. 88 (2005) 2362-2368.

[99] S. Escolastico, M. Ivanova, C. Solis, S. Roitsch, W.A. Meulenberg, J.M. Serra, Ro. Soc. Ch. Adv. 2 (2012) 4932-4943.

[100] F.M. Figueiredo, V.V. Kharton, A.P. Viskup, J.R. Frade, J. Membr. Sci. 236 (2004) 73-80.

[101] H. Song, L. Zhang, R.B. Watson, Catal. Today 129 (2007) 346-354.

[102] D.R. Sahoo, S. Vajpai, S. Patel, K.K. Pant, Chem. Eng. J. 125 (2007) 139-147.

[103] E. Ruckenstein, H.Y. Wang, Catal. Lett. 73 (2001) 99-105.

[104] N.E. Tsakoumis, M. Rønning, Ø. Borg, E.R.A. Holmen, Catal. Today 154 (2010) 162-182.

[105] J. Clarke, M.E. Dry, J.J. Montano, W.J. van Zyl., Trans. Faraday Soc. 57 (1961) 2239-2246.

[106] R. Rudham, F.S. Stone. Chemisorption: Proceedings of Chemical Society Symposium (1956) 205-217.

[107] W. Nernst, Z. Electrochem. 6 (1899) 41-43.

[108] H. Iwahara, T. Esaka, T. Mangahara, J. Appl. Electrochem. 18 (1988) 173-177.

[109] H. Kruidhof, H.J.M. Bouwmeester, R.H.E. v. Doorn, A.J. Burggraaf, Solid State Ionics 63-65 (1993) 816-822.

[110] Y. Teraoka, T. Nobunaga, N. Yamazoe, Chem. Lett. 17 (1988) 503-506.

[111] Y. Zeng, Y.S. Lin, S.L. Swartz, J. Membr. Sci. 150 (1998) 87-98.

[112] H.J.M. Bouwmeester, H. Kruidhof, A.J. Burggraaf, Solid State Ionics 72 (1994) 185-194.

[113] V.V Kharton, A.A Yaremchenko, A.V Kovalevsky, A.P Viskup, E.N Naumovich, P.F Kerko, J. Membr. Sci. 163 (1999) 307-317.

[114] T. Ishihara, T. Yamada, H. Arikawa, H. Nishiguchi, Y. Takita, Solid State Ionics 135 (2000) 631-636.

[115] S. Kim, Y.L. Yang, R. Christoffersen, A.J. Jacobson, Solid State Ionics 104 (1997) 57-65.

[116] J.E. ten Elshof, H.J.M. Bouwmeester, H. Verweij, Appl. Catal. A-Gen. 130 (1995) 195-212.

[117] S. Li, W. Jin, P. Huang, N. Xu, J. Shi, M.Z.-C. Hu, E.A. Payzant, Y.H. Ma, AIChE J. 45 (1999) 276-284.

[118] Y. Teraoka, H.M. Zhang, S. Furukawa, N. Yamazoe, Chem. Lett. (1985) 1743-1746.

[119] J. Tong, W. Yang, B. Zhu, R. Cai, J. Membr. Sci. 203 (2002) 175-189.

[120] Z. Shao, G. Xiong, J. Tong, H. Dong, W. Yang, Sep. Purif. Technol. 25 (2001) 419-429.

[121] L. Tan, X. Gu, L. Yang, W. Jin, L. Zhang, N. Xu, J. Membr. Sci. 212 (2003) 157-165.

[122] S. Lee, K.S. Lee, S.K. Woo, J.W. Kim, T. Ishihara, D.K. Kim, Solid State Ionics 158 (2003) 287-296.

[123] H. Kusaba, Y. Shibata, K. Sasaki, Y. Teraoka, Solid State Ionics 177 (2006) 2249-2253.

[124] S. McIntosh, J.F.Vente, W.G. Haije, D.H.A. Blank, H.J.M. Bouwmeester, Chem. Mater. 18 (2006) 2187-2193.

[125] T. Nagai, W. Ito, T. Sakon, Solid State Ionics 177 (2007) 3433-3444.

[126] J.F. Vente, W.G. Haije, Z.S. Rak, J. Membr. Sci. 177 (2006) 2245-2248.

[127] Y. Teraoka, H. Shimokawa, C.Y. Kang, H. Kusaba, K. Sasaki, Solid State Ionics 177 (2006) 2245-2248.

[128] X. Zhu, H. Wang, W. Yang, Chem. Commun. (2004) 1130-1131.

[129] T. Schiestel, M. Kilgus, S. Peter, K.J. Caspary, H. Wang, J. Caro, J. Membr. Sci. 258 (2005) 1-4.

[130] C. Tablet, G. Grubert, H. Wang, T. Schiestel, M. Schroeder, B. Langanke, J. Caro, Catal. Today 104 (2005) 126-130.

[131] H. Wang, S. Werth, T. Schiestel, J. Caro, Angew. Chem. Int. Edit. 44 (2005) 6906-6909.

[132] G. Marnellos, O. Sanopoulou, A. Rizou, M. Stoukides, Solid State Ionics 97 (1997) 375-383.

[133] H. Matsumoto, T. Shimura, H. Iwahara, T. Higuchi, K. Yashiro, A. Kaimai, T. Kawada, J. Mizusaki, J. Alloy. Compd. 408-412 (2006) 456-462.

[134] G. Korotcenkov, S.D. Han, J.R. Stetter, Chem. Rev. 109 (2009) 1402-1433.

[135] Y. Du, A.S. Nowick, Solid State Ionics 91 (1996) 85-91.

[136] H. Iwahara, T. Esaka, H. Uchida, N. Maeda, Solid State Ionics 3-4 (1981) 359-363.

[137] H. Iwahara, H. Uchida, K. Ono, K. Ogaki, J. Electrochem. Soc. 135 (1988) 529-533.

[138] H. Iwahara, T. Yajima, T. Hibino, H. Ushida, J. Electrochem. Soc. 140 (1993) 1687-1691.

[139] K. Katahira, Y. Kohchi, T. Shimura, H. Iwahara, Solid State Ionics 138 (2000) 91-98.

[140] H. G. Bohn, T. Schober, J. Am. Ceram. Soc. 83 (2000) 768-772.

[141] F.L. Chen, O.T. Sorensen, G.Y. Meng, D.K. Peng, J. Eur. Ceram. Soc. 18 (1998) 1389-1395.

[142] M.W. Barsoum, Fundamentals of ceramics, Chapter 7, 175-241.

[143] T. Norby, Solid State Ionics 125 (1999) 1-11.

[144] N. Taniguchi, K. Hatoh, J. Niikura, T. Gamo, H. Iwahara, Solid State Ionics 53-56 (1992) 998-1003.

[145] J. Guan, S.E. Dorris, U. Balachandran, M. Liu, Solid State Ionics 110 (1998) 303-310.

[146] Z. Zhu, W. Sun, L. Yan, W. Liu, W. Liu, Int. J. Hydrogen Energ. 36 (2011) 6337-6342.

[147] H. Matsumoto, T. Shimura, T. Higuchi, H. Tanaka, K. Katahira, T. Otake, T. Kudo, K. Yashiro, A. Kaimai, T. Kawada, J. Mizusaki, J. Electrochem. Soc. 152 (2005) A488-A492.

[148] C. Zuo, T.H. Lee, S.J. Song, L. Chen, S.E. Dorris, U. Balachandran, M. Liu, Electrochem. Solid-State Lett. 8 (2005) J35-J37.

[149] X. Tan, J. Song, X. Meng, B. Meng, J. Eur. Ceram. Soc. 32 (2012) 2351-2357.

[150] L. Li, E. Iglesia, Chem. Eng. Sci. 58 (2003) 1977-1988.

[151] X. Wei, J. Kniep, Y.S. Lin, J. Membr. Sci. 345 (2009) 201-206.

[152] S. Fang, L. Bi, X. Wu, H. Gao, C. Chen, W. Liu, J. Power Sources 183 (2008) 126-132.

[153] J. Li, H. Yoon, E.D. Wachsman, J. Membr. Sci. 381 (2011) 126-131.

[154] T. Oh, H. Yoon, J. Li, E.D. Wachsman, J. Membr. Sci. 345 (2009) 1-4.

[155] G. Li, G. Xiong, S. Sheng, W Yang, Chinese Chem. Lett. 12 (2001) 937-940.

[156] X. Qi, Y.S. Lin, Solid State Ionics 130 (2000) 149-156.

[157] C. Zuo, S.E. Dorris, U. Balachandran, M. Liu, Chem. Mater. 18 (2006) 4647-4650.

[158] M. Cai, S. Liu, K. Efimov, J. Caro, A. Feldhoff, H. Wang, J. Membr. Sci. 343 (2009) 90-96.

[159] S. Hamakawa, L. Li, A. Li, E. Iglesia, Solid State Ionics 48 (2002) 71-81.

[160] S.J. Song, J.H. Moon, T.H. Lee, S.E. Dorris, U. Balachandran, Solid State Ionics 179 (2008) 1854-1857.

[161] G.C. Mather, D. Poulidi, A. Thursfield, M.J. Pascual, J.R. Jurado, I.S. Metcalfe, Solid State Ionics 181 (2010) 230-235.

[162] J. Song, L. Li, X. Tan, K. Li, Int. J. Hydrogen Energ. 38 (2013) 7904-7912.

[163] I. Hung, Y. Chiang, J.S. Jang, J. Lin, S. Lee, J. Chang, C. Hsi, J. Eur. Ceram. Soc. 35 (2015) 163-170.

[164] H Iwahara, H Uchida, K Kondo, K Ogaki, J. Electrochem. Soc. 135 (1988) 529-533.

[165] J. Basu, A. Suresh, B.A. Wilhite, C.B. Carter, J. Eur. Ceram. Soc. 31 (2011) 1421-1429.

[166] M.J. Scholten, J. Schoonman, J.C. van Miltenburg, H.A.J. Oonk, Solid State Ionics 61 (1993) 83-91.

[167] N. Bonanos, K.S. Knight, B. Ellis, Solid State Ionics 79 (1995) 161-170.

[168] K.H. Ryu, S.M. Haile, Solid State Ionics 125 (1999) 355-367.

[169] E. Fabbri, A. D'Epifanio, E. Di Bartolomeo, S. Licoccia, E. Traversa, Solid State Ionics 179 (2008) 558-564.

[170] X.F. Zhu, H.H. Wang, W.S. Yang, Chem. Commun. 9 (2004) 1130-1131.

[171] A. Magraso, C. Kjolseth, R. Haugsrud, T. Norby, Int. J. Hydrogen. Energ. 37 (2012) 7962-7969.

[172] Y.J. Gu, Z.G. Liu, J.H. Ouyang, Y. Zhou, F.Y. Yan, Electrochim. Acta 75 (2012) 332-338.

[173] Y. Rao, S. Zhong, F. He, Z. Wang, R. Peng, Y. Lu, Int. J. Hydrogen. Energ. 37 (2012) 12522-12527.

[174] K.D. Kreuer, Annu. Rev. Mater. Res. 33 (2003) 333-359.

[175] N. Taniguchi, T. Kuroha, C. Nishimura, K. Ijimia, Solid State Ionics 175 (2005) 2979-2983.

[176] R.C.T. Slade, S.D. Flint, N. Singh, Solid State Ionics 82 (1995) 135-141.

[177] F. Kröger, H. Vink, Academic Press 3 (1956) 307-435.

[178] C.B. Gopal, S.M. Haile, J. Mater. Chem. A 2 (2014) 2405-2417.

[179] L.G. Overholser, C.J. Barton, Sr., J.W. Ramsey, United States Patent # 2,938,769 (1960).

[180] P.G. Sundell, M.E. Bjorketun, G. Wahnstrom, Phys. Rev. B 73 (2006) 104-112.

[181] S.M. Haile, G. Staneff, K.H. Ryu, J. Mater. Sci. 36 (2001) 1149-1160.

[182] H. Zhang, A. Suresh, C.B. Carter, B.A. Wilhite, ECS Trans. 61 (2014) 307-318.

[183] L.M. Van der Haar, M.W. Den Otter, M. Morskate, H.J.M. Bouwmeester, H. Verweij, J. Electrochem. Soc. 149 (2002) J41-J46.

[184] H. Cui, A. Karthikeyan, S. Gopalan, U.B. Pal, J. Electrochem. Soc. 144 (2005) A1726-1732.

[185] I. Yasuda, T. Hikita, J. Electrochem. Soc. 141 (1994) 1268-1273.

[186] H. Yoo, C. Song, Solid State Ionics 135 (2000) 619-623.

[187] J. Yoo, A. Verma, S. Wang, A. J. Jacobson, J. Electrochem. Soc. 152 (2005) A497-A505.

[188] J.A. Lane, S.J. Benson, D. Waller, J.A. Kilner, Solid State Ionics 121 (1999) 201-208.

[189] C.J. Yu, D.M. Sparlin, H.U. Anderson, J. Am. Cerac. Soc. 70 (1987) C189-C192.

[190] H.J.M. Bouwmeester, M.W. Den Otter, B.A. Boukamp, J. Solid State Electrochem. 8 (2004) 599-605.

[191] Y. Lu, C. Kreller, S.B. Adler, J. Electrochem. Soc. 156 (2009) B513-B525.

[192] H. Wang, C. Tablet, A. Feldhoff, J. Caro, Adv. Mater. 17 (2005) 1785-1788.

[193] M. Ikeguchi, T. Mimura, Y. Sekine, E. Kikuchi, M. Matsukata, Appl. Catal. A-Gen 290 (2005) 212-220.

[194] J. Ortiz-Landeros, T. Norton, Y.S. Lin, Chem. Eng. Sci. 104 (2013) 891-898.

[195] Z. Rui, M. Anderson, Y.S. Lin, Y. Li, J. Membr. Sci. 345 (2009) 110-118.

[196] K.D. Kreuer, Chem. Mater. 8 (1996) 610-641.

[197] S.-J. Song, E.D. Wachsman, J. Rhodes, S.E. Dorris, U. Balachandran, Solid State Ionics 167 (2004) 99-105.

[198] X. Qi, Y.S. Lin, Solid State Ionics 120 (1999) 85-93.

[199] R.C. Hurlbert, J.O. Konecny, J. Chem. Phys. 34 (1961) 655-658.

[200] S. Cheng, V.K. Gupta, J.Y.S. Lin, Solid State Ionics 176 (2005) 2653-2662.

[201] H. Iwahara, T. Esaka, H. Uhida, T. Yamauchi, K. Ogaki, Solid State Ionics 18 & 19 (1986) 1003-1007.

[202] S. Zhan, X. Zhu, B. Ji, W. Wang, X. Zhang, J. Wang, W. Yang, L. Lin, J. Membr. Sci. 340 (2009) 241-248.

[203] S. Hamakawa, T. Hibino, H. Iwahara, J. Electrochem. Soc. 141 (1994) 1720-1725.

APPENDIX A

At 650-800°C, a negative-slope relationship between conductivity and pCO_2 on a log-log plot is proposed. The equilibrium between gaseous CO_2 and oxygen vacancy defects in the solid phase can be expressed by:

$$CO_{2(g)} + O_O^X + 2h^\bullet \leftrightarrow CO_{(g)} + O_{2(g)} + V_O^{\bullet\bullet} \quad \text{(I)}$$

$$K_{red} = \frac{[V_O^{\bullet\bullet}]pCOpO_2}{pCO_2[O_O^X][h^\bullet]^2} \cong \frac{[V_O^{\bullet\bullet}]pCOpO_2}{p^2}\, pCO_2^{-1} \quad \text{(A.1)}$$

where K_{red} denotes the equilibrium constant of Reaction (I), p denotes the concentration of mobile holes.

$$p = \sqrt{\frac{[V_O^{\bullet\bullet}]pCOpO_2}{K_{red}}}\, pCO_2^{-1/2} \quad \text{(A.2)}$$

The electrical conductivity can be determined by the product of the fractional concentration of mobile holes, the charge of a hole, and the mobility of the holes, μ_p.

$$\sigma_p = p \cdot e \cdot \mu_p = e \cdot \mu_p \cdot \sqrt{\frac{[V_O^{\bullet\bullet}]((pCO_2)_0 - pCO_2)^2}{K_{red}}}\, pCO_2^{-1/2} \quad \text{(A.3)}$$

given that $0 < pCO_2 < (pCO_2)_0$,

$$\frac{d(\sigma_p)}{d(pCO_2)} = e \cdot \mu_p \cdot \sqrt{\frac{[V_O^{\bullet\bullet}]}{K_{red}}} \cdot (-pCO_2^{-1/2} - \frac{1}{2} \cdot ((pCO_2)_0 - pCO_2) \cdot pCO_2^{-3/2})$$

$$= -\frac{1}{2} \cdot e \cdot \mu_p \cdot \sqrt{\frac{[V_O^{\bullet\bullet}]}{K_{red}}} \cdot \frac{1}{pCO_2^{1/2}} \cdot (1 + \frac{(pCO_2)_0}{pCO_2}) < 0 \quad \text{(A.4)}$$

The combination of Equation A.1-A.4 gives the p-type conductivity dependence on pCO_2, suggesting a negative slope. Similarly, at 600C a positive-slope dependence is proposed.